

Dissertation

Photoelectronic properties of semiconducting and insulating nanocrystals

Photoelektronische Eigenschaften halbleitender und isolierender Nanokristalle

ausgeführt zum Zwecke der Erlangung des akademischen Grades eines Doktors der technischen Wissenschaften unter der Leitung von

Prof. Dr. Erich Knözinger
und
Dr. Oliver Diwald
Inst. Nr. 165
Institut für Materialchemie

eingereicht an der Technischen Universität Wien
Fakultät für Technische Chemie

von

Dipl.-Ing. Thomas Berger
9625418
Neugasse 1, A-7021 Baumgarten

Baumgarten, im Mai 2005



Kurzfassung

Physikalische und chemische Prozesse auf Metalloxidoberflächen sind für viele technologische Anwendungen von großem Interesse. In der Regel werden dabei polykristalline Materialien eingesetzt, deren Aktivitäten durch eine Vielzahl von verschiedenen Oberflächenabschlüssen mit unbekannter Defektgeometrie und Defektkonzentration bestimmt sind. Die vorliegende Arbeit zielt auf die eingehende Untersuchung des Zusammenhangs zwischen Struktur und Reaktivität der Oberflächen von isolierenden (MgO) und halbleitenden (TiO₂) Modellsubstanzen ab. Dazu wurden Nanokristalle von möglichst definierter Größe und Gestalt über Chemische Gasphasen-Deposition hergestellt. Photoinduzierte Prozesse an der Oberfläche dieser Modellsysteme wurden dann mit Hilfe der EPR^{*}-, IR^{**}- und UV/Vis-Spektroskopie untersucht.

MgO-Nanowürfel weisen charakteristische Absorptionen im UV Bereich auf, die auf die elektronische Anregung von Ionen in Ecken und Kanten zurückgeführt werden. Damit ergibt sich ein direkter experimenteller Zugang zu den chemischen Eigenschaften dieser Zentren. Durch die Mobilität von UV-induzierten angeregten Zuständen (Oberflächenexzitonen) und deren Zerfall an Eckenanionen können letztere gezielt funktionalisiert werden. Dies wurde am Beispiel der homolytischen Wasserstoff-Spaltung an 3-fach koordinierten O⁻ Radikalen mitverfolgt: Durch wellenlängen-selektive optische Anregung können Oberflächen-Anionen zentren-spezifisch ionisiert werden. Im Zuge der Reaktion mit H₂ werden diese O⁻ Radikale in Hydroxylgruppen umgewandelt und atomarer Wasserstoff wird freigesetzt. Dieser kann an Oberflächenzentren geeigneter Elektronen-Affinität oxidiert werden. Die dabei gebildeten Farbzentren weisen charakteristische Absorptionen im Bereich des sichtbaren Lichtes auf. Der Koordinationsgrad und die lokale Geometrie der in der entsprechenden Vor- und Endstufe beobachteten paramagnetischen Zentren wurden mittels EPR-Spektroskopie charakterisiert. Theoretische Berechnungen ermöglichten die Zuordnung der gemessenen Signale zu definierten Oberflächenstrukturen.

Durch Einsatz der IR-Spektroskopie zur Detektion von Hydrid- und Hydroxylgruppen wurden Einblicke in die komplexe Chemie und Photochemie von H₂ an MgO Oberflächen gewonnen: Die elektronische Wechselwirkung von Hydroxylgruppen mit benachbarten Farbzentren führt zu einer bathochromen Verschiebung der jeweiligen OH-Streckschwingungsfrequenzen um 70 – 170 cm⁻¹. Darüber hinaus wird im EPR Spektrum eine Dublett-Aufspaltung des charakteristischen F_s⁺(H) oder (H⁺)(e⁻) Signals beobachtet, die auf die magnetische

* Elektronen-Paramagnetische-Resonanz-Spektroskopie

** Infrarot-Spektroskopie

Wechselwirkung des Spinzentrum mit dem Proton einer benachbarten Hydroxylgruppe zurückgeführt werden kann. In einer kombinierten IR- und EPR-spektroskopischen Untersuchung konnte gezeigt werden, dass $(\text{H}^+)(\text{e}^-)$ Zentren durch Oxidation von H-Atomen gebildet werden und der zugrundeliegende Oberflächendefekt nicht in den Prozess der heterolytischen Spaltung von molekularem Wasserstoff involviert ist.

Zur Untersuchung von UV-induzierten Ladungstrennungs-Prozessen hat sich die EPR-Spektroskopie als besonders geeignete Untersuchungsmethode erwiesen, da sowohl lokalisierte Elektronen als auch Elektronenlöcher als paramagnetische Zentren nachgewiesen werden können. Hinsichtlich dieser Ladungstrennungs-Prozesse werden MgO-Nanowürfel, als Isolatormaterial, mit TiO_2 Nanopartikeln, stellvertretend für halbleitende Materialien, verglichen. Die Rolle der Oberfläche im Einfang von Ladungen und in der Aufrechterhaltung der Ladungstrennung wurde untersucht.

Für den Einsatz von Halbleitern in der Photokatalyse ist die lichtinduzierte Generierung chemisch aktiver Ladungsträger eine grundlegende Voraussetzung. Nach deren Generierung können die Ladungsträger entweder rekombinieren, oder aber an dazu befähigten Zentren (im Fall von TiO_2 als Ti^{3+} -Zentren bzw. als O^- -Spezies) lokalisiert werden. Diese können schließlich mit Elektronen-Akzeptoren bzw. Elektronen-Donatoren, welche an der Oberfläche des Katalysators adsorbiert sind, reagieren. Um hohe Quantenausbeuten erreichen zu können, ist eine effektive Ladungstrennung erforderlich. Aus diesem Grund ist der Mechanismus des Ladungseinfangs für das Verständnis photokatalytischer Prozesse von großem Interesse.

Unter Hochvakuum-Bedingungen, d.h. in Abwesenheit von Elektronen-Donatoren bzw. Elektronen-Akzeptoren, rekombiniert der Großteil der durch Absorption von UV-Licht generierten Ladungsträger bei Raumtemperatur binnen weniger Nanosekunden. Bei Temperaturen $T \leq 140$ K und Lichtleistungen in der Größenordnung von $1 \text{ mW}\cdot\text{cm}^{-2}$ können Ladungseinfang-Prozesse jedoch auf einer Zeitskala von Minuten mitverfolgt werden. Der zeitliche Aufbau von lokalisierten Elektronen- und Lochzentren (Ti^{3+} bzw. O^-) wurde während bzw. nach UV-Bestrahlung mittels ESR-Spektroskopie mitverfolgt. Zusätzlich stellt sich heraus, dass der Großteil der photogenerierten Elektronen im Leitungsband verbleibt und zu einer kontinuierlichen IR-Absorption führt. In Anwesenheit von molekularem Sauerstoff – einem bekannten Elektronen-Fänger – kann die Effizienz der photoinduzierten Ladungstrennung um eine Größenordnung gesteigert werden, wobei es zur Photoadsorption von O_2 kommt. Auf dieser Grundlage wurde erstmals eine Bestimmung der absoluten Zahl der pro Nanopartikel lokalisierten Ladungen durchgeführt.

Die in der vorliegenden Arbeit präsentierten Ergebnisse liefern neue Einblicke in photophysikalische und photochemische Oberflächenphänomene an wohldefinierten Modellsystemen und stellen einen Beitrag zur Erlangung eines molekularen Verständnisses der Defektchemie an realen Katalysatoren dar.

Die vorliegende Arbeit entstand in der Zeit von Juni 2002 bis Mai 2005 unter der Leitung von Prof. Dr. Erich Knözinger und Dr. Oliver Diwald am Institut für Materialchemie der TU Wien.

Herrn Prof. Erich Knözinger danke ich herzlich dafür, mein Interesse an der Chemie und der Physik von Metalloxid-Oberflächen geweckt zu haben, sowie für die Betreuung während dieser lehrreichen Zeit.

Oliver Diwald danke ich nicht bloß für die unzähligen wissenschaftlichen Diskussionen und Erläuterungen, sondern auch für die vielen Gespräche abseits des Arbeitsalltags.

Martin Sterrer danke ich für seine Hilfe bei experimentellen Fragen.

Ganz besonderen Dank möchte ich Prof. John T. Yates von der University of Pittsburgh (USA) aussprechen, der mir den Aufenthalt am Surface Science Center ermöglicht hat. Dimitar Panayotov und Tracy L. Thompson danke ich für die Hilfestellung bei den Infrarot-spektroskopischen Untersuchungen.

Für die Unterstützung in Form von theoretischen Berechnungen danke ich Peter V. Sushko und Alexander L. Shluger vom University College London (UK).

Scott D. Walck und Johannes Bernardi danke ich für die Erstellung der Transmissionselektronen-Mikroskop-Aufnahmen.

Rainald Rosner und Johannes Frank danke ich für die Unterstützung bei technischen Problemen.

Allen Freunden und Kollegen am Institut danke ich ganz herzlich für die gute Zusammenarbeit und das angenehme Arbeitsklima.

Dem Fond zur Förderung der Wissenschaftlichen Forschung (Projekt-Nr. P 14731-CHE und P17514N11), der Österreichischen Forschungsgemeinschaft und dem Absolventenverband der TU Wien danke ich für die finanzielle Unterstützung dieser Arbeit.

1. Introduction	1
1.1. General introduction	1
1.2. Highly dispersed model systems for the study of the structure-reactivity relation of metal oxides	7
1.2.1. TiO ₂ - a prototype for semiconducting metal oxides	7
1.2.2. MgO - a prototype for insulating metal oxides	9
1.3. Photoinduced processes on metal oxides	12
1.3.1. Photoinduced reactivity of TiO ₂	13
1.3.2. Photoinduced surface phenomena on MgO	15
1.4. Scope and structure of the work	17
2. Spectroscopic techniques	18
2.1. Electron paramagnetic resonance (EPR) spectroscopy	18
2.1.1. Principles	18
2.1.2. Hyperfine interaction	21
2.1.3. Powder spectra	22
2.2. Fourier transform infrared (FTIR) spectroscopy	23
2.2.1. Hydroxyl groups as intrinsic surface probes	23
2.2.2. Free carrier absorption	25
2.3. UV/Vis diffuse reflectance spectroscopy	26
3. Experimental details	27
3.1. Sample preparation	27
3.1.1. Synthesis of TiO ₂ nanocrystals by metal organic chemical vapour deposition	27
3.1.2. Synthesis of MgO nanocubes by chemical vapour deposition (CVD)	28
3.2. Electron paramagnetic resonance (EPR) spectroscopy	30
3.3. Fourier transform infrared (FTIR) spectroscopy	31
3.3.1. Measurements at room temperature	31
3.3.2. In situ cell for measurements in the presence of UV light at low temperatures	32
3.4. UV/Vis diffuse reflectance spectroscopy	33
3.5. Reagents	34

PHOTOCHEMISTRY AND PHOTOPHYSICS ON TiO ₂ NANOCRYSTALS	35
4. Light-induced charge separation in TiO₂ nanocrystals	36
4.1. Introduction	36
4.2. Results and Discussion	39
4.2.1. Photoexcitation of oxidized TiO ₂ nanoparticles	39
4.2.2. The effect of oxygen on charge separation	43
4.2.3. Photoexcitation of reduced TiO ₂ nanoparticles	46
4.2.4. Electrical conduction effects in photochemistry experiments – an hypothesis based on a comparison of ESR and IR studies	49
4.3. Conclusions	49
5. Reversible hole trapping in anatase TiO₂ nanocrystals	51
5.1. Introduction	51
5.2. Results and Discussion	52
5.3. Conclusions	57
6. Charge trapping and the photoadsorption of O₂ on TiO₂ nanocrystals	58
6.1. Introduction	58
6.2. Results	60
6.2.1. Photoinduced charge separation at different temperatures	60
6.2.2. Charge transfer to molecular oxygen	62
6.2.3. Charge separation in the presence of an electron scavenger (O ₂)	64
6.2.4. Volumetric measurement of photoadsorbed oxygen	66
6.3. Discussion	69
6.3.1. Temperature-induced recombination	69
6.3.2. The effect of O ₂ on the efficiency of charge separation	70
6.4. Conclusions	72

SURFACE CHEMISTRY ON MgO NANOCUBES	74
7. Optical properties of surface trapped electrons	75
7.1. Introduction	75
7.2. Experimental procedure	76
7.3. Results	78
7.3.1. Colour centre formation by UV-induced oxidation of irreversibly formed hydrides	78
7.3.2. Colour centre formation by simultaneous exposure of MgO to H ₂ and UV light	79
7.3.3. Colour centre formation by homolytic H ₂ splitting at O ⁻ sites	80
7.4. Discussion	81
7.5. Conclusions	86
8. Magnetic properties of surface trapped electrons	88
8.1. Introduction	88
8.2. Results	92
8.2.1. Colour centre formation by UV-induced oxidation of irreversibly formed hydrides	92
8.2.2. Colour centre formation by simultaneous exposure of MgO to H ₂ and UV light	94
8.2.3. Colour centre formation by homolytic H ₂ splitting at O ⁻ sites	95
8.2.4. Comparison of the zeroth and the first generation colour centres	95
8.2.5. Electronic interaction between colour centre electrons and protons evidenced by IR spectroscopy	97
8.3. Discussion	98
8.4. Conclusions	103
9. Chemistry at corners and edges: generation and adsorption of H- atoms on the surface of MgO nanocubes	104
9.1. Introduction	104
9.2. Theoretical method	106
9.3. Results	107
9.3.1. Experimental data	107
9.3.2. Theoretical model	109
9.4. Discussion	112

CHARGE TRAPPING IN SEMICONDUCTORS AND INSULATORS – A COMPARATIVE STUDY	115
10. Trapping of photogenerated charges in oxide nanoparticles	116
10.1. Introduction	116
10.2. Results and Discussion	117
10.2.1. Optical excitation and charge separation	118
10.2.2. Dynamics of charge trapping	121
10.3. Conclusions	123
11. Concluding remarks	124
Appendix	126
References	129

1. Introduction

1.1. General introduction

The outstanding role metal oxides play both in science and in technology is based on the great diversity of their chemical and physical properties^{1,2}. The wide range of industrial applications of metal oxides is impressively exemplified by TiO₂, a semiconducting material with a global production of more than 4 million tons per year³. TiO₂ is used as a white pigment, as a coating for the passivation of surfaces against corrosion, in thin-film optical-interference coatings, as gas sensor, in electrodes of rechargeable lithium batteries⁴, in solar cells for the production of hydrogen and electric energy^{5,6}, in heterogeneous catalysis⁷ and as a photocatalyst for the decomposition of pollutants in air^{8,9} and wastewater^{9,10}. Due to its high dielectric constant, TiO₂ is investigated as a dielectric gate material in electronic nanodevices¹¹ and Co-doped TiO₂ films might be used as a ferromagnetic material in spintronics¹². Magnesium oxide (MgO) as another example is an insulator and is widely used in chemical industry e.g. as a scrubber for air pollutant gases (CO₂, NO_x, SO_x) and in refractory bricks in the steel industry. Furthermore, it plays an important role in heterogeneous catalysis as a support for highly active metal clusters¹³.

During the last decade the emergence of nanotechnology has entailed significant implications particularly in the research field of catalysis¹⁴. Due to their modified chemical and physical properties as compared to the respective bulk material nanoparticles exhibit altered catalytic behaviour^{13,15}. In the case of nanostructured oxides, surface properties are strongly modified with respect to infinite two-dimensional structures, giving rise to solids with unprecedented acid/base or sorption characteristics. As an example, the desorption temperature of CO on MgO strongly depends on the respective crystal size (Fig. 1.1). The chemical activity of a nanostructured system is enhanced by the presence of specific local geometrical arrangements due to surface vacancies and low-

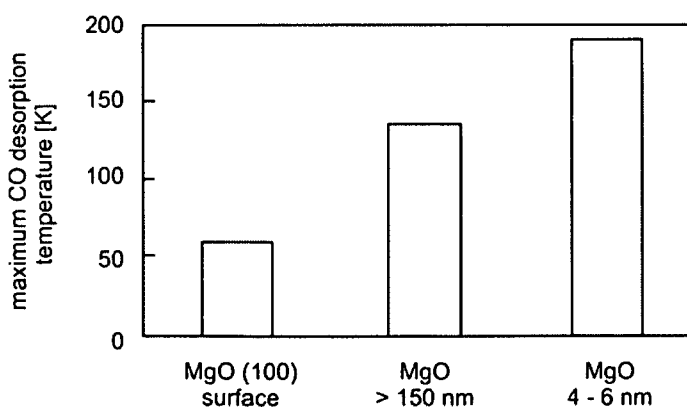


Fig. 1.1: Maximum CO desorption temperatures for nanoparticles and extended surfaces of MgO [13].

coordinated surface atoms like corners and edges. An increase in the surface area due to the decrease of the particle size thus causes an enhanced concentration of available surface active sites. The particle size may also influence the structural characteristics, namely the lattice symmetry and cell parameters. The relative phase stability of polymorphs of some metal oxides is reversed at small particle sizes due to the contribution of surface free energy. In this case, the nanostructure stabilizes a specific polymorph, which is not the stable phase for a bulk material. This actually is shown in Fig. 1.2 for TiO₂ nanocrystals obtained by metal organic chemical vapour deposition (MOCVD): At particle sizes < 14 nm anatase – although metastable from a thermodynamic point of view – is the stable polymorph¹⁶. This is due to the in general lower surface energies for anatase planes as compared to the thermodynamically stable rutile modification¹⁷. However, particle coarsening induced by thermal treatment is associated with an increased relative contribution of the bulk energy term to the total free energy and the rutile modification becomes thermodynamically more stable.

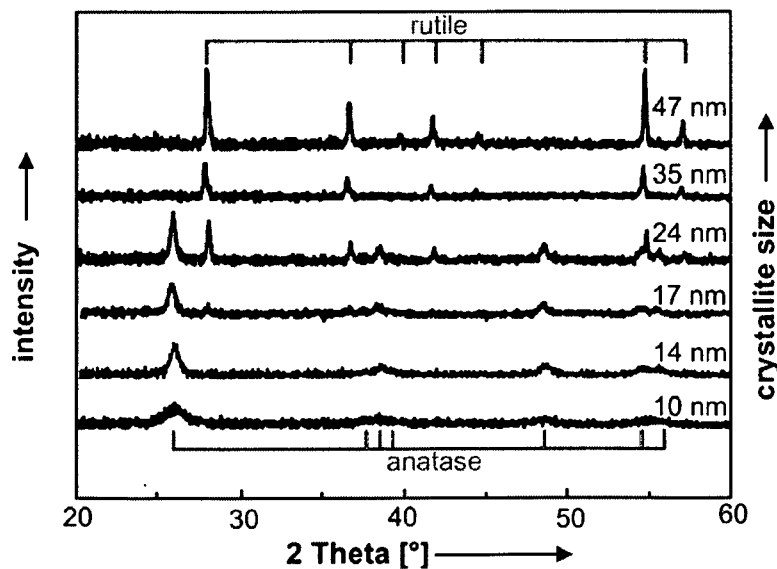


Fig. 1.2: X-ray diffractograms of TiO₂ nanocrystals produced by chemical vapour deposition (CVD). Particle coarsening was induced by annealing the sample to temperatures between 600°C and 900°C. Average particle sizes were determined from peak broadening using the Scherrer equation. The first indication for the presence of the rutile modification was found on a sample with an average particle size of 17 nm.

The change of the standard free energy for the transformation of anatase to rutile is given by

$$\Delta G^0 = \Delta_f G^0(T, \text{rutile}) - \Delta_f G^0(T, \text{anatase}) + A_R \cdot \gamma_R - A_A \cdot \gamma_A \quad (\text{Eq. 1.1})$$

where $\Delta_f G^0$ is the standard free energy of formation and A and γ represent the molar surface area and the surface free energy of titania, respectively. Assuming spherical particles Eq. 1.1 can be modified:

$$\Delta G^0 = \Delta_r G^0(T, \text{rutile}) - \Delta_r G^0(T, \text{anatase}) + 3 \cdot M \cdot r^{-1} \cdot (\gamma_R \cdot \rho_R^{-1} - \gamma_A \cdot \rho_A^{-1}) \quad (\text{Eq. 1.2})$$

where r is the radius of the particles, M the molecular weight and ρ the density. For $\Delta G^0=0$, nanocrystalline anatase is in equilibrium with rutile at a given particle size.

The majority of technological applications of metal oxides are based on surface related phenomena. Therefore, a fundamental knowledge of the interplay between the surface structure and the physical and chemical properties of the materials is of great importance. This information can, for example, be used in order to systematically design new catalysts with improved reactivity. However, metal oxides used in catalysis are rather complex systems. These so-called "real" catalysts are characterized by the presence of particles of different morphology, broad particle size distributions, a high concentration of different surface defects and possibly more than one crystal structure. Furthermore, the sample properties can change under working conditions, i.e. at ambient or elevated temperature and pressure. In conclusion, "real" catalysts under working conditions represent a worst case with regard to the modelling and understanding of the underlying processes on an atomic level because of the heterogeneity of the system.

	real surfaces (catalyst)		ideal surfaces
<i>origin:</i>	non-equilibrium processes	materials gap	equilibrium processes
<i>surface:</i>	high specific surface area		low specific surface area
	set of surface planes		well defined uniform geometry
	high defect concentration		low defect concentration
	non-uniform defect geometry		uniform defect geometry
<i>surface defect characterization:</i>	molecular spectroscopies; transmission electron microscopy, temperature programmed desorption		ultra-high vacuum techniques,... scanning probe microscopies, electron spectroscopies,... temperature programmed desorption

Tab. 1.1: The materials gap between catalysis and surface science – powder surfaces versus single crystalline surfaces.

A strategy to make catalysts accessible to structure-reactivity investigations is to systematically reduce the complexity of "real" systems by using model systems with well-defined and tuneable properties. The following strategies are applied:

- Single crystals are used in order to obtain well-defined surfaces. However, the discrepancy between the model material and “real” catalysts opens the so-called *materials gap* (Tab.1.1).
- Ultra-high vacuum conditions allow for the preparation of clean surfaces. Furthermore, adsorption experiments can be performed under defined conditions. The difference with respect to working conditions opens the so-called *pressure gap*.

A plethora of powerful surface techniques has become accessible in the last decades and allowed to investigate the surface geometry and the interaction of specific surface sites with molecules from the gas-phase^{18,19}. Many of the most powerful surface science techniques are related to the detection of impinging or emitted charged particles and need, therefore, to be performed under ultra-high vacuum (UHV) conditions. However, the *pressure gap* can be bridged to a certain degree by the combination of UHV methods with surface sensitive techniques that work in the presence of a gas-phase²⁰.

In order to bridge the *materials gap*, model systems with increasing degree of complexity ranging from single crystals to highly defective surfaces and epitaxially grown thin films have been investigated^{1,21}. Furthermore, highly dispersed metal clusters of different size can be deposited on such films²⁰.

A special aspect of the *materials gap* becomes obvious for photocatalysts. The initial step of a photocatalytic reaction is the light-induced generation of an electron/hole pair in the bulk of a semiconductor particle. In order to initiate reactions with molecules from gas-phase or solution the charge carriers have then to migrate to the particles' surface. In principle both electrons and holes can react with molecules from the ambient phase.

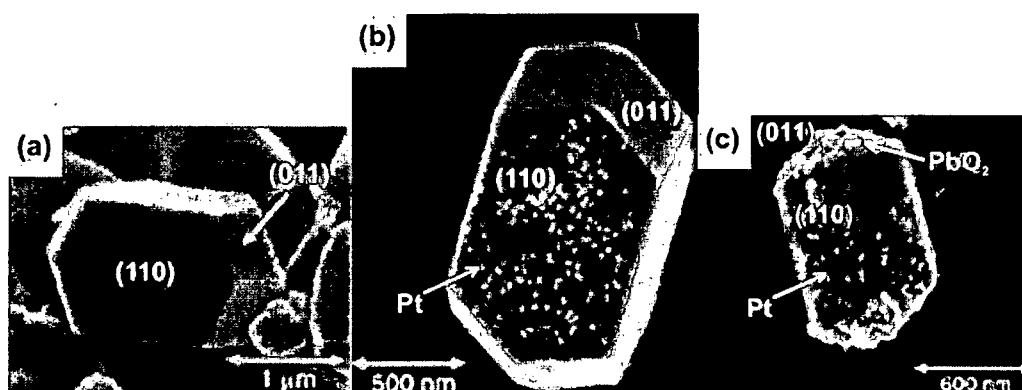


Fig. 1.3: (a) microcrystalline rutile before and (b) after reductive Pt deposition, c) after oxidative PbO_2 deposition [22].

Only recently, Ohno et al.²² have shown that on the surface of appropriately sized TiO₂ microcrystals ($d \sim 1 \mu\text{m}$) reduction and oxidation of metal ions from aqueous solution by photogenerated charge carriers occur at different crystal faces (Fig. 1.3). The investigation allowed for an assignment of reduction (Fig. 1.3b) and oxidation sites (Fig. 1.3c) to specific surface planes. However, analogous experiments carried out on single crystalline surfaces²³ and on the polished surface of randomly textured and large polycrystals ($d \sim 55 \mu\text{m}$)²⁴

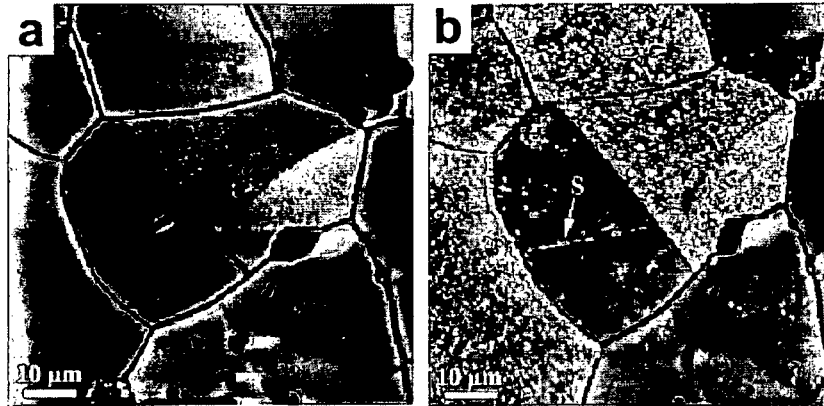


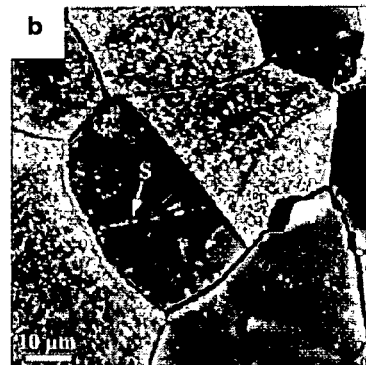
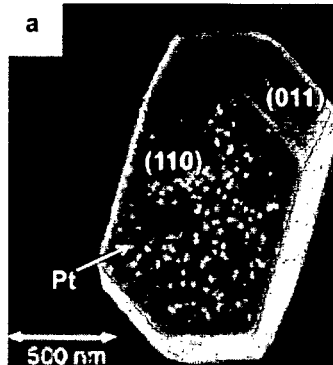
Fig. 1.4: Atomic force micrographs of differently oriented grains in a polycrystalline rutile TiO₂ ceramic (a) before and (b) after photoreductive deposition of Ag [24].

revealed opposite trends (Fig. 1.4). In fact, synergistic effects between different faces have to be taken into account for particulate systems of appropriate size. This is illustrated in Fig. 1.5:

- a) appropriately sized microcrystals (Fig. 1.5a): a photon with supra band gap energy induces the generation of an electron/hole pair in the particles' bulk. The respective charge carriers then migrate to the surface: Electrons preferentially react at the (110) plane, where they reduce metal ions (M^+). The metal (M) is deposited at the respective surface. Holes preferentially react at the (011) plane, where they oxidize an appropriate donor molecule D^- (e.g.: $4h^+ + H_2O \rightarrow O_2 + 4H^+$). The reduction of M^+ at the (110) surface is, therefore, facilitated by the consumption of holes at the (011) plane and gives rise to a synergistic effect between the two faces.
- b) extended surfaces (Fig. 1.5b): In this case the reaction is reduced to a quasi-2-dimensional problem: due to the extension of the separated single crystalline surfaces both reduction and oxidation reactions have to take place on the same crystal face. The high photocatalytic activity of the (011) plane is, therefore, explained by the ability of this surface to effectively separate electrons from holes and to enhance their availability for respective reduction and oxidation reactions. The (110) surface on the other hand does not facilitate charge separation - recombination occurs.

a) 3-dimensional model system

b) quasi-2-dimensional model system

microcrystal ($d=1\mu\text{m}$):polished surface of randomly textured polycrystals ($d=55\mu\text{m}$):

observed reactivity of surface planes for UV induced metal deposition:

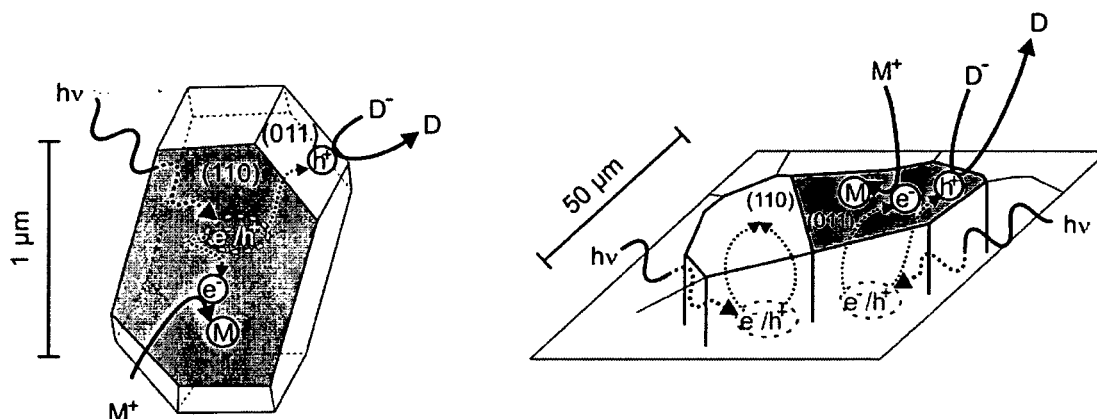
 $(110) > (011)$ $(011) > (110)$ 

Fig. 1.5: Face dependent reactivity of polycrystalline TiO_2 systems. Photoinduced metal deposition is used as the model reaction. Different reactivities are found for the same faces on (a) microcrystals and (b) the polished surface of randomly textured polycrystals [22,24].

The situation becomes even more complicated for metal oxides with more than one stable crystalline phase. In this case synergism between the polymorphs has to be considered as well²⁵.

These results impressively show that in order to understand processes in photocatalysis, a fundamental knowledge of the interconnection of surface and bulk properties is required. The use of model systems on the basis of single crystals or films in order to bridge the *materials gap* is, therefore, limited. Indeed, the investigation of well-defined polycrystalline materials is indispensable to realistically model processes on real catalysts.

For model studies, polycrystalline systems have to meet certain requirements. They should exhibit a well-defined morphology, defects of uniform geometry, a narrow particle size distribution and a defined crystalline structure. All these properties should be independently tuneable by using different synthesis methods. Bridging of the *materials gap* starting from polycrystals, therefore, strongly depends on the development of novel preparation techniques in order to provide appropriate model catalysts for structure-reactivity investigations.

1.2. Highly dispersed model systems for the study of the structure-reactivity relation of metal oxides

1.2.1. TiO_2 - a prototype for semiconducting metal oxides

TiO_2 crystallizes in three different structures: rutile, anatase and brookite. However, only rutile and anatase play a role in technological applications. Both structures exhibit a tetragonal unit cell and may be discussed in terms of differently interconnected basic units. These consist of a titanium atom surrounded by six oxygen atoms in a more or less distorted octahedral configuration (Fig. 1.6). Rutile is the most stable bulk phase at normal temperature and

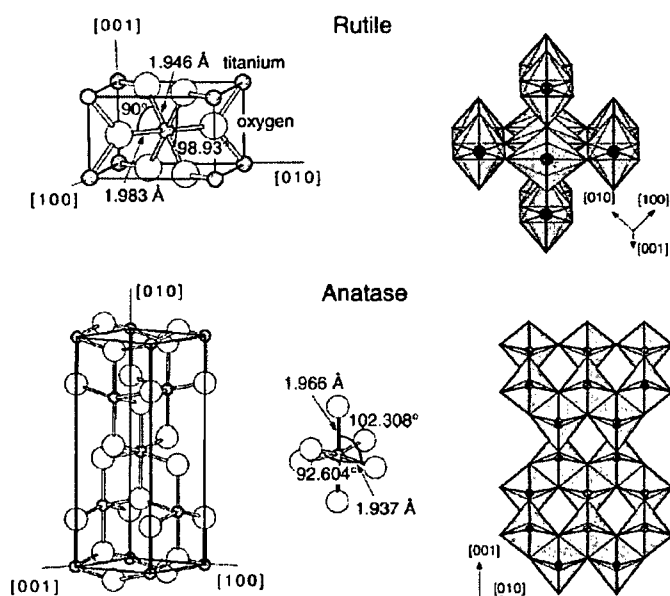


Fig. 1.6: Bulk structures of rutile and anatase. The tetragonal bulk unit cell of rutile has the dimensions $a = b = 4.587 \text{ \AA}$, $c = 2.953 \text{ \AA}$, and the one of anatase $a = b = 3.782 \text{ \AA}$, $c = 9.502 \text{ \AA}$. In both structures slightly distorted octahedra are the basic building units [19].

pressure, however, at particle sizes < 14 nm anatase is the stable polymorph (Fig. 1.2)²⁶. This is due to the in general lower surface energies for anatase planes as compared to the rutile modification²⁷.

Due to its importance in catalysis and its applicability in surface science studies TiO_2 has become a prototype for the investigation of surface processes on transition-metal oxides. It can be made conducting in the bulk by simply annealing in ultra-high vacuum. Electron and ion spectroscopies may, therefore, be used without any surface charging problems. Only recently the direct observation of oxygen vacancies became possible using atomic force microscopy (AFM)²⁸ and scanning tunneling microscopy (STM, Fig. 1.7)^{29,30}.

Oxygen vacancies are created very easily on TiO_2 surfaces by an annealing procedure: High temperature treatment at ultra-high vacuum conditions induces the removal of oxygen atoms from the lattice and the subsequent desorption of oxygen from the surface. Two electrons are left on the surface upon removal of one oxygen atom ($\text{O}^{2-} \rightarrow \text{O} + 2\text{e}^-$). These electrons occupy 3d states of the Ti sites immediately adjacent to the oxygen vacancy. Thus, the oxidation state of the Ti sites is lowered from 4+ to 3+ or 2+.

Rutile TiO_2 is the metal oxide whose surface properties have been studied most thoroughly due to the fact that stoichiometric, well-ordered and nearly perfect surfaces may be produced relatively easily¹⁹. However, also single crystalline anatase samples of high purity³¹ and epitaxially grown anatase thin films³² became available only recently.

On the other hand, novel synthesis methods provide nanosized TiO_2 powders of different size and morphology (Fig. 1.8)⁴⁴. Physical as well as chemical preparation techniques have reached significant advances concerning the homogeneity of structural and electronic properties. These methods, therefore, provide well-defined systems for the investigation of the structure-reactivity relation of photocatalysts.

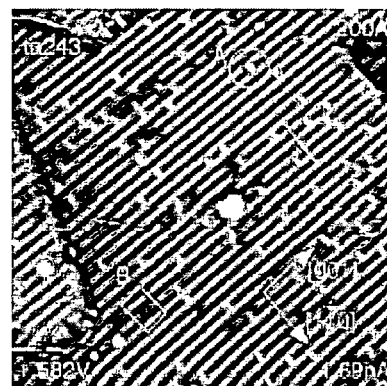


Fig. 1.7: STM image (200 Å x 200 Å) of a $\text{TiO}_2(110)$ surface, sputtered and annealed in ultra-high vacuum to 1100 K for 10 min, showing point defects. Features labeled with "A" have been assigned as oxygen vacancies [29].

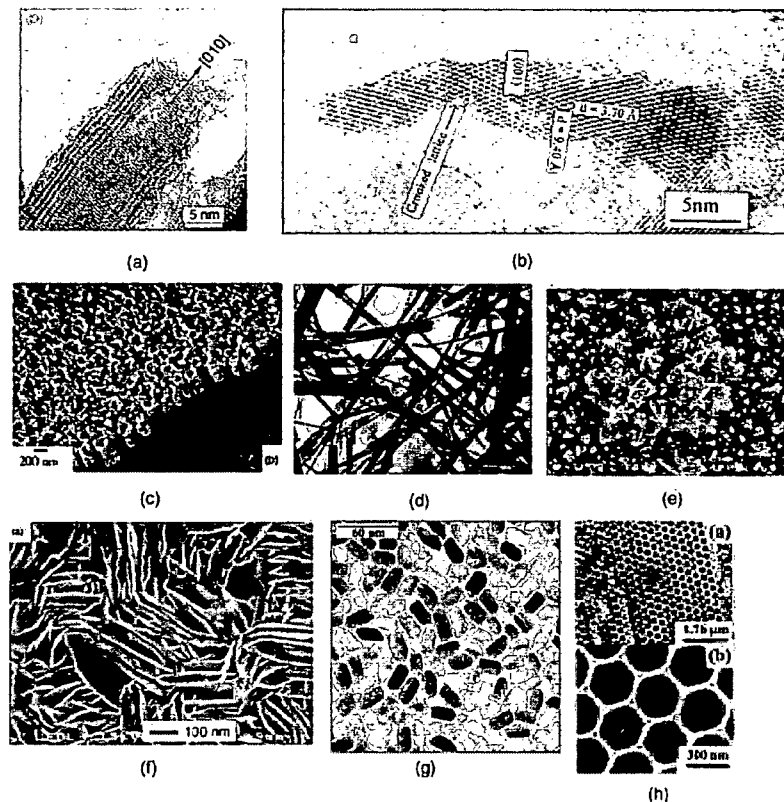


Fig. 1.8: Novel synthesis methods provide nanosized TiO_2 powders of different morphology [44].

1.2.2. MgO - a prototype for insulating metal oxides

Magnesium oxide is a highly ionic insulator with a band gap of 7.8 eV. It crystallizes in the simplest possible oxide structure exhibiting a face centred cubic unit cell. The respective (100) surface is due to its non-polar and atomically flat nature by far the most stable face and, therefore, the dominant surface plane in polycrystalline MgO. This is the reason for the outstanding role of MgO as a model system for the investigation of surface related properties of metal oxides^{1,21}.

From a chemical point of view, extended MgO single crystal surfaces are relatively inert. It was shown only recently in a combined scanning tunneling microscopy (STM) and electron paramagnetic resonance (EPR) study that paramagnetic electron centres on defective single crystalline films are predominantly formed at low coordinated sites, whereas sites at extended terraces are rather inactive³³. Thus, chemical and electronic properties are strongly modified when the defectivity of the crystal is increased. This is the reason for the complex surface chemistry of polycrystalline metal oxides, which are characterized by a plethora of specific geometrical surface arrangements. These are differently coordinated surface ions

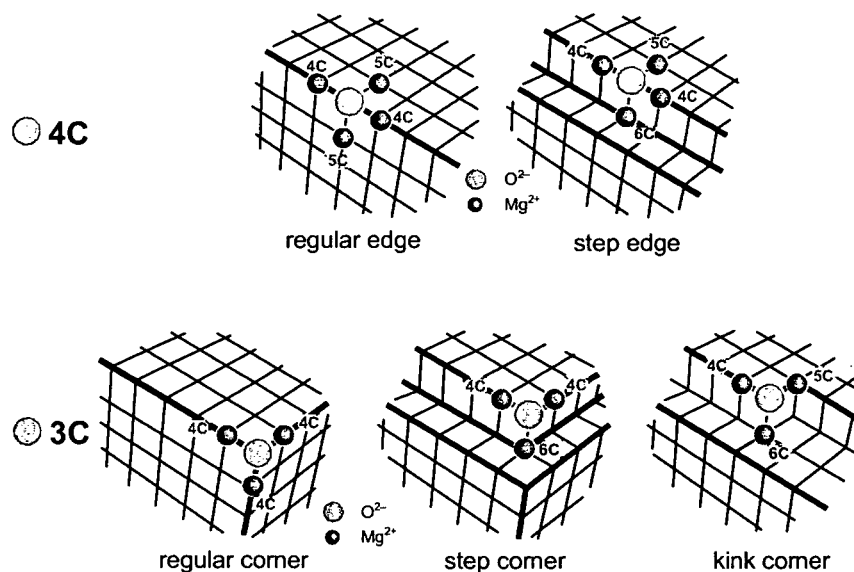


Fig. 1.9: Different geometrical features of low coordinated oxygen ions in edges (4-coordinated, 4C) and corners (3-coordinated, 3C) on MgO according to Shluger et al. [34].

and structural defects like surface ion vacancies. The investigation of the structure-reactivity relation of surface defects on metal oxides is, therefore, of great importance.

It was shown by means of quantum mechanical calculations that the electronic properties of low coordinated surface ions are strongly influenced even by their second coordination sphere³⁴. Therefore, complex surface features have to be considered to model the surface of powdered metal oxide samples. The plethora of local surface structures shall be adumbrated in Fig. 1.9 and Fig. 1.10, which show a selection of possible types of low coordinated anions and anion vacancies, respectively. These types of defects are expected to play an important role in the surface chemistry of polycrystalline MgO.

The first coordination sphere of an anion at a *regular edge site* and at a *step edge* is the same – in both cases it is 4-coordinated (4C). However, there are differences in the second coordination sphere: In the case of a *regular edge* site, the 4C oxygen ion is surrounded by two 4C and two 5C Mg ions, respectively, whereas the 4C oxygen ion at the *step edge* is surrounded by two 4C Mg ions, one 5C and one 6C Mg ion. Differences in the second coordination sphere are also observed for 3-coordinated oxygen anions at the *regular corner*, at the *step corner* and at the *kink corner* (Fig. 1.9).

Removal of the respective low coordinated oxygen anion gives rise to vacancies and sites of different local geometry (Fig. 1.10).

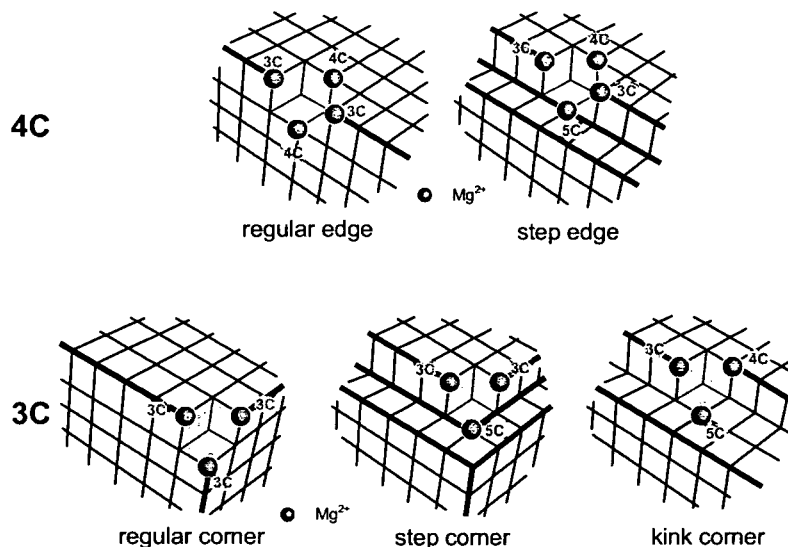


Fig. 1.10: Classical anion vacancies in 3- and 4-fold coordination and some examples of related defects with differently coordinated next nearest neighbours.

Molecular surface probes as well as surface trapped charge carriers have been used extensively to investigate the nature and location of such defects³⁶⁻⁴⁰. Surface sites with sufficient electron affinity, may be effectively probed by electrons. The doping of the respective sites with electrons may be achieved either by adsorption of atoms with low ionisation energy or by ionising radiation such as UV, X- or γ -rays. The respective trapping site thus gets accessible for spectroscopic investigations. For the characterization of paramagnetic centres EPR spectroscopy is an extremely powerful technique.

Tench and Nelson introduced the picture of oxygen vacancies on the (100) surface as electron trapping sites³⁵. They extended the model of so-called colour centres originally observed in the bulk of alkali halides to the surface. These centres were denoted as F_s^{n+} ("n+", with $n = 0, 1, 2$ stands for the charge of the vacancy; the subscript denotes the location in the surface). However, calculated formation energies for anion vacancy defects on the MgO (100) surface plane exclude a high abundance of such defects. Therefore, several alternative models have been proposed as trapping sites, ranging from low-coordinated vacancies at steps and corners³⁶ to neutral anion-cation-divacancies³⁷ or local non-stoichiometries such as the reverse corner³⁸. Only recently, it was shown in a combined experimental and quantum mechanical investigation, that an electron may be trapped even at a single 3-coordinated Mg^{2+} cation, where a nearby hydroxyl group provides a positive electrostatic potential³⁹. This centre could be tracked by EPR spectroscopy due to the hyperfine and super-hyperfine interaction with the next nearest ^{25}Mg cations and the nearby proton, respectively. The centre belongs to the class of the so-called $F_s^+(H)$ or $(H^+)(e^-)$ centres. These centres are characterized by the magnetic interaction of the trapped electron

with the proton of a nearby hydroxyl group, giving rise to a doublet-splitting of the respective signal in the EPR spectrum. In addition, the frequency of the respective hydroxyl stretching vibration is strongly influenced by the interaction with the trapped electron. Thus, IR spectroscopy provides complementary information about the centre of interest⁴⁰.

In order to spectroscopically investigate the surface of polycrystalline materials well-defined model systems are required. Non-equilibrium techniques such as chemical vapour deposition (CVD) lead to high surface area materials with a high concentration of differently coordinated surface ions and surface ion vacancies. Furthermore, the particles exhibit a well-defined morphology and a narrow particle size distribution (Fig. 1.11)⁵¹.



Fig. 1.11: Chemical vapour deposition (CVD) provides well-defined model systems for the investigation of the structure-reactivity relation.

1.3. Photoinduced processes on metal oxides

In 1972, Fujishima and Honda used TiO_2 as a catalytic electrode in a photoelectrolysis cell to decompose water into H_2 and O_2 , without the application of an external voltage⁵. Since then, various metal oxide surfaces have been investigated extensively in order to understand the fundamental processes of photoinduced reactions. In addition to the possible application in photoelectrochemical solar energy conversion⁶, environmental photocatalysis has become a highly investigated research area due to the fact, that highly oxidizing species, formed at the surface of semiconducting photocatalysts, allow for a destruction of organic compounds in polluted air and wastewaters¹⁰. A unique phenomenon, the so-called super-hydrophilicity, was reported only recently⁴¹: Water droplets on TiO_2 surfaces spread out when UV irradiation is applied. However, storage in the dark again induces a gradual increase in the water-contact angle. Although the underlying mechanisms are not yet clear, TiO_2 -coated glasses are used as self-cleaning and antifogging surfaces.

Heterogeneous photocatalysis is based on the photoinduced conversion of molecules on the surface of a solid catalyst. According to differences in the mechanism of photoexcitation,

photocatalysis is generally divided into two classes⁹: In the case of *catalysed photoreactions* the initial photoexcitation occurs in the adsorbed molecule. On the other hand, the process is referred to as a *sensitised photoreaction*, when the initial excitation takes place in the catalyst substrate followed by a charge carrier transfer and/or energy transfer into a ground state molecule. The spectral quantum yield of a *catalysed photoreaction* depends only on the wavelength dependence of the rate constant for the formation of the products. In the case of a *sensitised photoreaction* the spectral quantum yield is determined by the spectral dependence of the concentration of photogenerated charge carriers⁴².

The results presented in this study are concerned with *sensitised photoreactions*, i.e. the direct excitation of electron transitions in the TiO₂ and MgO model catalysts. Therefore, this class of reaction will be described in more detail in the following.

1.3.1. Photoinduced reactivity of TiO₂

Semiconductors can act as sensitisers for light-induced redox processes due to their electronic structure, which is characterized by the existence of a void energy region. This so-called band gap extends from the top of the filled valence band to the bottom of the vacant conduction band and assures a sufficiently long lifetime of the charge carriers to diffuse to the catalysts' surface and to initiate a redox reaction.

The ability of a semiconductor to photocatalyse a chemical reaction is governed by the band energy positions of the semiconductor and the redox potentials of the adsorbate. Due to thermodynamical reasons, the relevant potential level of the acceptor species is required to be below (more positive than) the conduction band potential of the semiconductor. The potential level of the donor needs to be above (more negative than) the valence band position of the semiconductor in order to donate an electron to the vacant hole.

The initial process in heterogeneous photocatalysis is the generation of an electron-hole pair in the semiconductor particle: when a photon with an energy $h\nu$ matches or exceeds the band gap energy of the semiconductor, an electron is promoted from the valence band to the conduction band leaving a hole behind. The fate of the separated electron and hole can follow several pathways: The desired reaction of electrons and holes at the particles' surface with electron acceptors and donor species from gas-phase or solution requires a charge carrier migration from the bulk to the surface. However, the recombination of charge carriers in the bulk and at the surface of the catalyst, which is accompanied by heat release, competes with the interfacial charge transfer. In the absence of electron and hole

scavengers, the stored energy is dissipated within a few nanoseconds⁴³. However, in the presence of a suitable scavenger or surface defect state charge carrier trapping may occur, thus preventing recombination. The overall quantum efficiency of the interfacial charge transfer, is determined by two critical processes^{10,44}:

- the competition between charge-carrier recombination and trapping (picoseconds to nanoseconds)
- the competition between trapped carrier recombination and interfacial charge transfer (microseconds to milliseconds)

Titaniumdioxide is an indirect semiconductor (Fig. 1.12)^{45,46}. The location of the lowest conduction band edge is shifted from the highest valence band edge at the centre of the respective Brillouin zone. The fundamental band-to-band transition, therefore, requires a change in both, energy and momentum and is assisted by a phonon, which provides the change in momentum. In the case of indirect semiconductors both, the fundamental absorption as well as the respective emission are much weaker than in direct semiconductors. For photocatalysts, however, an efficient absorption is needed in order to obtain high quantum yields.

Nevertheless, TiO_2 is close to being an ideal photocatalyst: it is cheap, nontoxic, chemically inert, photocatalytically stable and the photogenerated holes are highly oxidizing. Furthermore, photogenerated electrons are reducing enough to produce superoxide from O_2 . A shortcoming is that it absorbs only a small fraction of solar radiation (band gap of rutile and anatase: 3.0 eV and 3.2 eV, respectively). Great efforts have, therefore, been made to induce a bathochromic shift and a visible light activity of TiO_2 catalysts. Only recently it was reported that by substituting lattice oxygen with different ions (N, C, S) a catalytic activity in the visible could be obtained^{44,47,48}. However, the reasons for these effects are still subject of a controversial discussion⁴⁹.

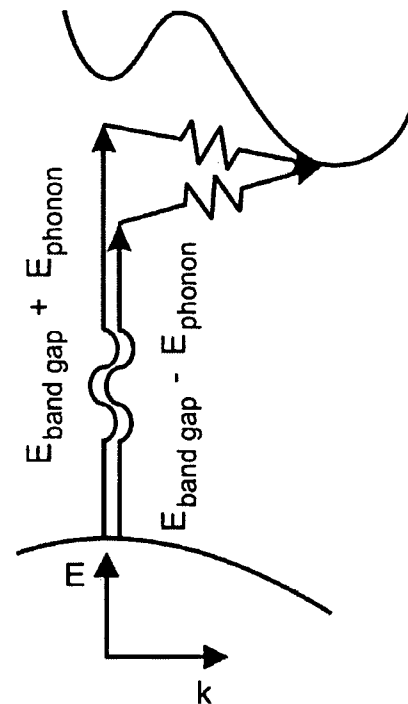


Fig. 1.12: Phonon assisted transitions in indirect semiconductors.

1.3.2. Photoinduced surface phenomena on MgO

The fundamental bulk absorption edge of MgO is 7.8 eV and, therefore, far too wide for an economical use of this insulator in photocatalysis. However, several photoinduced surface processes may take place at highly dispersed samples using photon energies much lower than the band gap.

Fig. 1.13 shows that the UV diffuse reflectance spectrum of dehydroxylated MgO nanocrystals exhibits two minima (maxima in absorption) in the energy range $4 \text{ eV} < E < 6 \text{ eV}$. The respective low energy absorptions were assigned to transitions in low coordinated oxygen anions at the surface of the crystals ($\text{O}_{\text{LC}}^{2-}$)⁵⁰. Furthermore, it was assumed that the respective surface state transitions were of excitonic nature. The observed bathochromic shift is caused by the reduction of the electrostatic potential at the surface of ionic crystals. The magnitude of the so-called Madelung potential is a measure for the electrostatic stabilization of an ion and depends on the coordination state, the charge and the distance to neighbour-ions. The experimentally observed transitions are, therefore, associated with the excitation of excitons at 4-coordinated ($\text{O}_{4\text{C}}^{2-}$, 5.4 eV) and 3-coordinated ($\text{O}_{3\text{C}}^{2-}$, 4.6 eV) oxygen anions. This assignment was corroborated only recently by quantum theoretical calculations³⁴ and further experimental investigations⁵¹.

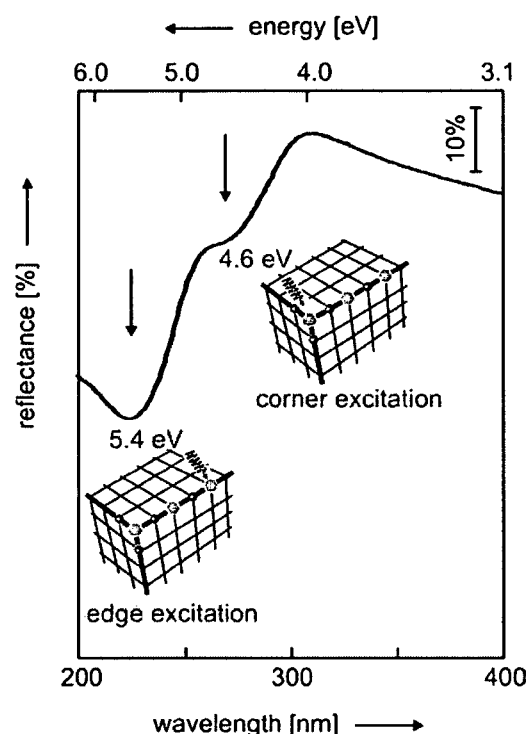


Fig. 1.13: UV diffuse reflectance spectrum of dehydroxylated MgO nanocubes.

Theoretical studies have given evidence for the delocalisation of the photogenerated states^{34,50}. Whereas excitons on 3-coordinated sites are strongly localized, excited states at higher coordinated sites tend to be mobile. The absorption and emission of light can, therefore, take place at different sites on the surface. Detailed analysis of the respective deactivation processes by luminescence spectroscopy has corroborated this assumption^{51, 52}. Electrons from the excited state, however, may return to the ground state also via radiationless deactivation by excitation of phonons.

1.4. Scope and structure of the work

The present study focuses on the spectroscopic investigation of trapped charge carriers at the surface of semiconducting and insulating nanocrystals. The investigation has two major topics: First, to gain fundamental knowledge of photoinduced charge separation phenomena and to understand the reactivity of photogenerated charges towards simple molecules like O₂ and H₂. Second, the structural properties of charge trapping sites shall be investigated using trapped charge carriers and surface hydroxyl groups as probes for geometrically different surface arrays. The interconnection between the two topics shall contribute to the elucidation of the structure-reactivity relation of well-defined model systems.

The whole study is divided into three parts: Part one faces the trapping of photogenerated charge carriers in TiO₂ nanocrystals. How the trapping process is determined by temperature, light irradiance and the concentration of reactive molecules in the gas-phase is the central question of this part. Quantitative information on the absolute number of charge carriers trapped per nanoparticle is provided.

Part two is concerned with the surface chemistry on MgO nanocubes. Based on existing knowledge of defect centres on this material, reactive O⁻ hole centres are generated site-specifically and their reaction towards H₂ is investigated. Furthermore, the optical and magnetic properties of surface trapped electrons are studied and conclusions about the structure of the respective defect centres will be drawn.

In the third part of this thesis a comparison of charge trapping processes on semiconducting and insulating nanoparticles will be given.

Different spectroscopic techniques are used in this study: Electron paramagnetic resonance (EPR) spectroscopy, Fourier transform infrared (FTIR) spectroscopy and diffuse reflectance (DR) UV/Vis spectroscopy. An introduction to the respective techniques is given in the following section.

2. Spectroscopic techniques

2.1. Electron paramagnetic resonance (EPR) spectroscopy

2.1.1. Principles

Electron paramagnetic resonance (EPR) spectroscopy^{56,57} is an experimental technique for the detection and characterization of chemical systems bearing unpaired electrons, i.e. paramagnetic systems. These include free radicals, transition metal ions and paramagnetic point defects trapped in solid matrices. EPR spectroscopy, in fact, is one of the leading techniques to study the effects of radiation in the solid state.

Most molecular spectroscopic techniques investigate the interaction of the electric field component of the respective electromagnetic radiation with some electric dipole moment in the molecules (see also section 2.2, infrared spectroscopy and section 2.3, UV/Vis spectroscopy). Different to them, EPR spectroscopy is based on the interaction of the magnetic component of the radiation with magnetic dipoles of paramagnetic centres, namely the magnetic moment of unpaired electrons. The respective magnetic moment μ_S results from the intrinsic angular momentum of an electron, the so-called electron spin \mathbf{S} (vectors are denoted by bold letters in the following). The magnetic moment is collinear and antiparallel to the spin and is given by:

$$\mu_S = -g_e \cdot \mu_B \cdot \mathbf{S} \quad (\text{Eq. 2.1})$$

with: g_e free electron g value ($g_e=2.0023$)
 μ_B Bohr magneton $=9.27 \cdot 10^{-24} \text{JT}^{-1} = e \cdot h \cdot (4\pi \cdot m_e)^{-1}$
 \mathbf{S} intrinsic angular momentum

Due to Heisenberg's uncertainty principle only the square of the intrinsic angular momentum (\mathbf{S}^2) and one component in a given direction (e.g. S_z) can be measured with certainty. The magnitude \mathbf{S}^2 is given by $[\mathbf{S} \cdot (\mathbf{S}+1)]^{1/2} \cdot \hbar$, where S is the primary spin quantum number. The allowed values of \mathbf{S} along any selected direction are restricted to the secondary spin quantum numbers M_S , which range in unit increments from $-S$ to $+S$, giving $2S+1$ possible components along an arbitrary direction.

The spin quantum numbers of an electron are $S = 1/2$ and $M_S = \pm 1/2$, respectively. In the absence of a magnetic field the spin vectors \mathbf{S} (and the corresponding magnetic moments) of an assembly of paramagnetic electrons are randomly aligned. However, when a magnetic field \mathbf{B} is applied along the z-axis, two possible orientations of the electron spin \mathbf{S}

are allowed. These are associated with values $S_z = +1/2 \cdot \hbar$ (\uparrow or α state, $M_S = +1/2$) and $S_z = -1/2 \cdot \hbar$ (\downarrow or β state, $M_S = -1/2$). The two permitted orientations of the spins are associated with different energies:

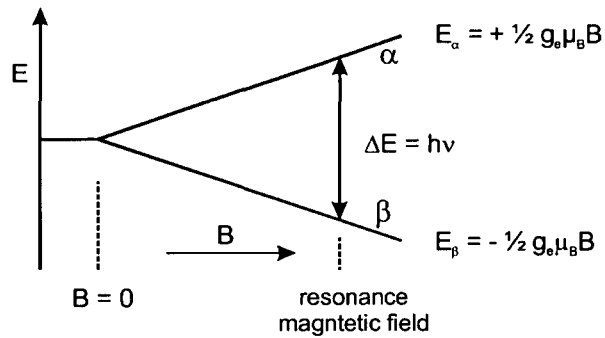


Fig. 2.1: Linear dependence between applied magnetic field and energy level splitting of the spin eigenstates of the unpaired electron.

$$E = (\pm 1/2) \cdot g_e \cdot \mu_B \cdot B \quad (\text{Eq. 2.2})$$

This energy splitting is called the electronic Zeeman effect. The higher energy level is occupied by spin states with the magnetic moment aligned opposite to the direction of the magnetic field (\uparrow or α state), whereas spin states with magnetic moments parallel to the magnetic field occupy the lower energy levels (\downarrow or β state). The energy difference between these two states is then given by:

$$\Delta E = E_\alpha - E_\beta = g_e \cdot \mu_B \cdot B \quad (\text{Eq. 2.3})$$

The two states are degenerate in zero field and their separation increases linearly with B (Fig. 2.1).

At thermal equilibrium and in the presence of an external field, the spin population is determined by the Boltzmann distribution:

$$n_\alpha/n_\beta = e^{-\Delta E/(kT)} \quad (\text{Eq. 2.4})$$

with:

- $n_{\alpha/\beta}$ spin population for $M_S = +1/2$ and $M_S = -1/2$, respectively
- ΔE energy difference between α and β state [J]
- k Boltzmann constant ($k = 1.38 \cdot 10^{-23} \text{JK}^{-1}$)
- T absolute temperature [K]

At 77K, in a field of about 3000 G, the ratio n_α/n_β accounts only for 0.995.

In an EPR experiment the transition of an electron between the two states is investigated by the resonance absorption of electromagnetic radiation of appropriate energy $h\nu$. To observe the spin transition the following resonance condition must be fulfilled:

$$h\nu = \Delta E = E_\alpha - E_\beta = g_e \cdot \mu_B \cdot B \quad (\text{Eq. 2.5})$$

In a so-called "field sweep" EPR experiment the frequency is kept constant and the magnetic field is varied. The intensity of the transition at a given resonance magnetic field depends on the population difference $n_\beta - n_\alpha$, which is proportional to the reciprocal value of the absolute temperature (Curie law).

However, in most cases the observed system does not contain "free" electrons and the g factor differs from the free spin value g_e . The reason for this deviation is an additional contribution of the orbital angular momentum L to the spin S , which is caused by spin-orbit coupling with the surrounding of the spin centre. As a consequence, the magnetic moment of an unpaired electron in a real chemical system is not, in general, exactly antiparallel to the effective spin. Furthermore, the scalar g_e value has to be replaced by a symmetrical (3x3) matrix (or a second rank tensor) due to an anisotropic interaction of the orbital angular momentum with the external field (orbital Zeeman interaction). Therefore, the resonance condition may be written as

$$h\nu = \mathbf{g} \cdot \mu_B \cdot \mathbf{B} \quad (\text{Eq. 2.6})$$

The matrix \mathbf{g} is characteristic for the respective spin centre under investigation. The tensorial nature of \mathbf{g} causes a dependence of the resonant field on the orientation of the crystal axes in the magnetic field. For a single crystal with only one type of paramagnetic centres of identical symmetry, the \mathbf{g} matrix may be built up by EPR spectrum acquisition for various orientations of the crystal axes with respect to the magnetic field. The respective principal values (g_{xx} , g_{yy} , g_{zz}) may then be obtained by diagonalisation of the matrix. This operation is equivalent to the rotation of the axes of the paramagnetic centre in order to coincide with the laboratory axes defined by the magnetic field (Fig. 2.2).

The local symmetry of a spin centre is reflected in the nature of the respective \mathbf{g} matrix. The system displayed in Fig. 2.2 shows *axial symmetry*. The principal values of the \mathbf{g} matrix are $g_{zz} = g_{||}$ and $g_{xx} = g_{yy} = g_{\perp}$ and may be derived from the resonant fields B_z and $B_x = B_y$,

respectively. The orientation in Fig. 2.2b is called “parallel”, those in Fig. 2.2c and d are called “perpendicular”. For every other orientation of the spin centre with respect to the magnetic field the g -values lie in between g_{\perp} and g_{\parallel} (Fig. 2.2a). For a spin centre of *cubic symmetry* the principal g values are equal ($g_{xx} = g_{yy} = g_{zz}$), in the case of *rhombic symmetry* they have distinct values.

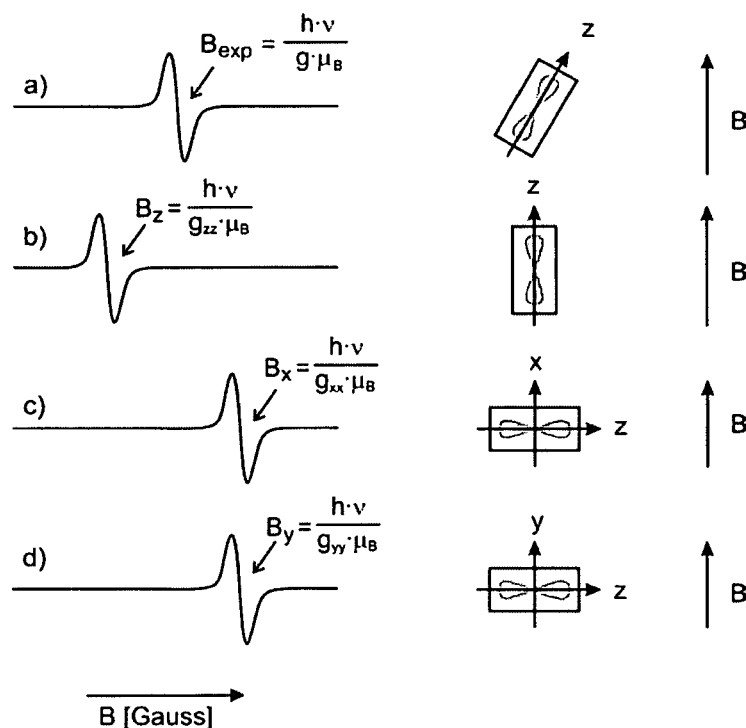


Fig. 2.2: Simulated EPR spectra of a paramagnetic centre in a single crystal for different orientations of the crystal in the magnetic field. The directions of the radical axes and of the crystal axes are arbitrarily assumed to be the same.

2.1.2. Hyperfine interaction

When a nucleus of non-zero nuclear spin is in close vicinity to the paramagnetic electron centre, a splitting of the respective signal in the EPR spectrum can be observed. This splitting is due to the hyperfine interaction between the magnetic moment of the unpaired electron and the magnetic moment associated with the nuclear spin. Different types of electron spin – nuclear spin interactions have to be considered depending on whether the distribution of the respective electron is spherical or non-spherical. Unpaired s electrons give rise to an isotropic hyperfine coupling due to their finite probability at the nucleus (Fermi contact interaction). For paramagnetic electrons in p , d or f orbitals, on the other hand, no Fermi contact occurs due to the nodes of the corresponding wave functions at the nucleus. In this case the hyperfine interaction is a consequence of the non-spherical symmetry of the

orbitals and can be described in terms of the classical dipolar interaction between magnetic moments. The dipol-dipol interaction is anisotropic – it depends on the orientation of the orbital with respect to the applied magnetic field.

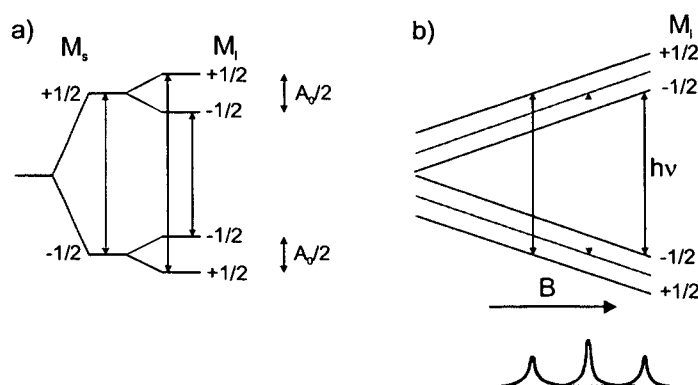


Fig. 2.3: Electron Zeeman levels for an electron spin $S = \frac{1}{2}$ with hyperfine coupling to a nuclear spin with $I = \frac{1}{2}$ and the resulting EPR transitions a) at constant magnetic field and b) as a function of magnetic field.

In the simplest case of an electron magnetic moment of $S = \frac{1}{2}$ and a nuclear magnetic moment of $I = \frac{1}{2}$, each of the electron Zeeman levels is split into two (according to the multiplicity determined by $2I+1$). If a magnetic field is applied, the allowed EPR transitions between the split energy levels are given by the selection rules (Fig. 2.3):

$$\Delta M_S = \pm 1 \quad \text{and} \quad \Delta M_I = 0.$$

M_S and M_I are the magnetic quantum numbers of the electron and the nucleus, respectively. As a consequence of the hyperfine interaction the transition is split into a doublet (Fig. 2.3b). The resonance magnetic fields are given by

$$B_i = (h\nu \pm A_0/2)/g_e \cdot \mu_B \quad (\text{Eq. 2.7})$$

and $a_0 = A_0/g_e \mu_B$ is called the hyperfine coupling constant (in magnetic field units).

2.1.3. Powder spectra

A polycrystalline sample is constituted by a large number of single crystals, which are randomly oriented with respect to the external magnetic field. As a consequence, the respective powder spectrum represents the superposition of a large number of single crystal

spectra corresponding to all possible crystal orientations. The signal is spread over a resonant field range, which is determined by the values of the principal g components and its shape is strongly influenced by the local symmetry of the spin centre (Fig. 2.4 and Fig. 2.5).

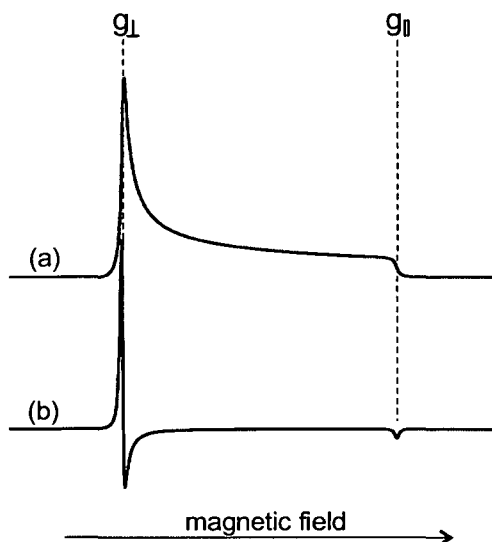


Fig. 2.4: Computer simulation of a powder pattern with axial symmetry of the spin centre: a) absorption spectrum, b) 1st derivative of the absorption spectrum.

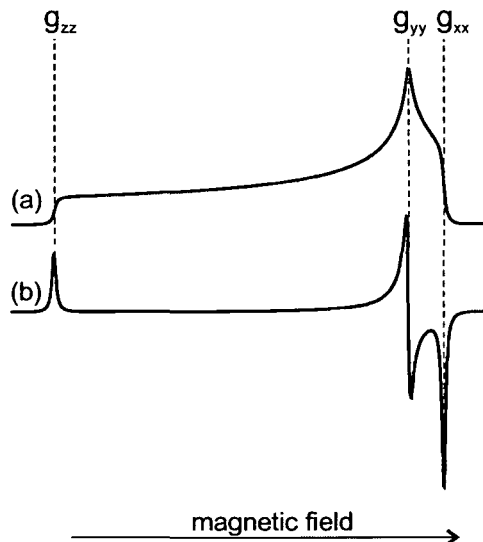


Fig. 2.5: Computer simulation of a powder pattern with rhombic symmetry of the spin centre: a) absorption spectrum, b) 1st derivative of the absorption spectrum.

2.2. Fourier transform infrared (FTIR) spectroscopy

2.2.1. Hydroxyl groups as intrinsic surface probes

The investigation of surface hydroxyl groups by FTIR spectroscopy is a very powerful tool concerning the characterization of polycrystalline metal oxides. The position of the respective stretching frequency, which ranges between 3200 cm^{-1} and 3750 cm^{-1} , gives direct evidence for the chemical and physical properties of the local environment. Furthermore, the thermal stability of hydroxyl groups provides direct information on the reactivity of the respective adsorption site.

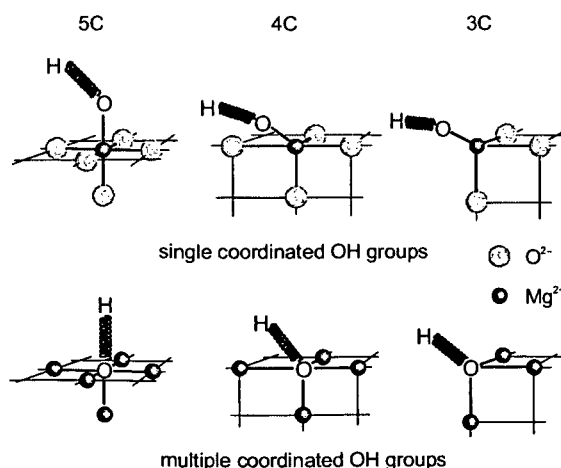


Fig. 2.6: Different types of OH groups of single and multiple coordination on the surface of MgO.

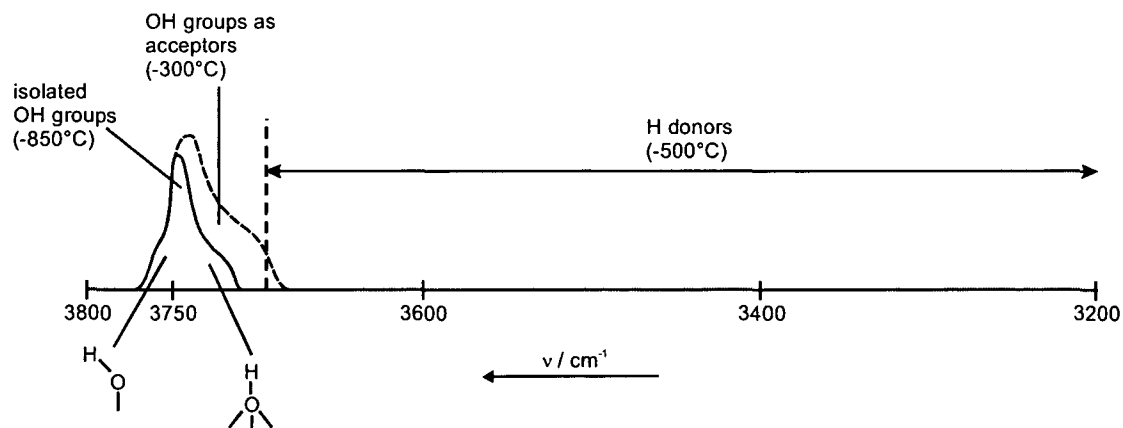


Fig. 2.7: Assignment of the stretching frequencies to different types of OH groups.

The coordination of an OH group significantly influences the position of its absorption band in the infrared spectrum. Considering as example the surface of MgO, Fig. 2.6 shows a selection of differently coordinated and isolated hydroxyl groups. Unfortunately, a definitive assignment of single OH bands to characteristic low coordinated sites is not possible. This is due to the fact that also ions of the second coordination sphere significantly contribute to the local potential and, therefore, to the frequency of the respective vibration. As a consequence of the large variety of different local structures on the surface of polycrystalline material, broadened and overlapping bands are observed in the respective IR spectra.

A significant influence on the frequency of OH bands may also be caused by hydrogen bonding. The character of hydrogen bridged OH groups is determined by their donor or acceptor properties⁵⁸. Both types are shifted to lower frequencies, whereby the extent of the frequency shift is larger for H-donors than for H-acceptors (Fig. 2.7). The strength of the H-bonding of a proton donor determines both the position of the band in the IR spectrum and the isotopic ratio ($\nu_{\text{OH}}/\nu_{\text{OD}}$). The smaller the value of the isotopic ratio, the stronger is the bonding. This effect results from an enhanced anharmonicity of the potential curve by the interaction of the oscillator with another group (Fig. 2.8).

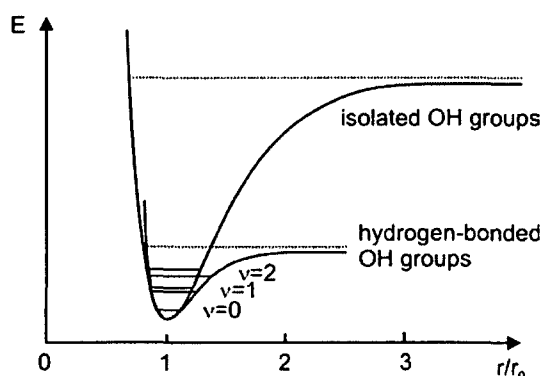


Fig. 2.8: Potential curve of isolated and hydrogen-bonded OH groups [58].

2.2.2. Free carrier absorption

In the present study infrared spectroscopy was not only applied to investigate surface probe molecules (vibrational spectroscopy), but was used also in order to study the so-called free carrier absorption (optical spectroscopy).

In addition to the fundamental band-to-band transition, optical absorption in semiconductors can take place also via indirect transitions within the same energy band (intraband transitions). This absorption requires the presence of charge carriers, which are free to move inside a band (e.g. electrons in the conduction band) and may, therefore, interact with the ambient. Free carrier absorption is observed in the infrared region of the electromagnetic spectrum and is characterized by a monotonic, structureless spectrum, which grows as λ^p , where p can range from 1.5 to 3.5 and λ is the photon wavelength. The quantum theory of free carrier absorption is based on the same considerations as the theory of the fundamental absorption in an indirect band gap material (Sec. 1.3.1, Fig. 1.12). In order to satisfy the conservation of momentum, a momentum scattering process is required in addition to the photon absorption. The change in momentum is provided by interaction of the electron with lattice phonons (Fig. 2.9).

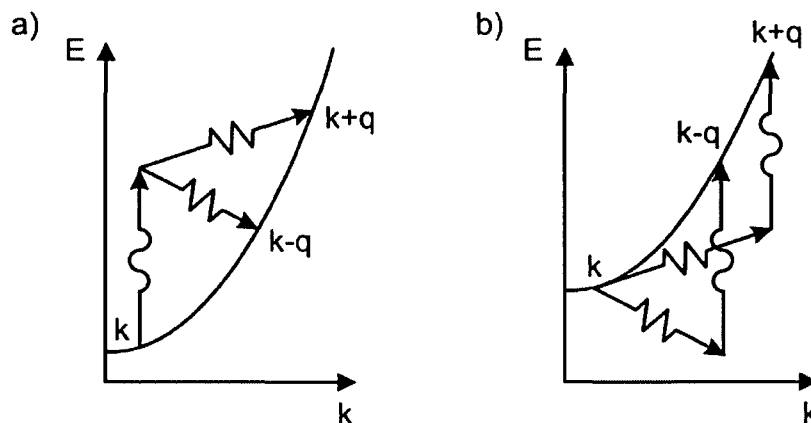


Fig. 2.9: Free carrier absorption only takes place when a momentum scattering process is involved in addition to photon absorption. In (a) a photon is absorbed first and then phonon emission or absorption occurs. In (b) phonon scattering occurs first [46].

2.3. UV/Vis diffuse reflectance spectroscopy

Reflectance spectroscopy, in general, is based on the analysis of the spectrum of light, which is reflected from a sample in a specific direction. Two fundamentally different reflection modes may be distinguished: regular reflectance is observed on an ideal flat surface, whereas rough surfaces and powder samples give rise to diffuse reflectance.

Single scattering on particles is observed, if the distance between the scattering centres is at least twice the diameter of the particles. In this case, the angular dispersion of the remittance is anisotropic. In polycrystalline materials, however, the condition for single scattering is not fulfilled and the particles may not be seen as independent scattering centres any more. As a consequence, multiple scattering phenomena occur and an isotropic angular distribution of the remitted radiation is observed.

In a diffuse reflectance experiment, the phenomena of absorption and scattering are always observed at the same time. However, a phenomenological theory developed by Kubelka and Munk⁵⁹ shows, that the remittance of a sample depends only on the ratio between the coefficients of absorbance and scattering, but not on their absolute values. By assuming the scattering coefficient to be constant in a given energy range, the Kubelka-Munk model allows to derive an absorbance spectrum from the respective reflectance spectrum. The positions of reflectance minima correspond to the maxima of absorption of the sample.

3. Experimental details

3.1. Sample preparation

3.1.1. Synthesis of TiO₂ nanocrystals by metal organic chemical vapour deposition

Nanocrystalline TiO₂ particles are produced in a flow reactor system by the metal organic chemical vapour deposition (MOCVD) method (Fig. 3.1)⁶⁰. The liquid precursor (titanium isopropoxide) is evaporated at temperatures in the range between 115-145°C at a reduced pressure of 5-20 mbar. Argon (0.84 standard litres per minute) is used as carrier gas, which transports the gaseous metal organic precursor to the furnace zone (T = 800°C). In this area the metal oxide particles are formed by the thermal precursor decomposition. After leaving the reaction zone the particles are cooled to room temperature and are finally deposited in a stainless steel net. The temperature gradient in the cooling step is in the range of 10⁴ °C/s.

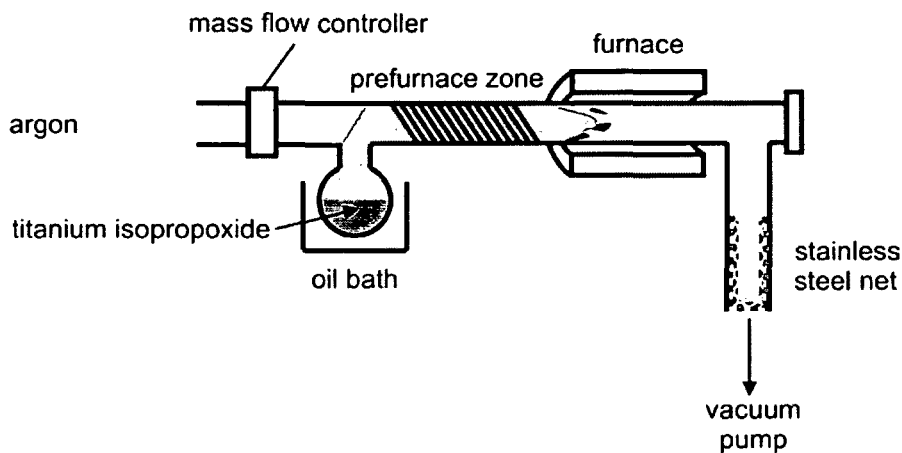


Fig. 3.1: Schematic representation of the MOCVD reactor for the production of high surface area TiO₂.

The native product powder is then transferred on air into the respective sample cells. The sample is gradually annealed (10 °C/min) to 600°C under high vacuum conditions ($P < 10^{-6}$ mbar) for 2 h and oxidized with 20 mbar O₂ for two reasons: 1) to remove organic remnants from the precursor material and 2) to guarantee the stoichiometric composition of the oxide. Annealing at $T > 600^{\circ}\text{C}$ at high vacuum conditions causes the removal of oxygen from the

TiO₂ lattice. A non-stoichiometric (reduced) sample is formed. However, unless otherwise noted, oxidized samples are used in this study.

Since a complete dehydroxylation cannot be achieved at 600 °C and high vacuum conditions, the TiO₂ samples retain some isolated Ti-OH groups after sample activation.

In the transmission electron micrograph (TEM), the majority of crystallites display a highly irregular shape after such activation (Fig. 3.2a). The size of the nanocrystals ranges from 8 to 18 nm (Fig. 3.2b) with a mean diameter of 13 nm. The specific surface area deduced from the TEM mean diameter value is 121 m²·g⁻¹ and is in accordance with nitrogen physisorption measurements (*t*N₂) of 130±13 m²·g⁻¹. Extensive particle agglomeration may, therefore, be excluded. X-ray diffraction patterns of the oxidized sample reveal the anatase crystal structure exclusively. However, sample treatment at temperatures *T* > 700°C results in the appearance of the rutile structure (Fig. 1.2).

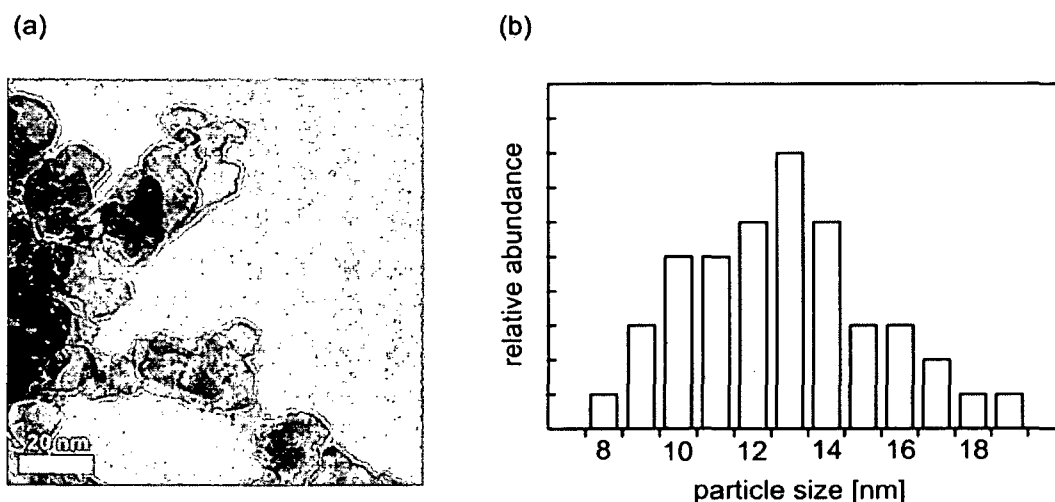


Fig. 3.2: (a) Transmission electron micrograph and (b) particle size distribution of anatase TiO₂ after oxidative treatment at 600°C. About 50 particles from 4 different sample regions were observed for plot 1b.

3.1.2. Synthesis of MgO nanocubes by chemical vapour deposition (CVD)

For metals with vapour pressures as high as 1 mbar at temperatures below 1000°C, the respective oxides may be synthesized using the pure metal as the precursor in a flow reactor as shown in Fig. 3.3⁶¹. The limitation to 1000°C is given by the thermal stability of the quartz tubes and of the furnaces, which are operated via resistive heating. Due to this limitation, this sample preparation method is only used for the production of alkaline earth metal oxides.

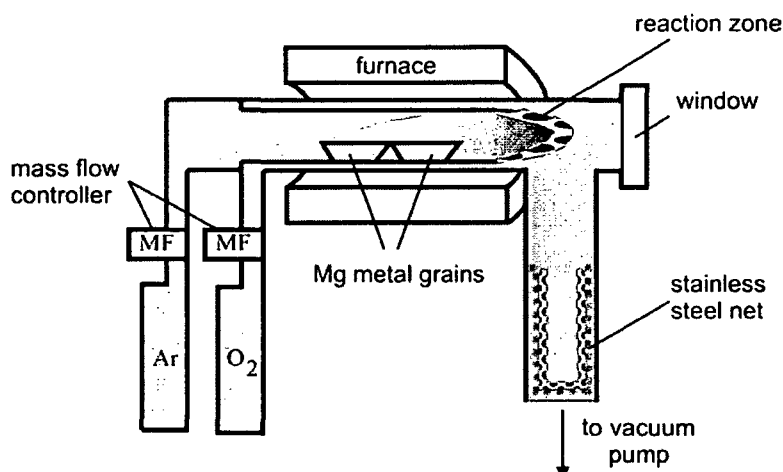


Fig. 3.3: Schematic representation of the CVD reactor for the production of MgO nanocubes.

However, the big advantage of this preparation technique is the absence of organic remnants on the native sample powder in contrast to the method discussed for TiO₂ in Sec. 3.1.1.

The flow reactor system consists of two quartz glass tubes. In the inner tube, metal grains are thermally evaporated and transported by Argon (1.22 standard litres per minute) as carrier gas to the reaction zone at the end of the inner tube. There, the metal vapour gets in contact with oxygen gas (80 standard cubic centimetres per minute), which flows through the outer quartz glass tube, and reacts immediately under the formation of nanoscale metal oxide particles. A rotary vane pump maintains a pressure between 5 to 20 mbar in the reactor system. In the constant gas flow, the metal oxide particles leave the hot reaction zone (620°C) and are cooled down to room temperature with cooling rates of 10⁴ °C/s. Finally they are collected at a stainless steel net.

Prior to any experiment, the sample is heated to 600°C and treated with oxygen to burn away organic contaminants originating from oil of the vacuum pumps. After pumping the oxygen off, the final annealing temperature of 900°C is kept for an interval of at least 1 h. After vacuum annealing no evidence for electronically reduced centres such as in the case of TiO₂ was observed. The activation procedure results in a complete dehydroxylation of the surface. The surface area corresponds to 300 m²·g⁻¹ as determined by nitrogen physisorption measurements (tN₂).

The transmission electron micrographs of CVD MgO after thermal treatment reveal a cubic shape of the respective nanocrystals (Fig. 3.4) with the (100) face being the dominant surface plane. The nanocubes exhibit a sharp size distribution with edge lengths ranging from 2 to 10 nm and a mean edge length of 5 nm. However, the size of the respective nanocubes strongly depends on the CVD conditions and samples with average edge lengths in the range between 3 nm and 10 nm may be obtained replacing oxygen by other oxidizing agents like N₂O or dry air⁵¹.

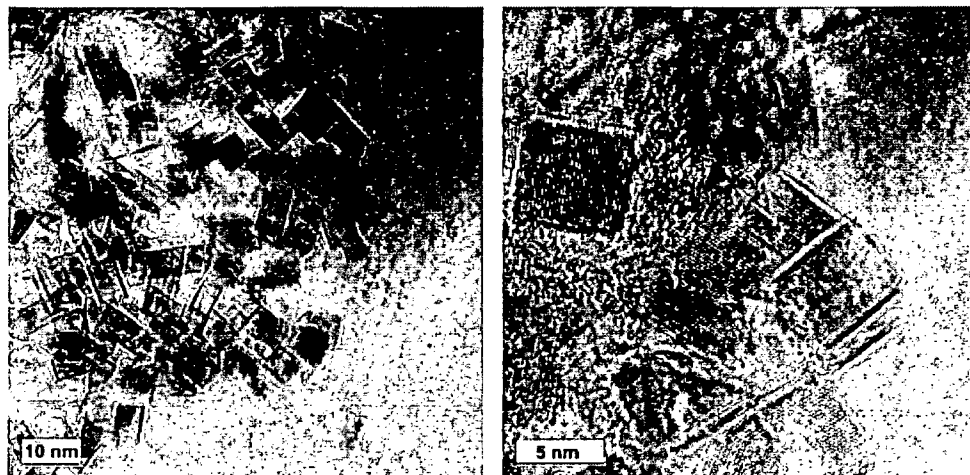


Fig. 3.4: Transmission electron micrographs of CVD MgO after thermal pretreatment at 900°C in vacuo.

3.2. Electron paramagnetic resonance (EPR) spectroscopy

X-band EPR measurements were performed on a Bruker EMX 10/12 spectrometer. Typical values of the microwave frequency are 9.2 – 9.8 GHz, which implies a resonance magnetic field strength of the order of 0.34 T (3400 Gauss). A Bruker ER 4102ST standard rectangular resonant cavity in the TE₁₀₂ mode was used in all measurements. According to the required resolution the modulation amplitude varied between 0.3 and 2 Gauss. Unless otherwise noted, the microwave power was chosen in a range, where no saturation of the respective EPR transition occurs.

The powder sample is contained within a Suprasil quartz glass tube connected to an appropriate high vacuum pumping system consisting of a turbomolecular pump in conjunction with a rotary vane pump. This allows for thermal sample activation and UV irradiation in situ at pressures less than 10⁻⁶ mbar. Spectrum acquisition was performed in the temperature range 298 K > T > 77 K. The measurements at 77 K and in the temperature

range $T = 90 \text{ K} - 140 \text{ K}$ were carried out in a Dewar filled with liquid nitrogen (Fig. 3.5) or an ER 4131 VT Variable Temperature Accessory, respectively. In order to maximize signal-to-noise ratios, between 10 to 50 scans were acquired for one spectrum. EPR computer simulations were performed using the SIM 14S program⁶². The g values were determined on the basis of a DPPH standard.

An aperture in the EPR cavity allows one to study the time evolution of paramagnetic electron and hole centres during UV exposure (Fig. 3.5). UV light reflections at the gold-plated inner surface of the resonant cavity in conjunction with the diffuse reflectance of the powder facilitate uniform light exposure of the cylindrical sample tube from all directions. The concentration of spins was measured in situ at a fixed resonance magnetic field value of the respective EPR transitions during UV irradiation⁶³. A 300 W Xe lamp (Oriel) was used as an UV source. The light beam was passed through a water filter to exclude IR contributions from the excitation spectrum. Light power was measured with a bolometer (International Light).

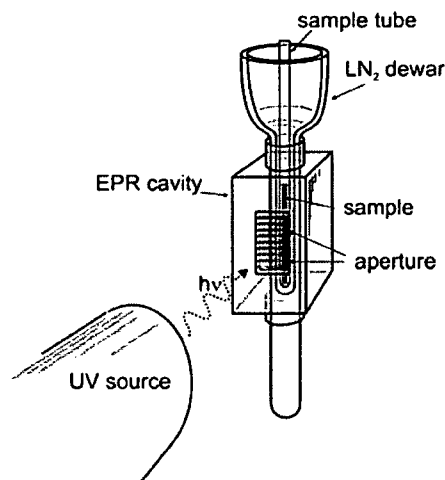


Fig. 3.5: Experimental set-up for simultaneous UV exposure and EPR measurement at 77 K.

3.3. Fourier transform infrared (FTIR) spectroscopy

3.3.1. Measurements at room temperature

The IR measurements were performed on a high resolution Fourier transform infrared spectrometer type IFS 113v, Bruker Analytik. 300 scans were accumulated for one spectrum to obtain a reasonable signal-to-noise ratio. Measurements were performed in the mid-IR spectral region ($400 - 4000 \text{ cm}^{-1}$) and the resolution was 3 cm^{-1} . The transmitted radiation was detected with a MCT detector operated at 77 K.

The sample cell used in this study allows thermal activation and subsequent infrared spectroscopic investigation of the sample in high vacuum (Fig. 3.6). The high vacuum pumping system consists of a turbomolecular pump in conjunction with a rotary vane pump and guarantees pressures $P < 10^{-6}$ mbar. The samples were pressed to self-supported pellets and placed in a sample holder. A gas supply assembly is attached to the vacuum line and allows adsorption/desorption experiments at room temperature. A more detailed description of the experimental set-up is given in Refs. 64 and 65.

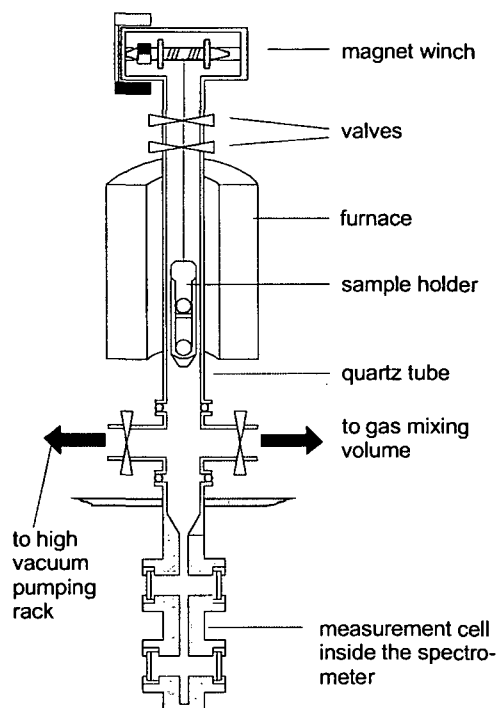


Fig. 3.6: Schematic of the IR transmission cell for measurements at room temperature.

A spectrum of the activated sample at room temperature was used as reference. The spectra were acquired using the OPUS software (Bruker) and further data manipulation was performed with the GRAMS (Galactic Industries Corporation) software package.

3.3.2. In situ cell for measurements in the presence of UV light at low temperatures

In order to acquire IR spectra during UV exposure at $T = 140$ K, a modified experimental set-up developed by Yates and co-workers was used (Fig. 3.7)⁶⁷. The powdered sample is hydraulically pressed at 12000 lbs/in² into the middle of a fine-tungsten support grid⁶⁶ as a circular spot 7 mm in diameter. The upper position on the grid is empty and is used for the background absorbance measurements in the same experiment. A type-K thermocouple is spot-welded to the top-centre region of the grid. The grid is held by nickel heating and cooling supports in the centre of the dual beam IR-UV photoreactor. The grid is mounted in the cell at a 45° angle to the IR beam, so that irradiation of the grid with ultraviolet light directed perpendicularly to the IR beam can be carried out without making a geometrical change. Electrical ohmic heating and cooling with liquid nitrogen permit the temperature of the grid to be set within the range 100-1000 K. The cell gas outlet is connected to a stainless steel ultrahigh vacuum system. Both a Pfeiffer Vacuum 60 L/s turbomolecular pump and a

Varian 20 L/s ion pump are used to maintain the base pressure of the system below 10^{-7} Torr. A more detailed description of the IR-UV photoreactor may be found in reference 67.

For UV experiments a 350 W high-pressure Hg arc lamp (Oriel Corp.⁶⁸) was used as a light source. The light was filtered with a water filter to remove IR radiation. The UV light irradiance on the sample was 370 mW/cm^2 in the energy range 3.2 eV - 6.2 eV. The infrared spectrometer was a Mattson Research Series I FTIR, and all scans were made in the ratio mode with a resolution of 4 cm^{-1} . Typically, 50 scans were accumulated in each spectrum.

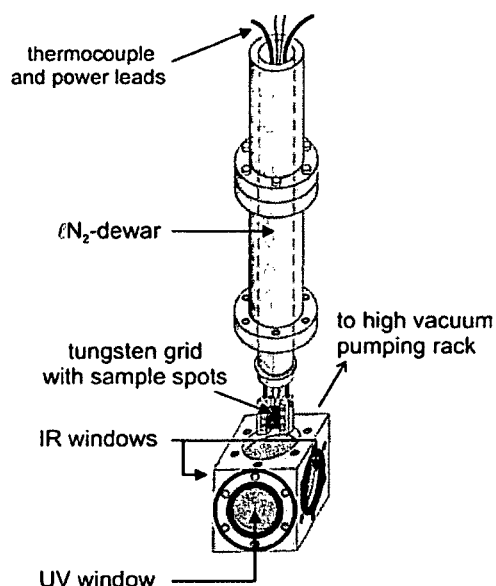


Fig. 3.7: Schematic of the in-situ cell for measurements at 140 K in the presence of UV light [67]

3.4. UV/Vis diffuse reflectance spectroscopy

For UV/Vis diffuse reflectance measurements, the MgO powder was placed in a high vacuum tight quartz cell with optical windows made of Suprasil. Thermal activation, as well as adsorption and desorption steps were performed by connecting the cell to a vacuum line that

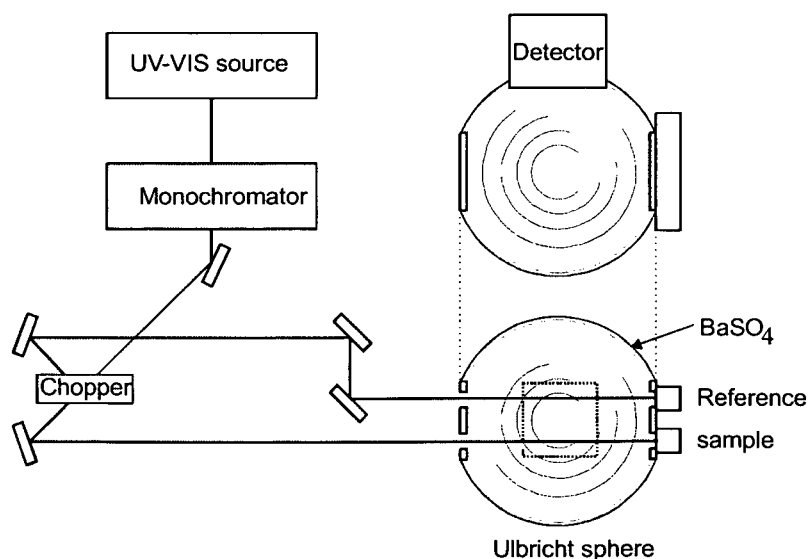


Fig. 3.8: Schematic set-up of a DR UV/Vis spectrometer.

guarantees pressures less than 10^{-6} mbar. The UV spectra were acquired using a Perkin Elmer Lambda 15 spectrophotometer equipped with an integrating sphere. BaSO₄ was used as a reference. The experimental set-up of the UV/Vis spectrometer is shown in Fig. 3.8.

3.5. Reagents

Reagent	Purity / %	Distributor
Mg grains	99.98	Johnson Matthey GmbH
H ₂	99.999	Messer Griessheim
D ₂	99.7	Messer Griessheim
O ₂	99.998	Messer Griessheim
N ₂ O	99.5	Messer Griessheim
Ar	99.999	Messer Griessheim
titanium(IV)- isopropoxide	97	Sigma-Aldrich

PHOTOCHEMISTRY AND PHOTOPHYSICS ON TiO₂ NANOCRYSTALS

Ultraviolet light-induced electron-hole pair excitations in anatase TiO₂ powders were studied by a combination of electron paramagnetic resonance (EPR) and infrared (IR) spectroscopy measurements. During continuous UV irradiation in the mW·cm⁻² range, photogenerated electrons are either trapped at localized sites giving paramagnetic Ti³⁺ centres, or remain in the conduction band as EPR silent species, which may be observed by their IR absorption (Sec. 4).

Using low temperatures ($T < 140$ K) to reduce the rate of the electron-hole recombination processes, trapped electrons and conduction band electrons exhibit lifetimes of hours. The EPR-detected holes produced by photoexcitation are O⁻ species, produced from lattice O²⁻ ions. It is found that under high vacuum conditions, the major fraction of photoexcited electrons remains in the conduction band. The UV light irradiance is crucial during these experiments, since the efficiency of charge carrier separation sensitively depends on temperature. Local heating of the crystallites at irradiances > 3 mW·cm⁻² was observed and attributed to enhanced recombination of photogenerated charge carriers. At 298 K, all stable hole and electron states are lost from TiO₂ (Sec. 5).

Defect sites produced by oxygen removal during annealing of anatase TiO₂ are found to produce a Ti³⁺ EPR spectrum identical to that of trapped electrons, which originate from photoexcitation of oxidized TiO₂. Reduced TiO₂, produced by annealing in vacuum, has been shown to be less efficient in hole trapping than oxidized TiO₂ (Sec. 4).

Compared to photoactivation experiments in vacuum at $P < 10^{-6}$ mbar the presence of O₂ enhances the concentration of persistently trapped electron and hole centres by a factor of 10 due to the formation of adsorbed O₂⁻ species. The photoadsorption of oxygen was also tracked quantitatively by pressure measurements, and the number of trapped charges, hole centres and O₂⁻, was found to correspond to maximal 10 electron-hole pairs per TiO₂ nanocrystal at $T = 140$ K. On the other hand, photoactivation at $P < 10^{-6}$ mbar results in only one efficiently separated electron-hole pair per particle (Sec. 6).

4. Light-induced charge separation in TiO₂ nanocrystals

4.1. Introduction

The light-induced production of charge carriers is the basic requirement for the application of semiconductors in photocatalysis^{9,10,69} and photovoltaic cells⁷⁰. Once produced, the charge carriers become trapped, either in shallow traps (ST) or in deep traps (DT), but they can also recombine, radiatively or non-radiatively, dissipating the input energy as heat. Charge carriers can react with electron donors or acceptors adsorbed on the surface of the photocatalyst^{9,10,71,72}. Recombination and trapping of charge carriers accompanied by the competition with interfacial charge transfer determine the overall quantum efficiency^{8-10,69-71}. For photocatalytic systems in which the rate-limiting step is interfacial charge transfer, improved charge separation and inhibition of charge carrier recombination is essential for enhancing the overall quantum efficiency of the photocatalytic process^{9,10,69,73}.

Titanium dioxide, TiO₂, is the photoactive semiconductor most thoroughly investigated in the literature^{8-10,69-71,74} because it provides the best compromise between photocatalytic performance and stability in most chemical environments; it is also inexpensive and non toxic. Most commercial TiO₂ powdered catalysts are a mixture of rutile and anatase and there is growing evidence, which suggests that anatase is more active than rutile for oxidative detoxification reactions⁷⁵. Anatase is the thermodynamically less stable polymorph, but the more probable phase when the TiO₂ grain size is around 10 nm as expected from surface energy calculations^{16,76}. The physical and chemical properties of TiO₂ depend largely on the surface for particles a few nanometers in size^{9,15,76}. This is particularly true for charge carrier trapping, because many defect states associated with the surface act as trapping sites^{1,2,19}. However, on polycrystalline surfaces their exact nature and function are not well established.

X-ray absorption spectroscopy (XAS) studies⁷⁷ and electron paramagnetic resonance (EPR) spectroscopy revealed that the surface states, which trap photogenerated electrons, can be coordinatively unsaturated Ti sites formed upon reduction and surface reconstruction of TiO₂ nanoparticles. Characteristic EPR signals attributed to Ti³⁺ ions in the $g < 2$ region were observed on anatase TiO₂ samples after excitation of the solid with UV light⁷⁸⁻⁸⁰.

Trapping and recombination of photogenerated charge carriers have been studied by UV/Vis absorption spectroscopy techniques, following transient absorption in the spectral range

between the visible and the infrared region. Serpone et al.⁸¹ and Bowman et al.^{82,83} have investigated independently the primary events after band gap excitation of titanium dioxide colloids using picosecond and even sub-picosecond time resolution. Transient absorption spectra show that localization (trapping) of photogenerated electrons occurs at times below 10^{-10} s. In the larger time regime, about 10^{-9} s after the excitation pulse, more than 90% of the photogenerated charge pairs have recombined^{82,83}. Bahnemann et al.⁸⁴ also observed transient UV/Vis absorption following band-gap excitation of TiO₂ colloids. They assigned absorption bands centred at 1.9 eV and 2.8 eV to trapped electrons and holes, respectively.

Transient absorption in the IR from 3000 cm^{-1} ($\sim 0.37\text{ eV}$) to 900 cm^{-1} ($\sim 0.15\text{ eV}$) is reported for TiO₂ powders after they were exposed to UV laser pulses. This effect, attributed to photogenerated electrons in or close to the conduction band (Fig. 4.1a), was studied by Onishi and coworkers⁸⁵ on a timescale of $5 \cdot 10^{-8}\text{ s} - 1\text{ s}$ after excitation. Lifetimes associated with decay kinetics between 10^{-7} s to 10^{-1} s were observed. In addition, an IR *emission* observed between 1200 to 900 cm^{-1} ($0.13\text{ eV} \pm 0.02\text{ eV}$) occurs on a time scale of milliseconds and was attributed to the relaxation of electron-hole pairs. The above studies show that the recombination rate strongly depends on the medium in which the solid is embedded (e.g. in liquid solution or for TiO₂ dried under high vacuum conditions) and can vary by 13 orders of magnitude⁸²⁻⁸⁷.

The above examples deal with relaxation phenomena in TiO₂ (charge-carrier recombination) following laser pulse excitation. However, less direct spectroscopic information is available for photoinduced processes involving lower light irradiances, such as continuous wave excitation in the power range of $\text{mW}\cdot\text{cm}^{-2}$, which corresponds to the usually applied photocatalytic conditions. Hoffmann and coworkers⁸⁶ characterized the decay of free and trapped electrons in polycrystalline TiO₂ (Degussa P25) by diffuse reflectance IR spectroscopy after bandgap excitation with a high pressure Xe lamp as the UV source. After partial sample dehydroxylation, the lifetimes of these conduction band electrons are on a time scale of minutes and are controlled by the hydroxylation state of the sample. Furthermore, the infrared absorption intensity of hydroxyl stretching bands is sensitive to the electric fields caused by trapped electrons⁸⁷. Apparently, surface hydroxyl groups actively participate in irreversible charge carrier trapping but also mediate charge recombination^{71,87,88}.

As indicated above, EPR is an exceptionally useful technique to probe photogenerated charge carriers in oxide particles. It allows one not only to monitor trapped electrons in localized states (Fig. 4.1b), but also electron holes trapped at oxygen anion O⁻ centres which

are EPR active^{53,77-80,89}. In addition, adsorbed surface radicals like superoxide anion O₂⁻, formed by interfacial electron transfer from trapped electron sites to adsorbed O₂⁹⁰ can easily be identified on the basis of their spin Hamiltonian parameters⁹¹. Though much is published about EPR on samples after UV exposure^{77,78,80,92-96}, to the best of our knowledge nothing is known regarding the evolution of paramagnetic species in TiO₂ during continuous UV exposure and as a function of excitation time.

The objective of the present investigation is to compare, for the first time, charge trapping effects that occur during photoexcitation with supra bandgap photon energy using two complementary techniques, EPR and IR spectroscopy. Whereas localized states such as holes trapped at oxygen anions (O⁻) and electrons trapped at coordinatively unsaturated cations (Ti³⁺ formation) are accessible to EPR spectroscopy (Fig. 4.1), delocalised and EPR silent electrons in the conduction band may be traced by their IR absorption from their electronic excitation within the conduction band in the infrared region. It will be shown that during UV excitation of anatase TiO₂ nanoparticles at 140 K and below, only a limited fraction of electrons are actually localized as Ti³⁺ states while the major fraction remains in the conduction band even after discontinuing UV excitation. The performance of these experiments under high vacuum conditions and low temperatures slows down the charge-carrier recombination and allows one to track the process of light-induced charge separation on a timescale of seconds to minutes. Moreover, after discontinuation of UV exposure, the charge separation can be stored for hours when TiO₂ particles are electronically isolated and kept at low temperatures. A comparison between photoexcitation effects on oxidized and on thermally-reduced TiO₂ particles will be made, and primary interfacial charge transfer steps that involve photogenerated electrons and O₂ (a known electron scavenger) will be addressed by this combined spectroscopic approach.

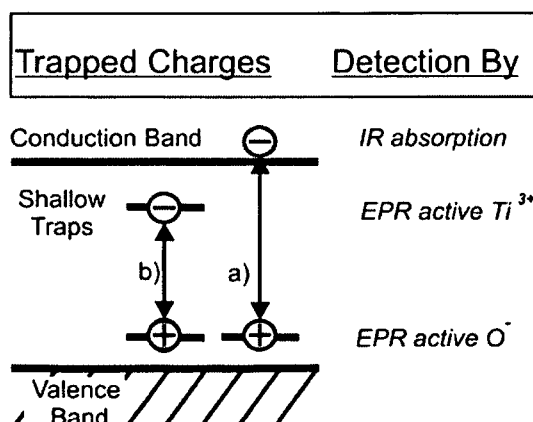


Fig. 4.1: Scheme of UV induced charge separation in TiO₂. Electrons from the valence band can either be trapped (a) by defect states, which are located close to the conduction band (shallow traps), or (b) in the conduction band where they produce absorption in the IR region. Electron paramagnetic resonance spectroscopy detects both electrons in shallow traps, Ti³⁺, and hole centres, O⁻.

4.2. Results and Discussion

4.2.1. Photoexcitation of oxidized TiO₂ nanoparticles

a) EPR measurements of the photoexcitation process

After oxidative treatment at 870 K and cooling to 90 K, TiO₂ particles do not contain any paramagnetic sites as evidenced by a flat line shown in Fig. 4.2a. However, after 20 minutes of polychromatic UV exposure ($I = 0.7 \text{ mW}\cdot\text{cm}^{-2}$ with $h\nu > 3.2 \text{ eV}$) at this temperature, two types of EPR features were measured (Fig. 4.2b): a low field signal assigned to holes trapped at oxygen ions, $\text{O}^{\cdot-}$ ^{63,97-99} with g tensor components at $g_{\perp} = 2.0121$ and $g_{\parallel} = 2.0046$ and a second feature which is essentially composed of two distinct signals attributed to trapped electrons at Ti^{3+} sites with $g_{\perp} = 1.9640$ and $g_{\parallel} = 1.9495$ (Ti^{3+} I) and $g_{\perp} = 1.990$ and $g_{\parallel} = 1.9600$ (Ti^{3+} II) (Tab. 4.1)*. These values are in perfect agreement with the literature and can be readily assigned to localized electrons in anatase at different and so far unspecified

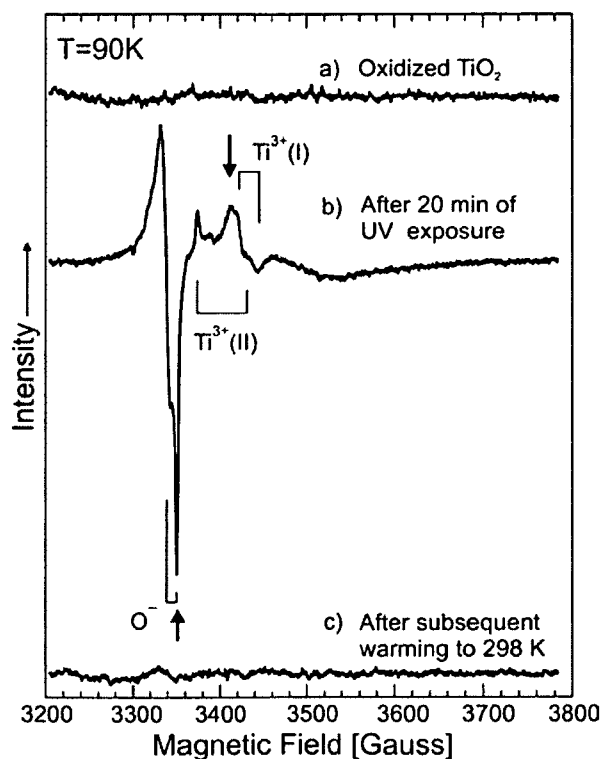


Fig. 4. 2: EPR spectra of oxidized anatase nanoparticles (a) before and (b) after 20 minutes of UV exposure at 90 K ($I = 0.7 \text{ mW}\cdot\text{cm}^{-2}$ with $h\nu > 3.2 \text{ eV}$). Subsequent warming to 298 K (c) leads to the complete annihilation of paramagnetic charge carriers.

* The ratio of $\text{O}^{\cdot-}$ and Ti^{3+} concentrations is not represented properly in these spectra. A high microwave power (100 mW) had to be used in order to make visible the Ti^{3+} centres. At these MW powers the $\text{O}^{\cdot-}$ species already shows considerable saturation behaviour and is therefore underestimated by a factor of ~ 12 .

sites^{79,80,91,95}. EPR scans, performed at different times during UV excitation, did not reveal any additional paramagnetic signals. On the basis of these observations and in accordance with literature¹⁰ we specify the following charge transfer steps:



Whereas the injection of electrons into the conduction band and concomitantly the generation of holes in the valence band occur in femtosecond times^{10,81-83}, the trapping processes of electrons (Eq. 4.2) and holes (Eq. 4.3) are observed on the time scale of seconds to minutes (Fig. 4.3). This was carried out by tracking the intensity values at magnetic fields indicated with arrows in Fig. 4.2. Both curves in Fig. 4.3 clearly show a monotonous growth within the first ~100 s; the Ti³⁺ signal levels thereafter at a constant value* while the O⁻ signal approaches steady state after ~500 s. The relative ratio of Ti³⁺ and

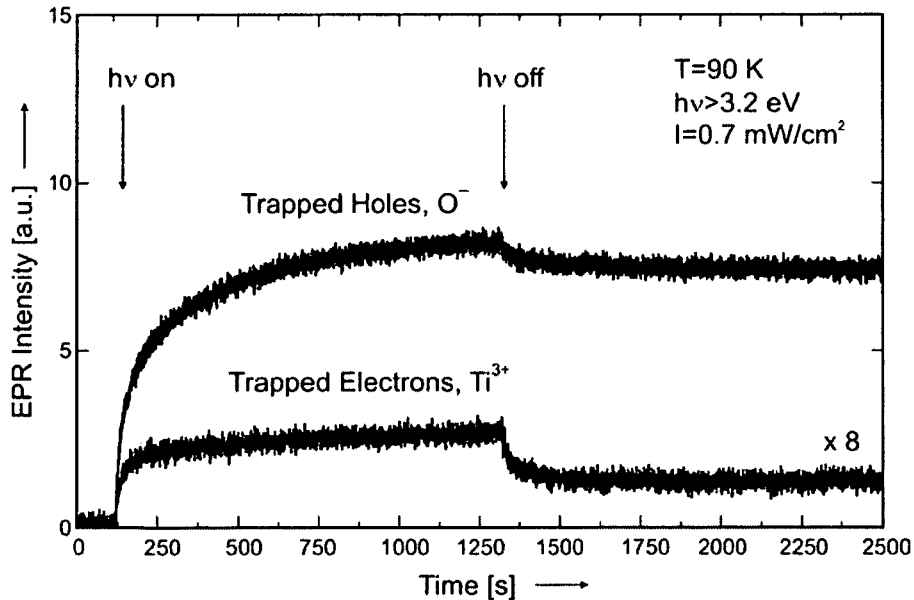


Fig. 4.3: Concentration of O⁻ and Ti³⁺ centres as a function of UV exposure time ($I = 0.7 \text{ mW}\cdot\text{cm}^{-2}$ with $h\nu > 3.2 \text{ eV}$).

* That only a monotonous increase in the Ti³⁺ signal is observed in the course of UV exposure time, indicates that a second light induced electron transfer step: $\text{Ti}^{3+} + e^- \rightarrow \text{Ti}^{2+}$ does not occur in the course of continuous UV exposure.

O⁻ signal intensities varies from sample to sample, but at 90 K, the Ti³⁺ concentration never exceeds 10 percent of the concentration of trapped holes. This implies that the majority of the photoexcited electrons remain in the conduction band in oxidized TiO₂. The persistent filling of the conduction band with electrons is in line with photoconductivity measurements performed on TiO₂ powders upon excitation with comparable light irradiances^{100,101}.

Discontinuation of UV excitation after 1200 seconds results in signal depletion to about 90% of the maximum intensity achieved during irradiation for O⁻ and 50% for the Ti³⁺ signals as shown in Fig. 4.3. Then, the signals remain constant on a time scale of hours (no significant signal decrease was observed after 5 hours of sample storage at 90 K). To characterize the correlation between hole and electron centres, the O⁻ concentration was plotted against the Ti³⁺ concentration as UV exposure time increases at 90 K (Fig. 4.4). The significant deviation from linearity at higher spin concentrations suggests that only a limited number of photoexcited and trapped electrons occupy localized states (Fig. 4.1b). A considerable fraction must remain in the conduction band as delocalised and EPR silent species^{86,87,100,101} (Fig. 4.1a).

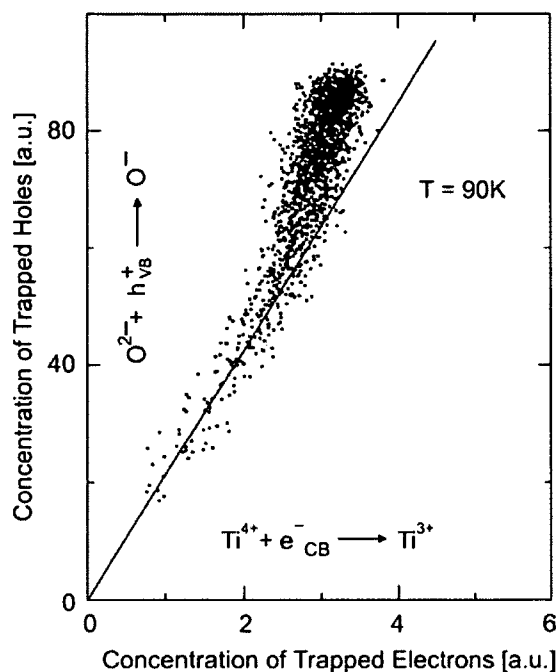


Fig. 4.4: Correlation of O⁻ and Ti³⁺ EPR signal intensity as a function of UV exposure time at 90 K ($I = 0.7 \text{ mW}\cdot\text{cm}^{-2}$ with $h\nu > 3.2 \text{ eV}$). The intensity values for the Ti³⁺ and O⁻ species were normalized with respect to equal integral intensities of the respective spin centre signals.

Light-induced filling of the conduction band with electrons is the exclusive process observed when the experiment is performed at temperatures somewhat higher than 90 K: no Ti³⁺ centres were observed during photoexcitation at 140 K, even after subsequent cooling to 90 K. Although the O⁻ signal (not shown) obtained at 140 K is lower in intensity, it follows essentially the same kinetics as in the experiment performed at 90 K. Because the relative Ti³⁺ concentration has a significant dependence on temperature between 90 K and 140 K, activation energies around 0.01 eV are estimated for the process of diffusion of shallowly trapped electrons from their Ti³⁺ trapping sites, followed by recombination with holes. Sample excitation at 298 K does not produce any paramagnetic states at all. Also, raising the

temperature to 298 K after UV excitation at 90 K (Fig. 4.2c) results in the complete annihilation of photogenerated charges.

b) IR measurements of the photoexcitation process

Illumination of oxidized TiO₂ particles with polychromatic UV light (3.2 eV - 6.2 eV, $I = 370 \text{ mW}\cdot\text{cm}^{-2}$) at 140 K in vacuum causes a pronounced increase in the background IR absorbance over the entire region from 3000 to 1000 cm^{-1} as the UV exposure time increases (Fig. 4.5a – 4.5b). Subtraction of the spectrum before the beginning of irradiation (Fig. 4.5a) from the excited state spectrum (Fig. 4.5b) produces a structureless broad IR absorption background feature, monotonically strengthened with decreasing wavenumber from 3000 to 1000 cm^{-1} (Fig. 4.5c). The spectrum 4.5c was ratioed to the spectrum of an empty tungsten grid under the same conditions of illumination to exclude possible background effects originating from the grid. The spectral shape of the background feature (Fig. 4.5c) does not change with UV exposure time. To track signal changes as a function of UV exposure, IR spectra were acquired every 30 s and a representative absorbance value at 2000 cm^{-1} was plotted against irradiation time.

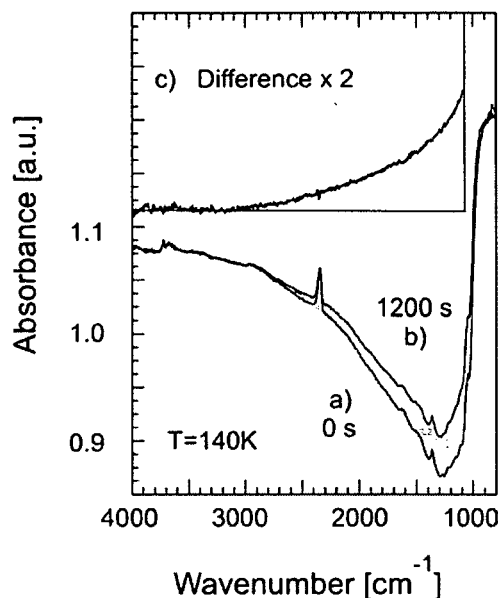


Fig. 4.5: IR spectra of oxidized anatase TiO₂ particles at 140 K: (a) before and (b) after 20 minutes of UV exposure. The inset (c) represents the difference (b-a).

Fig. 4.6 presents the IR signal changes obtained at 140 K in vacuum during the illumination and dark periods. The resulting profile qualitatively corresponds to the excitation curve measured by EPR for the evolution of O[•]. Upon discontinuing the UV exposure, the IR signal continuously decreases.

This type of broad and structureless IR absorption has been reported by several authors for TiO₂ after UV excitation^{45,46,85-87,102}. According to Yamakata et al.^{85,102} photogenerated electrons trapped in shallow gap states are the source of the transient IR absorption via two routes: the intra-CB transition of free electrons thermally excited from the trap state, and the direct optical transition from the trap state to the CB. Szczepankiewicz et al. have recently shown⁸⁷ that during illumination of TiO₂ surfaces under vacuum, the electron trapping and annihilation is slowed such that the free electrons, typically monitored by ultrafast techniques^{10,81-85}, maintain an unusually long lifetime of minutes to hours. Complementary to

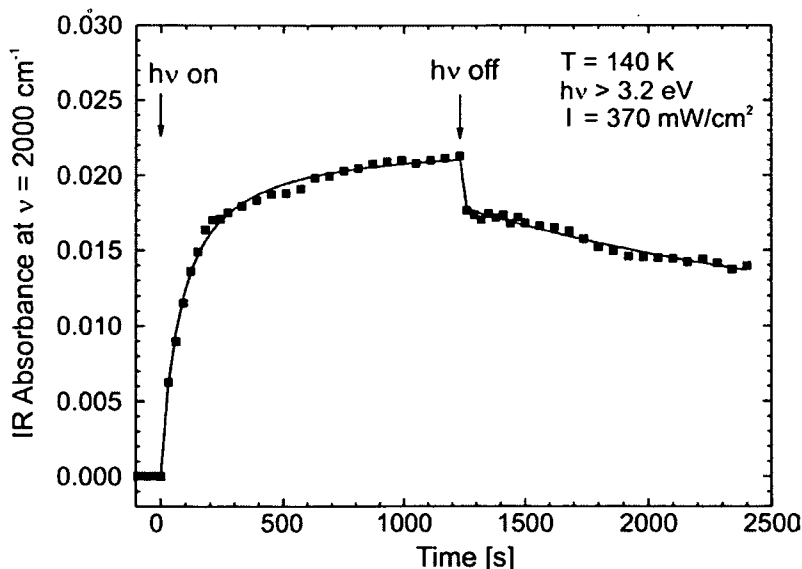


Fig. 4.6: Time resolved IR absorbance at 2000 cm^{-1} during and after UV exposure at 140 K.

the EPR results of this study where no paramagnetic electron states were observed after excitation at 140 K, we demonstrate that a continuous IR absorption points to the presence of electrons in the conduction band which are kept separated from their complementary holes even after discontinuation of UV exposure. A possible explanation for such a persistent storage of electrons comes from Emeline et al.¹⁰³: because the translation symmetry in spatially confined nanoparticles is only valid for the short-length crystal units, the number of states forming the band states is very limited compared to a bulk crystal. As a consequence the communication between different states in the conduction band is much less effective and the decay of electrons can be significantly delayed. When the TiO₂ temperature was raised to 298 K (not shown in Fig. 4.6), the slowly decaying IR absorption immediately decreased to a level close to the original baseline. As in the corresponding EPR experiment (Fig. 4.2c) charge carrier separation was reversed via thermally-induced charge carrier recombination.

4.2.2. The effect of oxygen on charge separation

a) EPR measurements of the effect of O₂

In order to elucidate the effect oxygen has on both trapped electrons and on the process of electron trapping, the following EPR experiments were performed at 140 K. UV exposure in vacuum was found to produce paramagnetic hole centres exclusively (O[•] radicals, Fig. 4.7a); centres due to Ti³⁺ have recombined with O[•] holes at 140 K. Contacting the pre-irradiated powder with 5 Torr O₂ in the dark followed by evacuation leads to significant changes in the spectrum (Fig. 4.7b). Photoexcitation of TiO₂ nanoparticles in the presence of oxygen at the

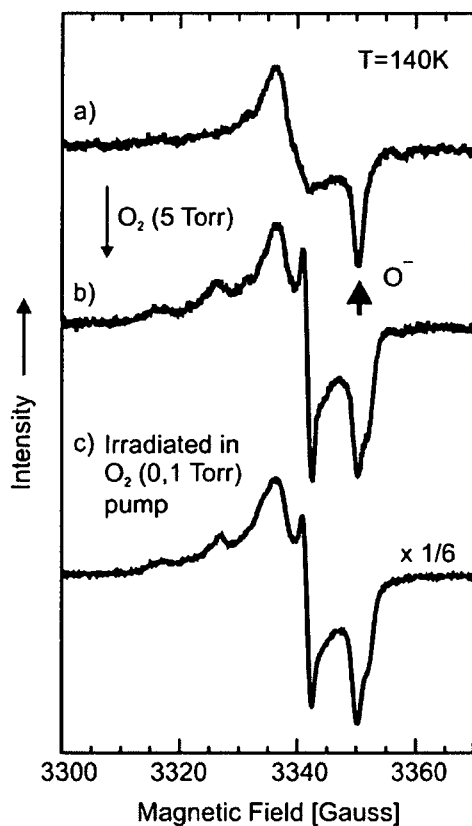


Fig. 4.7: (a) EPR spectra of oxidized anatase TiO₂ particles after 20 minutes UV exposure at 140 K; (b) after exposure to 5 mbar O₂ followed by evacuation; (c) the spectrum was measured after 20 minutes UV exposure at 140 K in the presence of O₂.

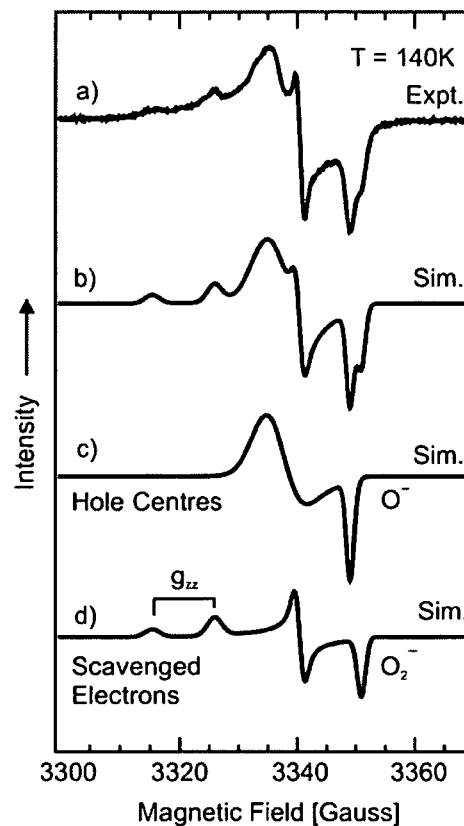


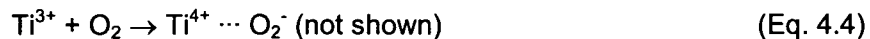
Fig. 4.8: (a) Experimental EPR spectrum after 20 minutes UV exposure at 140 K, (from Figure 8c); (b) the simulation result. Figures 9c and d display the simulated O⁻ and O₂⁻ components of spectrum (b) respectively.

same temperature and subsequent evacuation (Fig. 4.7c), produces essentially the same result as observed for O₂ addition to pre-irradiated TiO₂ (Fig. 4.7b). However, the overall intensity is enhanced by a factor of 6 when irradiation occurs in the presence of O₂.

In order to understand the spectral lines observed in Figs. 4.7b and 4.7c as a result of the presence of O₂, a simulation was performed as shown in Fig. 4.8. The results of the best fit are given in Fig. 4.8b and the *g* values corresponding to the paramagnetic species are listed in Tab. 4.1. In addition to O⁻ (Fig. 4.8c) a set of two additional features (Fig. 4.8d) contribute to the total spectrum. The associated *g* values are easily assigned to adsorbed superoxy species O₂^{-89,91,99,104}. In EPR applied to the investigation of oxide surfaces, this type of oxygen radical is a widely used probe for cationic surface sites because it has specific resonances within the low field region (*g*_{zz}), indicative of the local crystal fields at the respective O₂⁻ adsorption sites¹⁰⁴. In the present case, two different surface cations serve as

adsorption sites for the newly-formed oxygen radicals as evidenced by their resonances at $g_{zz} = 2.025$, and $g_{zz} = 2.018$. (Fig. 4.8a and 4.8d).

To summarize, the effect of oxygen on light induced charge separation at temperatures $T > 90$ K can be described by an interfacial transfer of electrons out of both localized paramagnetic states and the conduction band to molecular oxygen by Eqs. 4.4 and 4.5:



These reactions are exothermic (-42 kJ/ mol) and additionally favoured by Coulombic stabilization of the lattice⁹¹.

Simulation of the superimposed feature in Figs. 4.8a and 4.8b into its O^- (Fig. 4.8c) and O_2^- related signals (Fig. 4.8d) reveal comparable intensities of $\text{O}^- : \text{O}_2^-$ of $\sim 1.1 : 1$ and thus, an equal concentration of holes trapped by lattice O^{2-} to produce O^- , and electrons scavenged by molecular oxygen. This is true for O_2 addition to pre-irradiated TiO_2 in the dark (Fig. 4.7b) as well as for UV excitation in the presence of O_2 (Fig. 4.7c). When photogenerated electrons are trapped by adsorbed O_2 species, the state of charge separation can be maintained even after warming to room temperature. The clear proportionality between trapped holes (O^-) and scavenged electrons (O_2^-) and the lack of other oxygen adducts such as $\text{O}^- \cdots \text{O}_2$ as reported by others⁹⁹ point to the fact that even under UV exposure the O_2^- species remain on the surface as undissociated species.

A comparison of the O_2^- EPR intensities for O_2 post-addition to irradiated TiO_2 with TiO_2 irradiated in the presence of $\text{O}_2(\text{g})$ shows that the presence of $\text{O}_2(\text{g})$ produces a 6-fold enhancement of the O_2^- surface concentration. The fraction of the long-lived trapped charges, which are transferred to post-adsorbed O_2 is $\sim 17\%$ as judged by the O_2 titration experiment. When $\text{O}_2(\text{g})$ is continuously supplied to the interface during irradiation in $\text{O}_2(\text{g})$, an additional $\sim 83\%$ of O_2^- is produced as all photoexcited electrons are transferred to O_2 . In both experiments, the two O_2^- species are produced in the same ratio.

b) IR measurements of the effect of O_2

Fig. 4.9 shows the effect of adding O_2 (5 Torr) to the irradiated TiO_2 surface at 140 K using the intensity of the IR background at 2000cm^{-1} as a detector for trapped conduction band electrons. The experiment is similar to the 140 K EPR experiment of Figs. 4.7a and 4.7b. The decrease in IR absorbance at 2000cm^{-1} indicates that O_2 efficiently removes long-lived

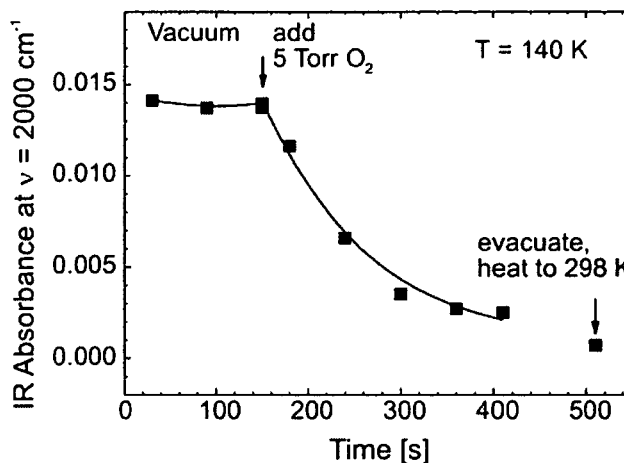


Fig. 4.9: IR background intensity at 2000 cm^{-1} of irradiated oxidized anatase TiO₂ particles upon addition of O₂ at 140 K.

trapped electron charge in the conduction band produced by UV excitation of TiO₂ in vacuum. Warming to 298 K results in a small additional removal of trapped electron charge, possibly by activated recombination.

4.2.3. Photoexcitation of reduced TiO₂ nanoparticles

Thermal treatment of TiO₂ nanoparticles in vacuum ($<10^{-5}$ Torr) and at 950 K produces an intense blue colour as the reduced solid is produced. The optical absorption in the range of visible light is accompanied by a pronounced increase in the background absorbance in the mid-IR region (Fig. 4.10b) compared to oxidized TiO₂ powder. As in the case of oxidized TiO₂ under UV excitation (Fig. 4.5c), the increased background (Fig. 4.10c) must be attributed to the production of conduction band electrons, which absorb IR light^{45,85-87}. For reduced TiO₂ produced by vacuum annealing, this profound change in the electronic structure is caused by the loss of lattice oxygen anions via desorption of molecular O₂ during thermal treatment.

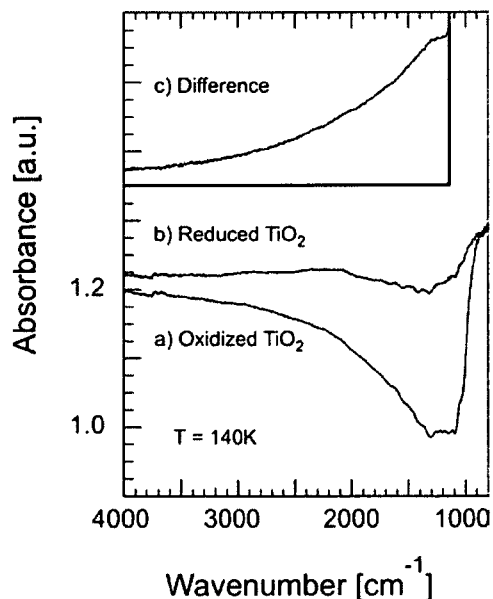


Fig. 4.10: Comparison of background IR behaviour of (a) oxidized TiO₂ and (b) reduced TiO₂ at 140 K.

IR measurements of the level of background absorbance during UV exposure of reduced anatase TiO₂ showed no change. After UV exposure the observed background absorbance was identical to that shown in Fig. 4.10c. Also increasing the temperature to 298 K did not produce any effect.

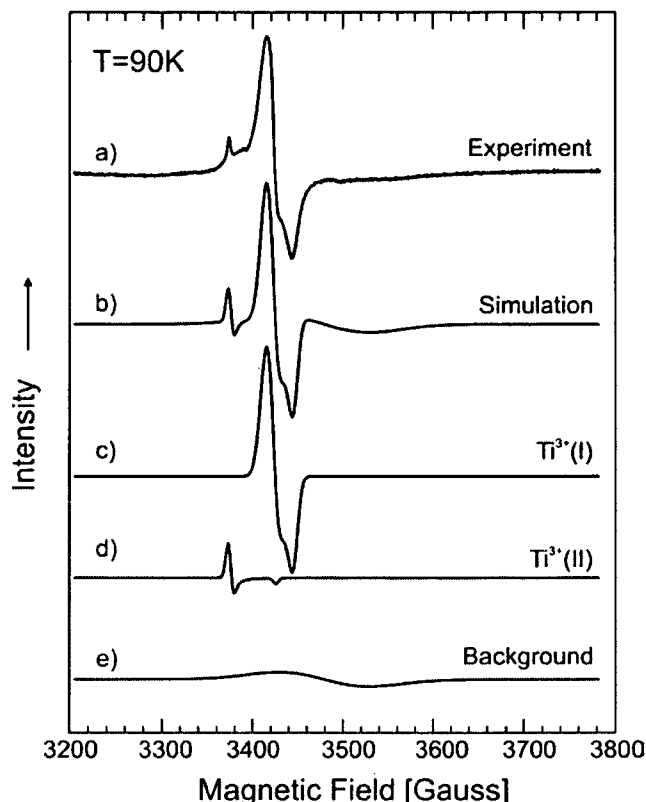


Fig. 4.11: (a) Experimental EPR spectrum of reduced TiO₂ at 90 K; (b) the simulation result. Figs. 4.11c – 4.11e display the simulated single components of spectrum (b).

A typical EPR spectrum of reduced anatase TiO₂ particles, shown in Fig. 4.11a contains essentially the same Ti³⁺ related signals (Figs. 4.11c and 4.11d) as observed for Ti³⁺ states in oxidized TiO₂ produced by UV excitation (Fig. 4.2b, Tab. 4.1). The spin concentration is, however, by a factor of 25 higher for reduced TiO₂. Upon 20 minutes light exposure with 0.7 mW·cm⁻², the signal intensity does not change (Figs. 4.12a and 4.12b) and only traces of O⁻ hole centre signals corresponding to less than 5% of the concentration measured on oxidized TiO₂ appear. These small EPR signals completely vanish after discontinuation of light exposure (Fig. 4.12b). The absence of trapped holes in reduced TiO₂ could be related to the deficiency of lattice oxygen trapping sites and/or the already high concentration of electrons in excited states either localized or delocalised (band filling mechanism)^{46,105}.

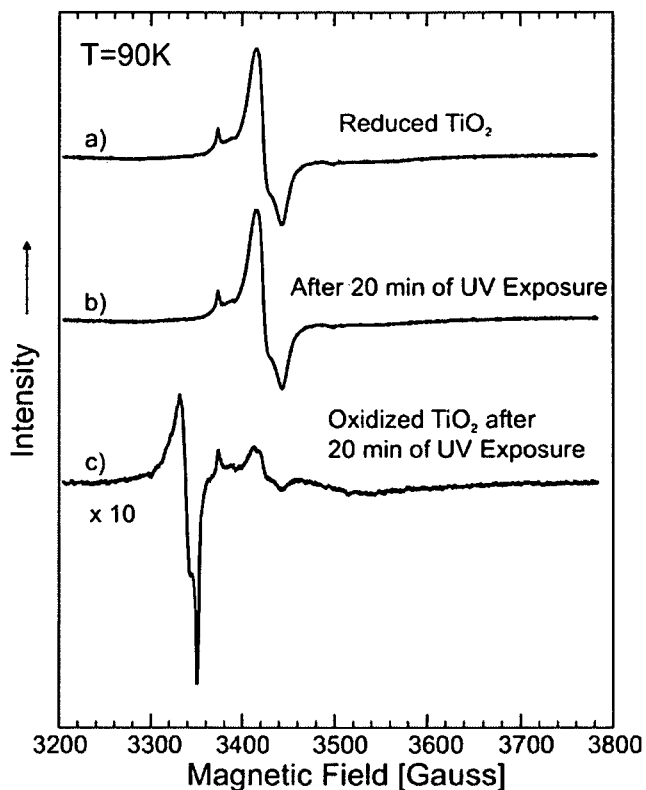


Fig. 4.12: The effect of UV irradiation on trapped electrons in reduced TiO₂ at 90 K.

When higher light irradiances ($> 5 \text{ mW}\cdot\text{cm}^{-2}$) are applied to reduced TiO₂, the Ti³⁺ centres also disappear (not shown). This bleaching process occurs already with photons of energy below 1.6 eV and indicates that the electronic states due to trapped electrons (Ti³⁺) are located within the band gap and can be ionised with significantly lower photon energies than required for electron-hole pair excitation across the 3.2 eV bandgap. Similar observations were made in an earlier study by Servicka et al.⁹³. In addition, Ghosh et al.¹⁰⁶ observed the presence of eight specific levels less than 1 eV below the conduction band. They speculated that these levels may be associated with Ti³⁺ ions at regular and interstitial sites and with colour centres. Gravelle et al.¹⁰⁷ tentatively assigned two Ti³⁺ ions to regular and interstitial lattice positions.

In addition, for reduced TiO₂, the Ti³⁺ signal in Fig. 4.11a as well as the optical absorptions in the visible and the mid IR are observed to disappear with O₂ exposure, producing the O₂⁻ ESR signal as expected from O₂ electron scavenging. These conclusions must be considered in connection with recent work where it was proposed that self-doping of anatase, by making it substoichiometric and producing large concentrations of Ti³⁺ sites, would lead to visible light activity for the degradation of pollutants^{108,109}. Since these photocatalytic reactions are usually carried in the presence of oxygen, which would oxidize the electronically reduced particles, a persistent visible activity is unlikely.

trapped holes - O ^{•-}	$g_{\perp} = 2.0121$	$g_{\parallel} = 2.0046$	
scavenged electrons - O ₂ ^{•-}			
O ₂ ^{•-} [I]	$g_{zz} = 2.0248$	$g_{yy} = 2.0096$	$g_{xx} = 2.0033$
O ₂ ^{•-} [II]	$g_{zz} = 2.0184$	$g_{yy} = 2.0096$	$g_{xx} = 2.0033$
trapped electrons - Ti ³⁺			
Ti ³⁺ [I]	$g_{\perp} = 1.9640$	$g_{\parallel} = 1.9495$	
Ti ³⁺ [II]	$g_{\perp} = 1.9900$	$g_{\parallel} = 1.9600$	
background	$g_{iso} = 1.9300$		

Tab. 4.1: Parameters of the g matrix for paramagnetic species isolated on anatase TiO₂ particles

4.2.4. Electrical conduction effects in photochemistry experiments – an hypothesis based on a comparison of ESR and IR studies

The TiO₂ powder, and its pretreatment, in the EPR and the IR experiments, was identical. To avoid warming of the EPR samples, the UV radiation power was maintained at 0.7 mW·cm⁻² whereas the IR experiments involved UV power of 370 mW·cm⁻². In the case of the EPR experiments, the TiO₂ is loosely contained in a quartz tube and electrically isolated from ground, whereas, for the IR measurements, the TiO₂ is compressed into a tungsten mesh support, which is in electrical contact with ground. The two different support methods are associated with different production and decay rates for the trapped charges. In the EPR experiments, the concentration of trapped holes and trapped electrons remained essentially constant for hours after irradiation was discontinued, whereas in the IR experiments, the trapped conduction-band electrons exhibited a monotonous loss of concentration after the UV radiation was discontinued. The difference in decay kinetics and in power levels required in the two experiments are postulated to be due to the different degrees of electrical isolation of the TiO₂ particles in the two experiments.

4.3. Conclusions

The following conclusions have been reached in this study:

1. Photogenerated electrons and holes are produced by band gap UV radiation on powdered anatase TiO₂. Trapped holes are detected as O^{•-} species, generated from

lattice O²⁻ in the valence band. The electrons are detected either as Ti³⁺ species or as electrons captured in the conduction band.

2. At 90 K, both electrons and holes are trapped for hours.
3. At 140 K, Ti³⁺ trapped electron states can recombine with holes, whereas conduction band electrons are stable.
4. At 298 K, all stable trapped hole and trapped electron states are lost from TiO₂.
5. The major fraction of photoexcited electrons remains in the conduction band, rather than being trapped as Ti³⁺ states.
6. The presence of O₂ during excitation at 140 K leads to the formation of two long-lived superoxy O₂⁻ states associated with different titanium cation sites on the surface.
7. Defect sites (Ti³⁺) produced by annealing TiO₂ are identical to the Ti³⁺ sites produced by photoexcitation.
8. The photoproduction of stable hole states in reduced TiO₂ is found to be very inefficient compared to those photoproduced in oxidized TiO₂.

5. Reversible hole trapping in anatase TiO₂ nanocrystals

5.1. Introduction

The interaction of light with oxide surfaces is of fundamental scientific interest, since it is directed to a wide range of technologies, e.g. optical and electronic devices, photovoltaics and photocatalysis. With respect to light-utilizing applications a key issue in the development of TiO₂-based materials is to cut down the recombination of light generated electron hole pairs by more efficient charge trapping. Although the literature on TiO₂ photochemistry is extensive, there are many open issues related to light induced phenomena without connection to already well-understood effects. For instance, the dynamics of photocatalytic reactions on TiO₂ particles have been studied extensively by transient absorption spectroscopies in the femtosecond to millisecond time range. The generation, relaxation and recombination processes of electrons and holes were identified due to their specific optical absorptions in the visible and infrared^{85,110}. These experiments are usually carried out by exciting colloidal samples with laser pulses. The optional presence of additional reactants during these processes allows for investigation of interfacial electron transfer processes^{72,81,84}. Little direct spectroscopic information, however, is available for photoinduced processes using light powers in the range of mW·cm⁻² of continuous light sources, which corresponds to technological applications. After sample dehydroxylation at elevated temperatures under high vacuum conditions ($p < 10^{-6}$ mbar), adsorption layers, which are present under ambient conditions can be excluded. Such conditions are indispensable for understanding the surface properties of the solid. Besides its fundamental role in interfacial reaction steps between charge carriers from the solid and molecules from the surrounding phase, the surface is of particular importance for charge carrier trapping. An ample body of evidence has been collected and shows that trapping sites are associated with surface defects, but their exact nature and location are not very well established^{9,10,19}.

For probing localized and, therefore, trapped charges, electron paramagnetic resonance (EPR) is an exceptionally useful technique. It allows not only to monitor electrons in localized states (Ti³⁺)¹¹¹, but also electron holes in form of O⁻ radicals are EPR active^{91,98}. In a previous study we investigated light induced electron-hole pair excitations in TiO₂ nanoparticles by a combination of electron paramagnetic resonance and infrared spectroscopy¹¹². We found that at temperatures below 140 K the majority of photoexcited electrons remain in the conduction band as EPR silent species on a time scale of hours and

only a small fraction of electrons is localized as Ti³⁺ species. On the other hand, electron holes get trapped by surface O²⁻ and produce paramagnetic O^{•-} species. It was also found, that the efficiency of charge separation critically depends on the temperature¹¹³.

In the present study we investigate the influence of the light irradiance on the hole trapping process.

5.2. Results and Discussion

No EPR signals are observed on oxidized samples. On the other hand, paramagnetic centres are generated by UV exposure ($I = 0.7 \text{ mW}\cdot\text{cm}^{-2}$ with $h\nu > 3.2 \text{ eV}$) at 77 K (Fig. 5.1a). Spectrum simulation (Fig. 5.1b) was carried out for g value determination (see Tab. 5.1) and the resonance signals are attributed to trapped holes O^{•-} (Fig. 5.1c)^{95,97,112} and trapped electrons Ti³⁺[I] and Ti³⁺[II] (Fig. 5.1d+e)^{79,80,114}. Furthermore, a broad background signal is observed (Fig. 5.1f)*. The reason for its huge width $> 100 \text{ G}$ could arise either from

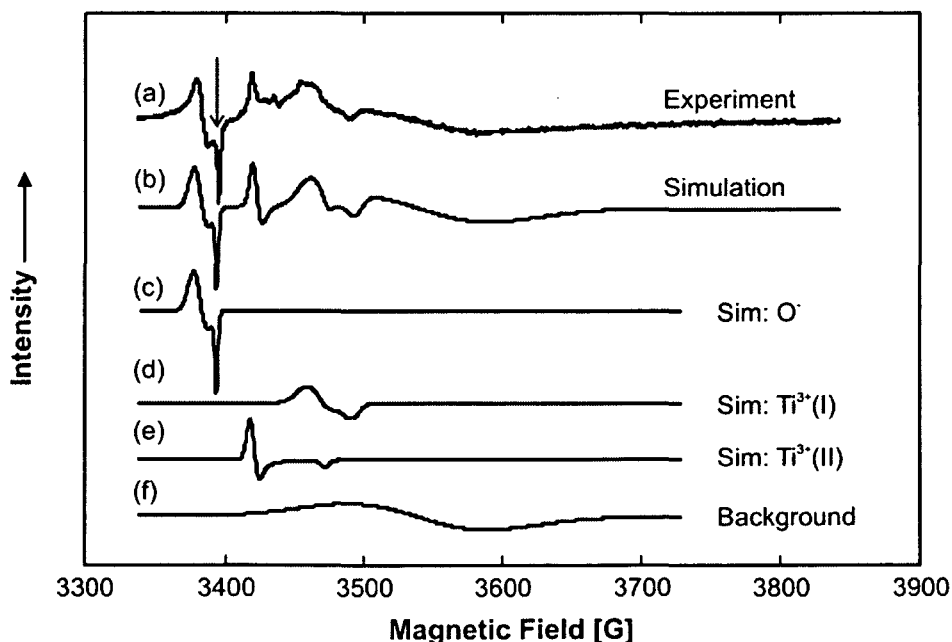


Fig. 5.1: (a) EPR spectra of TiO₂ nanocrystals after 20 minutes of UV exposure at 77 K and $P < 10^{-5}$ mbar and (b) the result of the spectrum simulation. (c)-(f) simulated single spectra of paramagnetic centres due to trapped electrons and holes.

* The ratio of O^{•-} and Ti³⁺ concentrations is not represented properly in these spectra. A high microwave power (100mW) had to be used in order to make visible the Ti³⁺ centres. At these MW powers the O^{•-} species already shows considerable saturation behaviour and is therefore underestimated by a factor of ~30.

the interaction of closely spaced electrons in Ti³⁺ dimers or from free electrons in the conduction band which give rise to a Dysonian lineshape. On the basis of a previous FTIR investigation¹¹² we attribute the broad background signal to conduction band electrons. Double integration of the respective single spectra reveals, that < 10 % of all photogenerated electrons are trapped at Ti³⁺ states whereas the majority remains in the conduction band. The following charge transfer steps can be specified for UV activation at 77 K:



trapped holes - O ⁻	$g_{\perp} = 2.0121$	$g_{\parallel} = 2.0046$
trapped electrons - Ti ³⁺		
Ti ³⁺ [I]	$g_{\perp} = 1.9640$	$g_{\parallel} = 1.9495$
Ti ³⁺ [II]	$g_{\perp} = 1.9900$	$g_{\parallel} = 1.9600$
background	$g_{\text{iso}} = 1.9300$	

Tab. 5.1: Parameters of the g matrix for paramagnetic species isolated on anatase TiO₂ particles.

The concentration of trapped hole states is shown in Fig. 5.2. At 77 K the state of light induced charge separation is essentially maintained in the dark. However, raising the temperature to 298 K causes the total annihilation of trapped holes and electrons and the original state before UV activation is restored. The signal shape of O⁻ centres in terms of line width does not change, neither during UV exposure nor after discontinuation of UV light.

Kinetic data for the evolution of O⁻ species as a function of light irradiance I are given in Fig. 5.3. Below 1.55 mW·cm⁻², the time-dependent accumulation of O⁻ centres ends up with a maximum concentration [O⁻]_{max}, which does not depend on the light irradiance. This limit has been reproducibly obtained on a sample with constant packing densities. Rotation of the sample tube by 180° during UV excitation did not change the number of spin centres proving that the nanocrystals of the cylindrical sample are uniformly exposed to the UV light. As will be outlined in more detail within the following section (Sec. 6) the number of trapped charges can be quantified on the basis of O₂-photoadsorption and it was found that the maximum

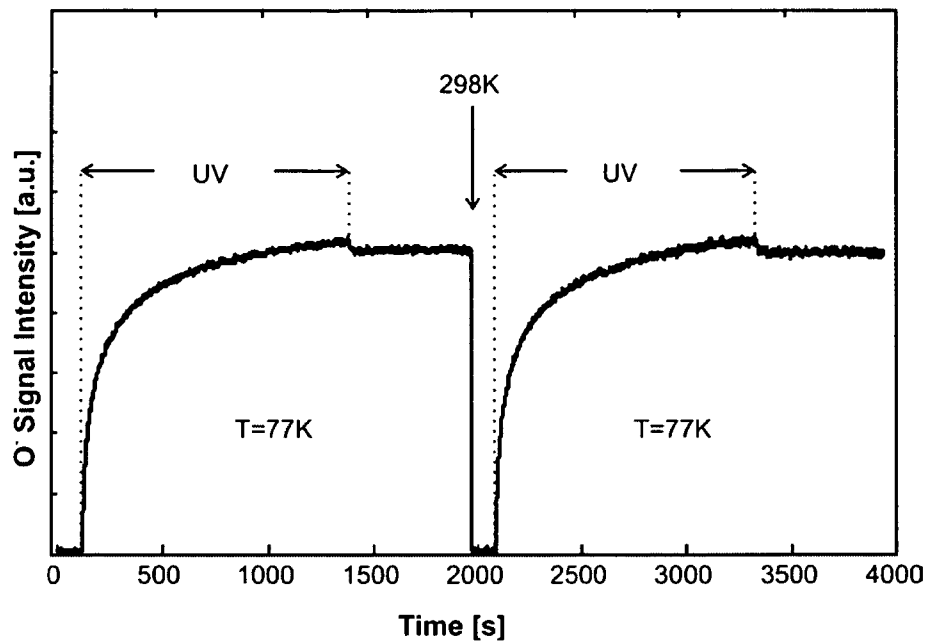


Fig. 5.2: Time evolution of trapped holes during UV exposure at 77 K. The arrow in Fig. 5.1a indicates the fixed resonance magnetic field value, which was chosen for the in situ measurement of the O⁻ concentration. Charge separation can be maintained upon discontinuation of UV light. Heating to 298 K completely restores the initial state before UV exposure.

concentration of trapped charges corresponds to one separated electron hole pair per TiO₂ nanocrystal¹¹³.

Irrespective of whether the excitation light was passed through a band pass between 3-4 eV (UG11) or not (0.5 eV to 6.2 eV), the kinetic profiles were identical for a given irradiance with supra band gap energy ($E > 3.2$ eV, Fig. 5.2). Consequently, we can exclude recombination processes, which are induced by photons with sub band gap energies ($3.2 \text{ eV} \geq E \geq 1.5 \text{ eV}$).

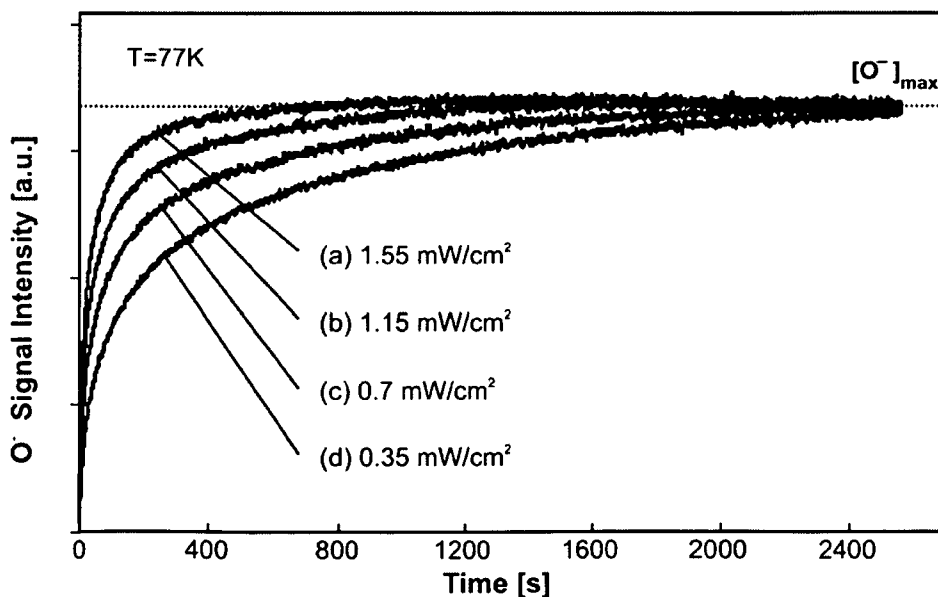


Fig. 5.3: Time evolution of trapped holes (O⁻) applying different light irradiances.

A secondary annihilation process of trapped charges becomes effective at light irradiances $I > 1.55 \text{ mW}\cdot\text{cm}^{-2}$. In Fig. 5.4 the evolution of hole centres at a light irradiance of $I = 6 \text{ mW}\cdot\text{cm}^{-2}$ (Fig. 5.4a) is compared with the curve obtained with $I = 0.35 \text{ mW}\cdot\text{cm}^{-2}$ (Fig. 5.4b). After an initial concentration built-up within the first 200 s a continuous depletion of trapped charges is observed thereafter. In order to understand this process, we checked the effect of discontinuation of UV exposure on the measured O^- signal. For $I = 0.35 \text{ mW}\cdot\text{cm}^{-2}$, the signal intensity drops by about 5 % of its original value $[\text{O}^-]_{\text{max}}$ and remains constant thereafter. However, for the experiment with $I = 6 \text{ mW}\cdot\text{cm}^{-2}$ a subsequent additional signal increase is measured. According to Curie's law, EPR signal intensities depend on acquisition temperature ($\text{intensity} \propto T^{-1}$). We, therefore, attribute the continuous signal decrease with ongoing UV exposure at $I = 6 \text{ mW}\cdot\text{cm}^{-2}$ to a temperature raise. On the other hand the intensity increase observed in the dark phase is associated with a cooling of the TiO₂ nanocrystals down to the 77 K of the cryostat. As mentioned above, IR radiation as a potential heating source was efficiently removed from the spectrum of the UV lamp by using a water filter. For this reason, we attribute the temperature rise to an UV light induced sample heating due to the non-radiative recombination of photogenerated electrons and holes. This effect, which is exactly the opposite of charge carrier trapping, occurs upon energy dissipation to the lattice, which corresponds to heat release. This recombination pathway is enhanced, when the maximum number of trapped charges has been reached. It is a well-known fact, that the majority of photogenerated electron/hole pairs undergo recombination within a few nanoseconds after their generation. Even at low temperatures only a small fraction of the energy introduced to the system by UV irradiation is stored within the sample by maintaining the charge separation state. The major fraction is released as heat rapidly and must be effectively removed from the sample by the cooling system (N_2 -Dewar) in order to guarantee a constant sample temperature throughout the experiment. However, at high light irradiances the cooling capacity of the system, which consists of /sample powder at high vacuum/quartz-tube/dewar filled with N_2 / does not meet these requirements. Consequently, the temperature of the TiO₂ nanoparticles increases as a function of UV exposure time and thermally induced detrapping and recombination of charges become effective. After turning off the UV light the sample cools down again to 77 K. It was shown in a previous study, that the efficiency of persistent separation of photogenerated electrons and holes critically depends on the sample temperature¹¹³. This effect was also observed by the experiment discussed by means of Fig. 5.2: a stable charge separation state generated at 77 K can be completely annihilated by increasing the temperature to 298 K. The effect of UV induced sample heating on the O^- signal intensity is, therefore, explained by the simultaneous occurrence of two independent physical phenomena:

- decrease of the EPR signal intensity as temperature increases according to Curie's law
- enhanced recombination of previously trapped holes with electrons via increase of the local temperature.

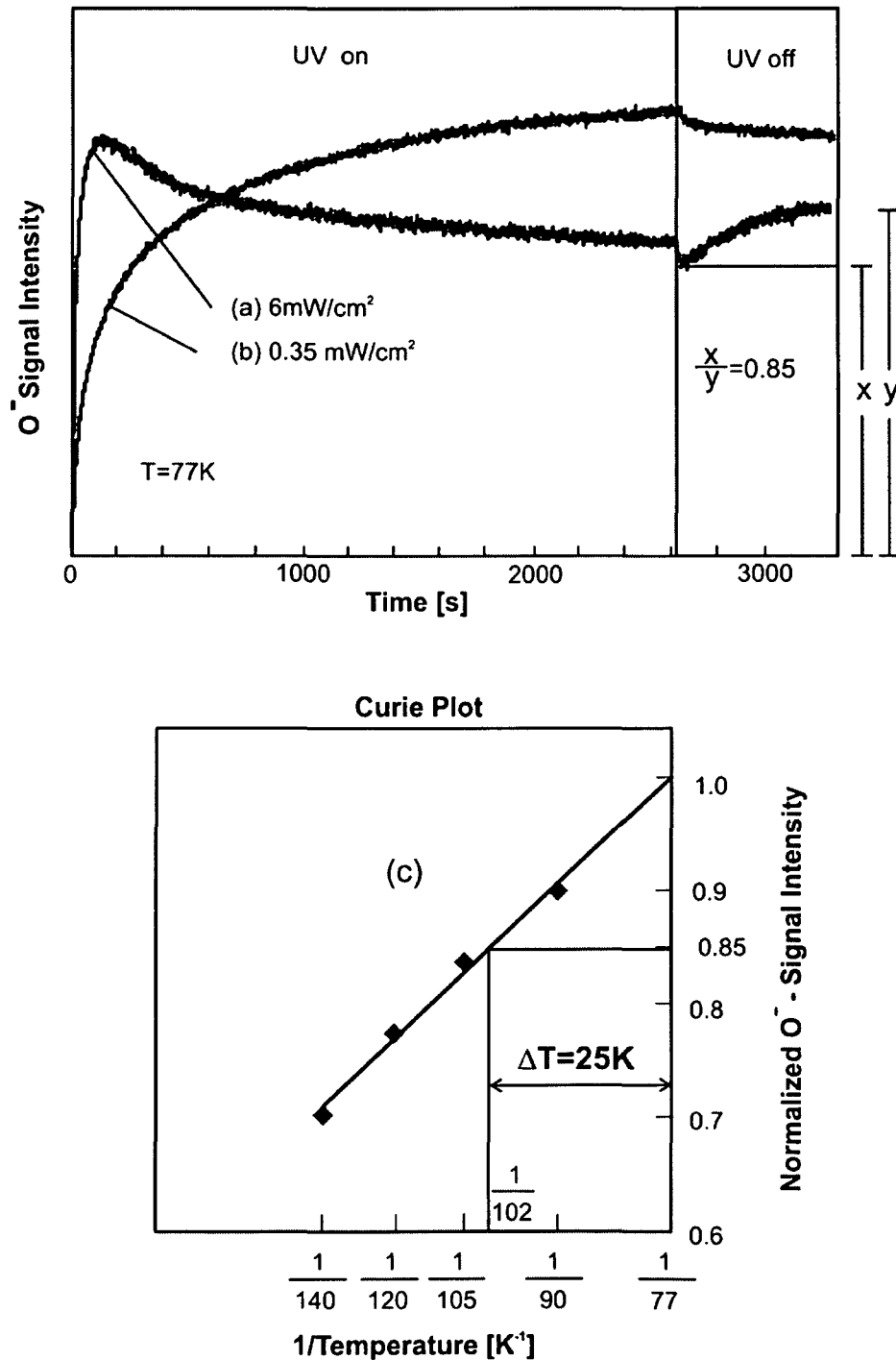


Fig. 5.4: UV light induced sample heating at high light irradiances: time evolution of trapped holes (O[•]) during UV exposure applying light irradiances of (a) 0.35 mW·cm⁻² and (b) 6 mW·cm⁻². (c) Curie plot: normalized signal intensity of trapped holes versus reciprocal sample temperature. The O[•] concentration was kept constant by scavenging the respective counter charge (electrons) by O₂.

In order to quantify the local heating effect on TiO₂ nanocrystals we measured the temperature dependence of the EPR signal intensity of a constant O⁻ centre concentration (Fig. 5.4c). The constant O⁻ concentration was accomplished by scavenging the corresponding electron centres with O₂ which inhibits efficiently electron/hole recombination¹¹³. The resulting O⁻ intensity shows a linear dependence on the reciprocal temperature (Curie plot). Now we subject the effect of UV light discontinuation to a thorough examination (Fig. 5.4): In the case of $I = 0.35 \text{ mW} \cdot \text{cm}^{-2}$ the O⁻ signal drops by about 5 % of its maximum value $[O^-]_{\text{max}}$, which was reached during UV exposure, and remains constant thereafter (Fig. 5.4b). For $I = 6 \text{ mW} \cdot \text{cm}^{-2}$ the initial intensity drop is followed by an additional signal increase (Fig. 5.4a). We attribute this signal increase to the enhancement of EPR sensitivity (Curie law) by decreasing the acquisition temperature (as achieved by turning of the UV light, which acts as a heating source). A temperature increase of $\Delta T = 25 \text{ K}$ by UV induced sample heating was determined by means of the Curie plot and using the respective intensity values before and after sample cooling $x/y = 0.85$ (Fig. 5.4a). This result shows that effective sample cooling marks a crucial point concerning the investigation of light induced phenomena. Meeting the requirement of a constant sample temperature gets ticklish when dealing with loose powders under high vacuum conditions. In order to fulfil this criterion one has to pay particular attention to the choice of appropriate values for the light irradiance.

UV induced sample heating may also have an important consequence concerning the effort of improving the quantum yield of photocatalytic reactions. Especially in the case of gaseous reactants, where heat transfer from the catalyst to the surrounding is less efficient than in liquid media, catalyst heating may influence the overall performance.

5.3. Conclusions

The reversible trapping of photogenerated hole centres and electrons was investigated on dehydroxylated TiO₂ nanoparticles as a function of light power by electron paramagnetic resonance spectroscopy (EPR) at pressures $p < 10^{-6}$ mbar. High light irradiances cause a UV induced heating of the sample due to the energy dissipation of absorbed UV into the lattice associated with heat release. Therefore, when studying light induced processes particular attention has to be turned to effective sample cooling and to the choice of appropriate values for the light irradiance.

6. Charge trapping and the photoadsorption of O₂ on TiO₂ nanocrystals

6.1. Introduction

TiO₂ powders have been extensively investigated over the last three decades due to their potential in technological applications ranging from photo-electrochemistry to photocatalysis^{9,115,116}. Photocatalytic oxidation reactions of organic pollutants were characterized in aqueous solutions^{10,69,117} and in the gas-phase¹¹⁸⁻¹²⁰. It was shown, that on the basis of TiO₂ nanostructures photocatalysts can exhibit higher activity and selectivity than commercially available microcrystalline samples^{15,121-125}. These observations were explained by several factors, among them, the high specific surface areas associated with small particle sizes and the enhanced adsorption of organic molecules¹²⁶. Consequently more surface sites can mediate interfacial charge transfer¹²⁵. However, a stochastic analysis of kinetic data for semiconductors of different sizes has shown a detrimental effect: the charge carrier recombination rate is enhanced when the particle size decreases from 20 nm to 3 nm¹²⁷. Furthermore, an optimal particle size around 11 nm was determined experimentally for the photocatalytic decomposition of chloroform in aqueous solution¹²⁸. In the last years, many investigations have focused on the influence of different particle properties like size^{122,125,129,130}, degree of hydroxylation^{91,129,131} and crystallographic phase^{78,91,132,133} on the catalytic performance. Nevertheless, little about the interconnection between the primary photoexcitation process in the particles' bulk and the resulting surface processes is known. These include surface charge trapping and of course the chemical consumption of charge carriers by interfacial charge transfer^{88,134,135}.

Investigating separation and the persistent trapping of photogenerated charges is relevant for the following reasons:

- a. By decreasing the recombination rate, charge trapping extends the lifetime of photogenerated electrons and holes¹³⁶. As such, the trapped charges can participate photochemically on a lengthened time scale, which in turn, enhances the efficiency of the photocatalyst.
- b. Hole trapping sites on the TiO₂ surface are generally accepted as active species in photocatalytic oxidation reactions¹³⁷. The structure of hole centres strongly depends upon surface treatment and modification⁸⁰ and the identification of hole trapping sites is, therefore, indispensable for the design of new photocatalyst materials.

- c. Trapping of photogenerated charges by molecular O₂ with an electron affinity of 0.43 eV is considered as a counter reaction in many photocatalytic oxidation processes. It determines the efficiency of the overall reaction¹³⁸. The reduction products O₂⁻ are effective oxygenation agents and open up another pathway for oxidative degradation of pollutants^{10,69}. Profound knowledge about the nature of photoadsorbed oxygen species is needed to elucidate photocatalytically relevant reaction mechanisms. Even in cases where O₂ does not directly participate in the degradation mechanism, measured rates and efficiencies are significantly enhanced when O₂ is used as a *sacrificial electron acceptor*¹³⁶. As a result, the inhibition of the electron-hole recombination by electron scavenging allows for the accumulation of chemically active hole centres.

Electron paramagnetic resonance (EPR) spectroscopy is an exceptionally useful technique for the investigation of charge separation processes on metal oxide materials^{53,63}. It allows not only to monitor localized electrons (Ti³⁺)¹¹¹ and holes (O⁻)^{91,98}, but also species adsorbed after charge transfer to gas-phase molecules^{96,139} e.g. superoxy species O₂⁻^{94,104,140} are accessible to this technique. Photoinduced O₂ adsorption has been investigated extensively on dehydroxylated TiO₂ powders in the seventies¹⁴⁰⁻¹⁴⁴. However, to the best of our knowledge, this process has never been studied quantitatively by addressing the role of particle size and the number of trapped charges.

The aim of the present study is to quantitatively investigate charge trapping processes and specifically charge transfer to molecular oxygen on dehydroxylated titania nanocrystals. For this benchmark study, anatase TiO₂ nanoparticles were obtained by metal organic chemical vapour deposition (MOCVD). The chemical vapour deposition (CVD) method, as a non solution-based synthesis technique, is appropriate for the production of different metal oxides on the nanometer range that can be efficiently dehydroxylated by thermal treatment without extensive particle coarsening and coalescence^{60,145}. In a foregoing study we have shown that electron and hole trapping can be tracked on a time scale of seconds to minutes when UV light powers in the mW·cm⁻² range are used^{112,113}. This has been achieved at temperatures T < 140 K and at high vacuum (P < 10⁻⁶ mbar) which certainly does not correspond to photocatalytically relevant conditions. However, only if the surface is kept free of adsorbates (P < 10⁻⁶ mbar), observations from photoexcitation experiments can be discussed entirely in the light of bulk and surface structure. Later on, this study will serve as a base for addressing the role of adsorbate and particle morphology in the photochemical surface process.

The study is structured as follows: first, a characterization of paramagnetic oxygen species that were isolated on dehydroxylated CVD TiO₂ particles will be given. The evolution of the observed centres will be studied as a function of time and O₂ pressure. On this basis the absolute number of separated electron/hole pairs per nanoparticle will be quantified by EPR spectroscopy in conjunction with the volumetric determination of photoadsorbed O₂.

6.2. Results

6.2.1. Photoinduced charge separation at different temperatures

EPR spectra after UV excitation ($I = 0.7 \text{ mW}\cdot\text{cm}^{-2}$ with $h\nu > 3.2 \text{ eV}$) at 90 K, 140 K and 298 K are shown in Figs. 6.1a, 6.1b and 6.1c, respectively. Signals due to two (Fig. 6.1a) or one (Fig. 6.1b) paramagnetic states were observed only after activation below room temperature (for g -values see Tab. 6.1)*. The low field signal in Fig. 6.1a is assigned to trapped holes h^+

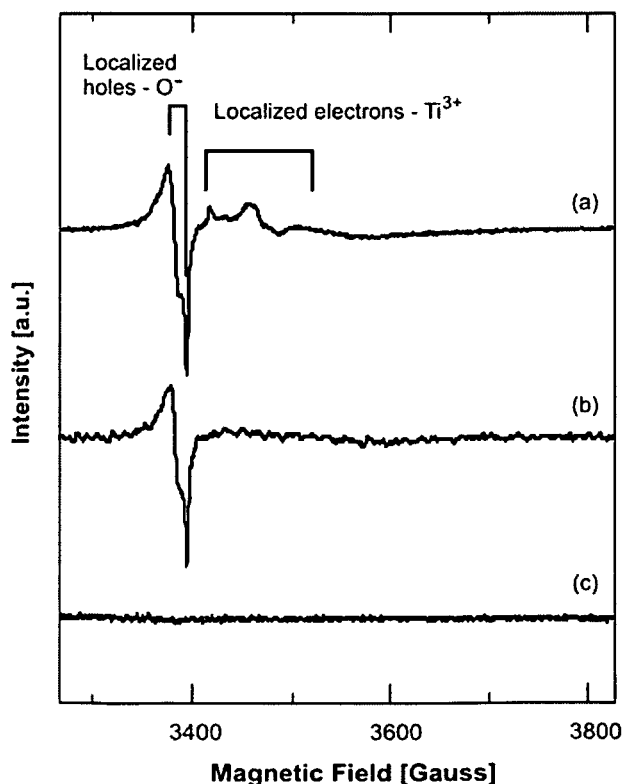


Fig 6.1: Paramagnetic species on TiO₂ nanocrystals after 20 minutes of UV exposure at (a) 90 K, (b) 140 K and (c) 298 K. All EPR spectra were acquired at 90 K.

* The ratio of O^{•-} and Ti³⁺ concentrations is not represented properly in these spectra. A high microwave power (100 mW) had to be used in order to make visible the Ti³⁺ centres. At these MW powers the O^{•-} species already shows considerable saturation behaviour and is therefore underestimated by a factor of ~12.

localized at oxygen ions, O⁻ ^{95,112}. The second feature at higher magnetic field which is composed of axially symmetric signals due to trapped electrons at two so far unspecified paramagnetic Ti³⁺ centres (Ti³⁺[I] and Ti³⁺[II]) on anatase TiO₂ ^{79,80,114} is exclusively observed under UV excitation at 90 K. Hole centres in form of O⁻ radicals were obtained after UV excitation at 90 K and 140 K, but not observed after activation at room temperature. The discrepancy in yield between the O⁻ and the Ti³⁺ centre concentration (Fig. 6.1b) reveals that photoexcited electrons do not exclusively form Ti³⁺ when they become trapped. This phenomenon has been confirmed by a previous study using infrared spectroscopy, where it was shown that under the same experimental conditions applied, the majority of photoexcited electrons enter the conduction band where they remain for a timescale on the order of hours ¹¹². On this basis and in accordance with literature we specify the following charge transfer steps:



The total number of trapped holes is by a factor of 1.15 higher after UV-induced activation at T = 90 K (Fig. 6.1a) as compared to T = 140 K (Fig. 6.1b). No persistent charge separation was observed after UV excitation at 298 K (Fig. 6.1c).

trapped holes - O ⁻ (Figs. 6.2, 6.3, 6.5)	$g_{\perp} = 2.0121$	$g_{\parallel} = 2.0046$	
trapped electrons - Ti ³⁺ (Fig. 6.2a)			
Ti ³⁺ [I]	$g_{\perp} = 1.9640$	$g_{\parallel} = 1.9495$	
Ti ³⁺ [II]	$g_{\perp} = 1.9900$	$g_{\parallel} = 1.9600$	
background (Fig. 6.2a)	$g_{\text{iso}} = 1.9300$		
ozonide - O ₃ ⁻ (Figs. 6.3, 6.4, 6.5)			
O ₃ ⁻ [I]	$g_{\perp} = 2.0015$	$g_{\parallel} = 2.0073$	
O ₃ ⁻ [II]	$g_{\perp} = 1.9996$	$g_{\parallel} = 2.0073$	
scavenged electrons - O ₂ ⁻ (Figs. 6.3, 6.4, 6.5)			
O ₂ ⁻ [I]	$g_{zz} = 2.0248$	$g_{yy} = 2.0096$	$g_{xx} = 2.0033$
O ₂ ⁻ [II]	$g_{zz} = 2.0184$	$g_{yy} = 2.0096$	$g_{xx} = 2.0033$

Tab. 6.1: Table with g-factors of paramagnetic centres observed on TiO₂ nanocrystals as a result of charge trapping.

6.2.2. Charge transfer to molecular oxygen

Molecular oxygen was added to the TiO₂ nanocrystals after UV excitation in order to study the reactivity of separated charge carriers at 90 K. Fig. 6.2 depicts the magnified region of the O⁻ signal prior to O₂ addition, which was originally presented in Fig. 6.1a. Trapped electron centres (Ti³⁺) present after UV exposure at 90 K are out of the magnetic field range in Fig. 6.2a. Addition of O₂ leads to their complete disappearance and fundamental changes in the magnetic field range where oxygen centred radicals resonate were observed^{94,98,104} (Fig. 6.2b). By means of spectrum simulation (Fig. 6.3) the total spectrum was deconvoluted into single component spectra which are associated with the following types of oxygen radicals: A) superoxy species O₂⁻^{91,99,112} (Fig. 6.3b) B) ozonide species O₃⁻⁹⁹ (Fig. 6.3c and d, g-values see Tab. 6.1) and C) a small fraction of remaining O⁻ centres (not shown). The concentration of spin centres was determined by double integration of the respective single component spectra and revealed a 1:1 ratio between hole centres (O₃⁻ [I+II], O⁻) and electron centres (O₂⁻). Identical species with the same relative concentrations were measured after excitation had been performed at 140 K¹¹². This points to the fact that at 90 K both, conduction band electrons (UV exposure at 140 K; Fig. 6.1b) and localized electrons from Ti³⁺ sites (UV exposure at 90 K; Fig. 6.1a) transfer readily to molecular O₂ from the gas-phase, according to the equations below:

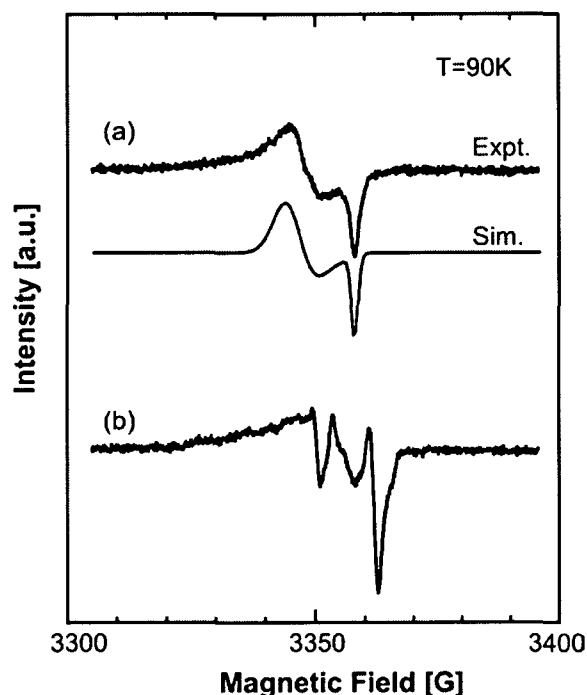
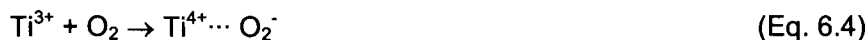


Fig. 6.2: Effect of O₂ addition to the EPR properties of trapped charges on TiO₂ nanocrystals. The EPR spectra were acquired (a) after 20 minutes of UV exposure at 90 K and P < 10⁻⁶ mbar and (b) after subsequent addition of O₂ at the same temperature followed by evacuation down to P < 10⁻⁶ mbar. The presented magnetic field range corresponds to the low field region of Fig. 6.1.

On the other hand, hole centres react with O₂ to form ozonide-type tri-nuclear oxygen adducts¹⁰⁴:



The thermal stabilities of the adsorbed oxygen species, O₃^{·-} and O₂^{·-}, were investigated in the temperature range between 90 K and 140 K and at P < 10⁻⁶ mbar. The signal envelope changes significantly with temperature and the relative concentrations of superoxy species O₂^{·-} (Fig. 6.3b), ozonide ions O₃^{·-} (Figs. 6.3c and 6.3d), and O^{·-} were determined via spectrum simulation (Fig. 6.4). With increasing temperature, the O^{·-} concentration increase clearly correlates with the O₃^{·-} decrease and at 140 K the ozonide signal has completely disappeared upon restoration of the original O^{·-} signal intensity. Double integration of the simulated O^{·-} and O₂^{·-} spectra at 140 K reveals for O^{·-} and O₂^{·-} species an intensity ratio of ~ 1.1 : 1 and thus, an equal concentration of holes trapped by surface O²⁻ anions to produce O^{·-} (Eq. 6.3), and electrons scavenged by molecular oxygen (Eqs. 6.4 and 6.5). The resulting O₂^{·-} are stable at room temperature and thus efficiently maintain the state of charge separation at this temperature. At T = 140 K gas-phase oxygen causes the total extinction of all related EPR signals and indicates that all trapped holes are located in the surface of the nanocrystals*.

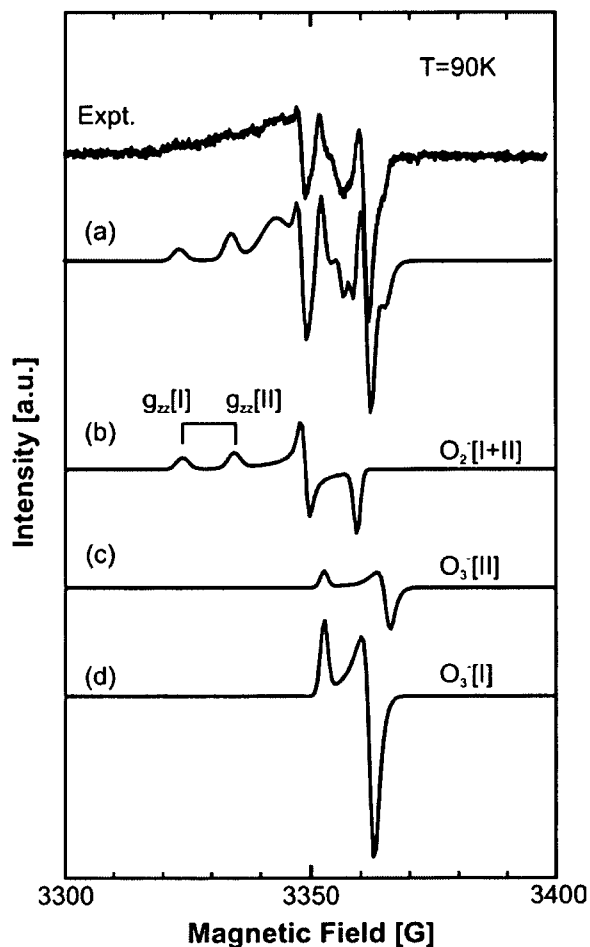


Fig. 6.3: Experimental and simulated EPR signals of oxygen radicals observed on TiO₂ nanocrystals. (a) Comparison between experimental spectrum (Fig. 6.2b) with the best fit simulation. Figures (b)-(d) correspond to the simulated single component spectra of O₂^{·-} ions, O₃^{·-} (I) ions and O₃^{·-} (II) ions, respectively.

* As a well-known fact, paramagnetic surface states become EPR invisible when oxygen is present in the gas-phase. Due to its paramagnetic nature, exchange effects with other spin centres cause signal broadening and the disappearance of the signal at higher pressures.

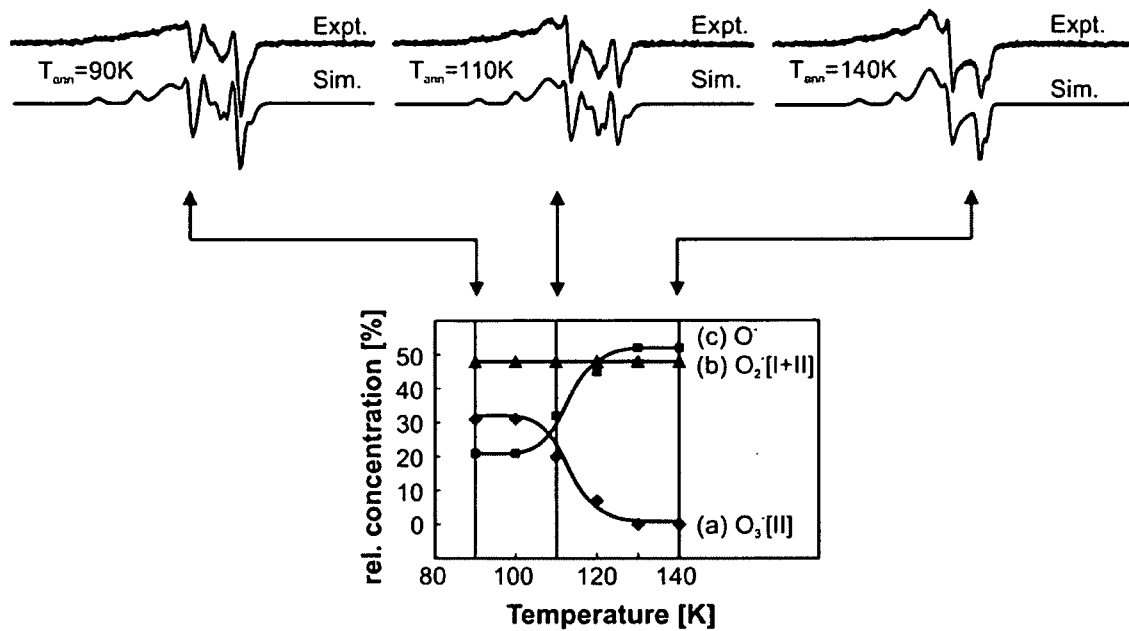


Fig. 6.4: Thermal stability of oxygen radicals on the surface of TiO₂ nanocrystals. The concentration of (a) ozonide ions O₃⁻, (b) superoxide anions O₂⁻ and (c) O⁻ ions are plotted as a function of temperature. Representative experimental and simulated EPR spectra at each marked area on the graph are presented in the top line.

6.2.3. Charge separation in the presence of an electron scavenger (O₂)

If O₂ is added to pre-irradiated TiO₂ nanocrystals at T = 140 K, O₂⁻ are produced and the O⁻ concentration remains unchanged since no O₃⁻ are formed at this temperature (Fig. 6.4, spectrum on the right hand). The ratio of O⁻ to O₂⁻ again accounts for unity. Qualitatively, the same is true for UV exposure in the presence of O₂ in the gas-phase at T = 140 K. However, the total concentration of paramagnetic centres is enhanced by a factor of 10.

Kinetic data for the accumulation of scavenged electrons (Fig. 6.5a) and trapped hole centres (Fig. 6.5b) during UV exposure time in the presence of 0.1 mbar O₂ at T = 140 K are given in Fig. 6.5. The following consecutive experimental steps were applied iteratively for these curves:

1. UV exposure in the presence of O₂
2. Removal of residual O₂ by evacuation down to 10⁻⁶ mbar
3. Acquisition of the EPR spectrum, spectrum simulation and double integration of the respective single component spectra.

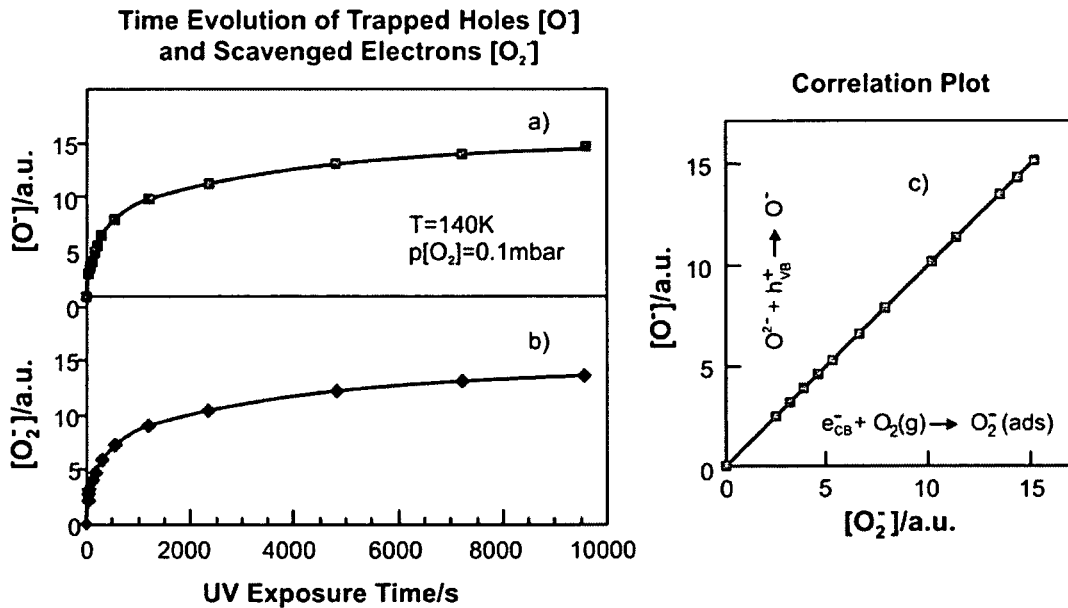


Fig. 6.5: Time-resolved accumulation of (a) trapped hole centres $O\cdot$ and (b) scavenged electrons $O_2\cdot^-$ as a function of UV exposure time at 0.1 mbar O_2 . A correlation between $O\cdot$ and $O_2\cdot^-$ EPR signal intensities is shown in Figure 6.5c.

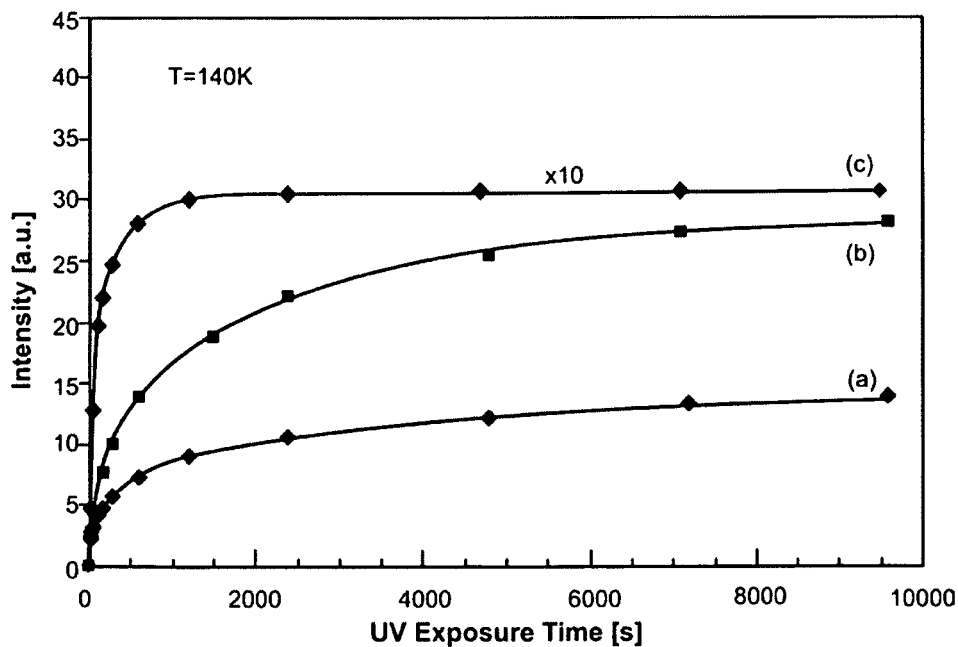


Fig. 6.6: Time-resolved accumulation of trapped holes and scavenged electrons upon UV exposure at different oxygen pressures: (a) 0.1 mbar O_2 and (b) 10 mbar O_2 . (c) UV exposure at $P < 10^{-6}$ mbar and subsequent addition of O_2 . Note that the profiles of $O\cdot$ and $O_2\cdot^-$ coincide for a given pressure, as the ratio of $O\cdot$ to $O_2\cdot^-$ accounts for unity throughout all experiments.

A linear correlation between the concentration of adsorbed $O_2\cdot^-$ and $O\cdot$ ions over an integral UV exposure time of 2.5 h is substantiated by the plot in Fig. 6.5c. The time-dependent $O_2\cdot^-$ and $O\cdot$ concentration profiles obtained at varied oxygen pressures (Figs. 6.6a and 6.6b) differ

only in the final concentration level of paramagnetic states. The higher the oxygen pressure during UV exposure, the higher is the maximum concentration of O⁻ and O₂⁻. When UV excitation was performed at $P < 10^{-6}$ mbar and O₂ was added afterwards (Eqs. 6.1 - 6.5), lower concentrations of O₂⁻ and O⁻ species were observed and the kinetics were found to be different (Fig. 6.6c): the maximum concentration was reached at 1000 s, significantly earlier than in the O₂ experiments. The maximum concentration of scavenged electrons O₂⁻ (which equals the maximum number of trapped hole centres O⁻) is plotted as a function of the O₂ pressure in Fig. 6.7. No further increase in the maximum number of trapped charges can be observed above O₂ pressures of 25 mbar O₂.

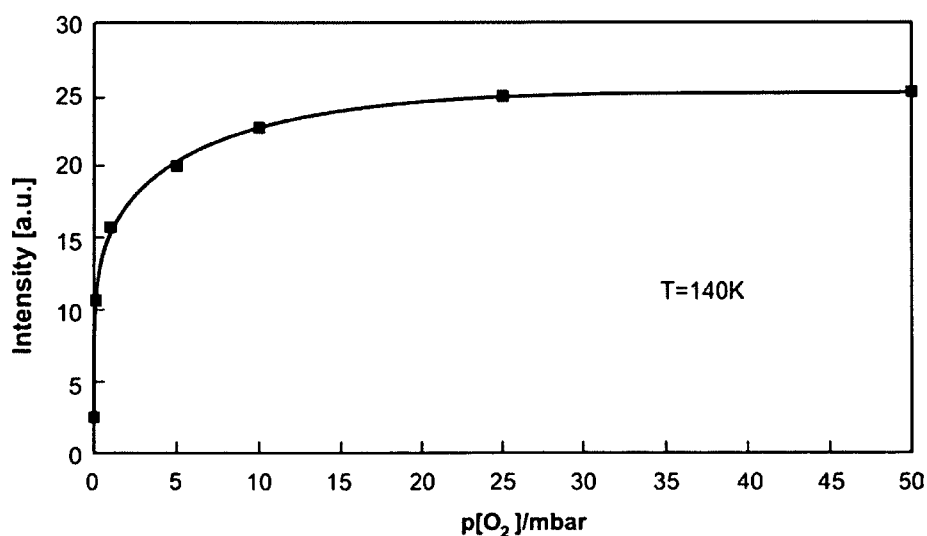


Fig. 6.7: Maximum concentration of scavenged electrons (O₂⁻) as a result of UV exposure at different oxygen pressures. The first data point (UV exposure in vacuo) was determined after O₂ addition to the pre-irradiated sample and subsequent evacuation. The solid line is added as a guide to the eye.

6.2.4. Volumetric measurement of photoadsorbed oxygen

In order to quantify the absolute number of separated charges, photogenerated electrons were titrated on the basis of the electron transfer reaction from the nanocrystal to molecular oxygen (Eqs. 6.4 and 6.5). The change of the O₂ pressure within the known volume of the EPR sample cell (Fig. 6.8, left ordinate scale) during photoadsorption was related to the measured O₂⁻ EPR signal intensities (Fig. 6.8, right ordinate scale). The photoadsorption experiments were performed at higher light irradiance (100 mW·cm⁻²) and temperature (298 K). The performance of these experiments at room temperature is done for two reasons:

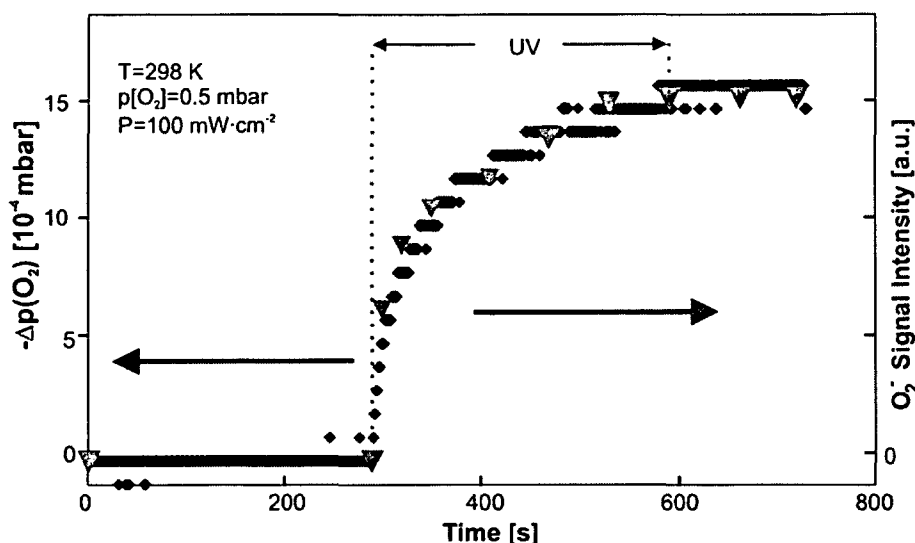
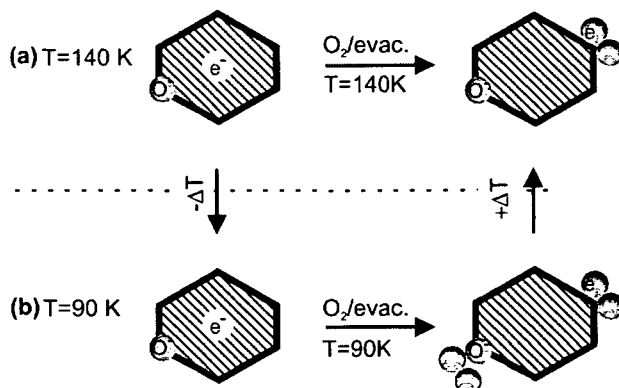


Fig. 6.8: Photoadsorption of O₂ on TiO₂ nanocrystals: Correlation of pressure change in the EPR cell and O₂⁻ EPR signal intensity as a function of UV exposure time at 298 K and 0.5 mbar O₂. The EPR data were determined by means of the same procedure as described for the experiment in Fig. 6.5.

First, condensation effects of molecular oxygen are excluded and second, isothermal conditions for the whole system comprising powder sample and the defined volume of the gas cell, is guaranteed. The EPR measurements, however, were again performed at 140 K. Pressure measurements were performed using a MKS Baratron 390HA-00100 pressure gauge in the range between 10⁻⁴ Torr to 1 Torr with an accuracy of 0.08%. The volume of the cell plus the whole system (46.8 cm³) was determined using the ideal gas equation with reference to a known volume. An O₂ pressure of 0.5000 mbar was applied and a pressure decrease $\Delta p = 0.0016$ mbar was observed after 300 s of UV exposure. The amount of adsorbed oxygen was then determined using the ideal gas equation. Again, a 1:1 ratio of O⁻ to O₂⁻ species was obtained and a direct correlation between pressure decrease and an O₂⁻ signal intensity increase was measured (Fig. 6.8). The number of illuminated particles was estimated considering spherical particles with a diameter of 13 nm*. In order to quantify the concentration of trapped charges per particle, the number of adsorbed O₂ molecules was rationed to the number of particles (Tab. 6.2). A maximum concentration of 10 O⁻/O₂⁻ pairs per particle was obtained after O₂ photoadsorption at 140 K. UV excitation at high vacuum conditions at the same temperature results in only one e⁻/O⁻ pair per particle. The observations of section 6.2.1 to 6.2.4 are recapitulated by means of Fig. 6.9, which illustrates the electron transfer reactions including the absolute numbers of effectively separated charges per particle.

* Approximate estimates for the number of trapped charges per particles may be made using the following argument: 12.5 mg of sample powder was used for these experiments and correspond to 3·10¹⁵ particles assuming a spherical particle shape with an average diameter of 13 nm. By control experiments such as sample rotation during UV exposure and shaking of the powder sample it was made sure that all nanocrystals contained in the EPR tube were efficiently exposed to UV light.

1. UV exposure at $p < 10^{-6}$ mbar
+ subsequent addition of O₂
at different temperatures



2. UV exposure in the presence
of O₂

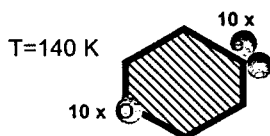


Fig. 6.9: Schematic of the interaction between trapped charges on TiO₂ nanocrystals with molecular O₂. 1) When charge separation on TiO₂ nanocrystals was performed at $P < 10^{-6}$ mbar and $T = 140$ K, trapped electrons transfer readily to subsequently added gas-phase oxygen and produce adsorbed O₂⁻ ions (1a). When the same experiment is performed at 90 K (1b) an ozonide-type adduct between surface trapped hole centres and O₂, which is unstable at 140 K, is produced in addition to the O₂⁻ species. Step 2 illustrates the result of the UV excitation experiment carried out at 140 K and in the presence of O₂ where the number of trapped charges is enhanced by a factor of 10.

		P(O ₂)	
		10 ⁻⁶ mbar	50 mbar
T _{UV}	298 K	0	3 ± 0.5
	140 K	1 ± 0.5	10 ± 0.5

Tab. 6.2: Number of persistently trapped electron and hole centres per TiO₂ nanocrystal as a result of UV activation at temperatures T_{UV} and O₂ pressures P(O₂).

6.3. Discussion

6.3.1. Temperature-induced recombination

In the absence of electron and hole scavengers, the efficiency of charge separation depends critically on the sample temperature (Fig. 6.1). When UV excitation is applied at $T = 90$ K the total number of trapped holes is by a factor of 1.15 larger, as compared to the same experiment at $T = 140$ K. No Ti³⁺ states can be generated at the somewhat elevated temperature ($T = 140$ K).

The nature of the underlying defects which transform into Ti³⁺ states under UV exposure are not identified yet. As reported in a previous paper¹¹², these reduced states can be bleached with photons of energy below 1.6 eV which indicates that the associated electronic levels are located below the conduction band minimum. Similar observations were made in an earlier study by Servicka et al.⁹³. Ghosh et al.¹⁰⁶ observed the presence of eight specific levels in rutile single crystals less than 1 eV below the conduction band. They speculated that these levels are connected to Ti³⁺ ions at regular and interstitial sites. Coronado et al.¹²⁹ suggested that Ti⁴⁺ cations in close vicinity to hydroxyl groups are likely candidates for the stabilization of Ti³⁺ centres. More work has to be done for an unambiguous identification of such sites in polycrystals.

The absence of Ti³⁺ states after excitation at 140 K can only be understood in terms of a thermally induced recombination of localized electrons Ti³⁺ with trapped hole centres. Energies for detrapping and recombination are in the range of meV. This connects to observations on slightly reduced rutile single crystals where electronic conduction above 4 K was related to the ionisation of donor centres, i.e. Ti³⁺ states¹⁴⁶. On the basis of a detailed EPR analysis and channelling results the donor centres were identified as interstitial Ti³⁺ ions in the rutile single crystals and experimentally observed ionisation energies amount a few meV.

For the present experiments it is important to note that obviously only a fraction of particles carries defects which at 77 K can efficiently bind electrons and transform into Ti³⁺ under UV exposure. This fraction varies between 0 and 10% of the total number of TiO₂ particles and depends on material properties and sample activation procedure.

Once such a defect traps an electron from the conduction band a second electron can be persistently trapped in the conduction band. Detrapping by temperature rise to e.g. 140 K

leads to depopulation of this localized state upon return of the electron into the valence band. If one expects that the second electron from the conduction band also drains off via the defect state into the valence band, the reduction in the number of trapped charges would be 16 % less than in the experiment at lower temperature where Ti³⁺ centres are stable. This estimate is consistent with the experimentally observed depletion of trapped charges by about -15 % at 140 K compared to 90 K.

UV excitation at 298 K does not yield any trapped charges (Fig. 6.1c), indicating that in the absence of electron and/or hole scavengers, energies around $k_B T$ (26 meV at room temperature, Fig. 6.10) are sufficient for the total annihilation of all UV generated electron/hole pairs.

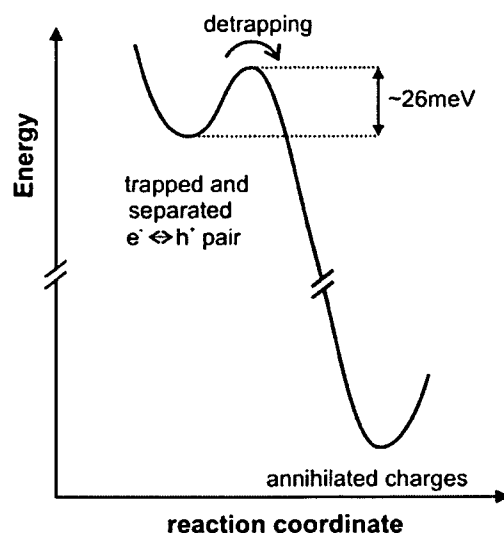


Fig. 6.10: Energy diagram showing the states of trapped and separated electron and hole centres in TiO₂ nanocrystals. Energies in the range of tens of meV are sufficient for crossing the barrier to charge carrier recombination. This annihilation process corresponds to the return of photogenerated electrons into the valence band.

6.3.2. The effect of O₂ on the efficiency of charge separation

The observation of single electron charging (Tab. 6.2) connects well to observations on nanocrystalline anatase films, which were used as electrodes for dye-sensitised solar cells in organic solvents¹⁴⁷⁻¹⁴⁹. It was found using intensity-modulated photocurrent spectroscopy that the average concentration of conduction band electrons corresponds to one electron per nanoparticle¹⁴⁷. It was also shown by means of transient absorption spectroscopy that at high light irradiances, when nanoparticles are charged with more than one electron, recombination losses become significant¹⁴⁹. This has been attributed to the Coulombic repulsion between photogenerated charges within the nanoparticle. Since the charge carriers are no longer solvated in an effectively infinite medium repulsive charging energies in the range of tens of meV¹⁴⁹ are needed to add an additional electron to an already negatively charged system. If one neglects the positive charge of trapped hole centres as effectively screened species, the addition of a second conduction band electron per particle is expected to raise the energy of this electron to a level wherefrom detrapping similar to the thermally-induced recombination pathway (Fig. 6.10) can occur. Consequently, under UV excitation

and at $P < 10^{-6}$ mbar the maximum concentration of effectively separated charges is limited by Coulomb repulsion between conduction band electrons (trapping of electrons at Ti³⁺ sites does not occur at $T = 140$ K). Under continuous UV exposure, light induced charge separation and recombination are equilibrated:



The crucial point is the capacity of a nanocrystal to effectively separate and screen two opposite charges in space. If gas-phase oxygen is present, electrons are removed from the dynamic equilibrium in Eq. 6.7 and become screened from the other electrons due to their localization at adsorbate species (Fig. 6.9). Therefore, we propose that the saturation concentration of trapped charges becomes limited either by a) the number of adsorption sites for O₂⁻ ions on the nanocrystal surface or b) the surface capacity for hole trapping and O⁻ formation. In the presence of O₂, the maximum concentration of separated charges (Fig. 6.7) is determined by the equilibrium of UV induced adsorption and UV induced desorption (i.e. the back electron transfer from O₂⁻ to a surface-trapped hole) of molecular oxygen as illustrated by Fig. 6.11. The UV induced desorption of surface bound molecular oxygen becomes less effective at increasing pressures up to 25 mbar O₂. Further pressure increase does not affect the final state (Fig. 6.7).

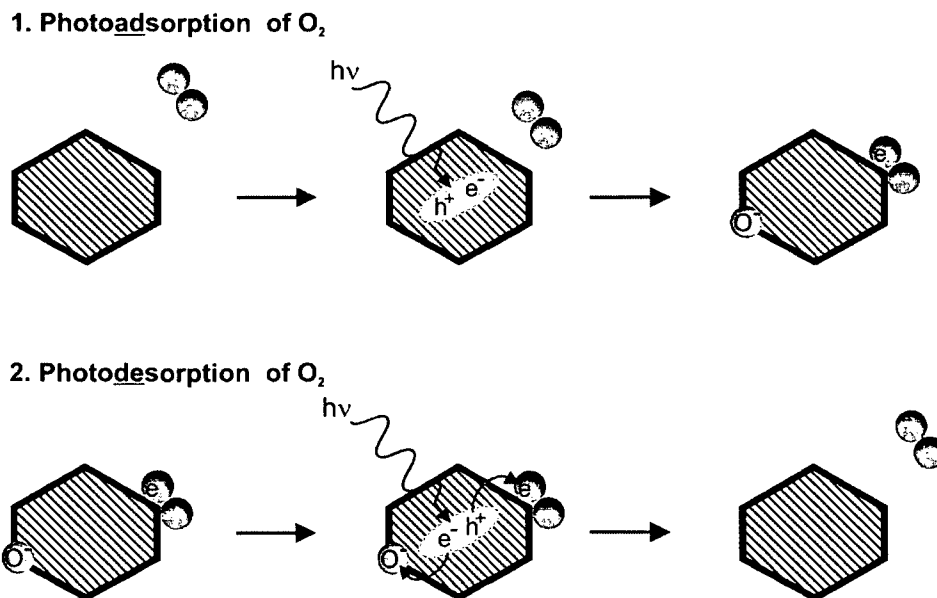


Fig. 6.11: Cartoon, which illustrates the processes of UV induced O₂ adsorption as well as the desorption of O₂, which occurs via the electronic neutralization of O₂⁻ ions with photo-generated hole centres. These processes constitute an equilibrium, which is reversible with respect to O₂ pressure.

Electron-hole recombination is the major limitation for achievement of high quantum yields for photocatalytic reactions. In this context, charge trapping is a desired effect, because it extends the lifetime of electrons and holes and thus decreases the recombination rate. An undesired side-effect, however, is the loss of reducing power as the photogenerated carriers lose a significant amount of energy in the trapping process⁸⁰. It has been shown, that recombination can be inhibited efficiently by scavenging at least one of the respective charge carriers with an appropriate electron or hole scavenger, thus accumulating the counter charge within the semiconductor particle¹⁵⁰⁻¹⁵². The absolute number of effectively separated charges for both UV exposure at high vacuum conditions as well as UV activation in the presence of an electron acceptor is, therefore, an important quantity regarding the characterization of the photocatalyst particle. These numbers can be regarded as a "figure of merit" for a certain catalyst, as they connect directly to (a) the efficiency of the separation of photogenerated charges and (b) the capacity of the respective surface planes to photoadsorb molecules from the gas-phase. The results of spectroscopic investigations can thus provide profound insights in the size and shape dependence of nanocrystals with respect to charge trapping and charge transfer reactions. For this purpose, samples of different size (surface-to-bulk ratio) and well-defined morphology (different surface planes) have to be investigated. Furthermore, the influence of surface OH-groups has to be studied on samples with different levels of hydroxylation. These investigations will provide insights into processes occurring under photocatalytically relevant conditions and will directly connect to studies performed on colloids by others⁸⁰. Such experiments are currently under investigation in our laboratory. In addition to this, MOCVD offers a promising sample preparation approach since nanocrystals of different size can be obtained by variation of the CVD parameters^{51,153}.

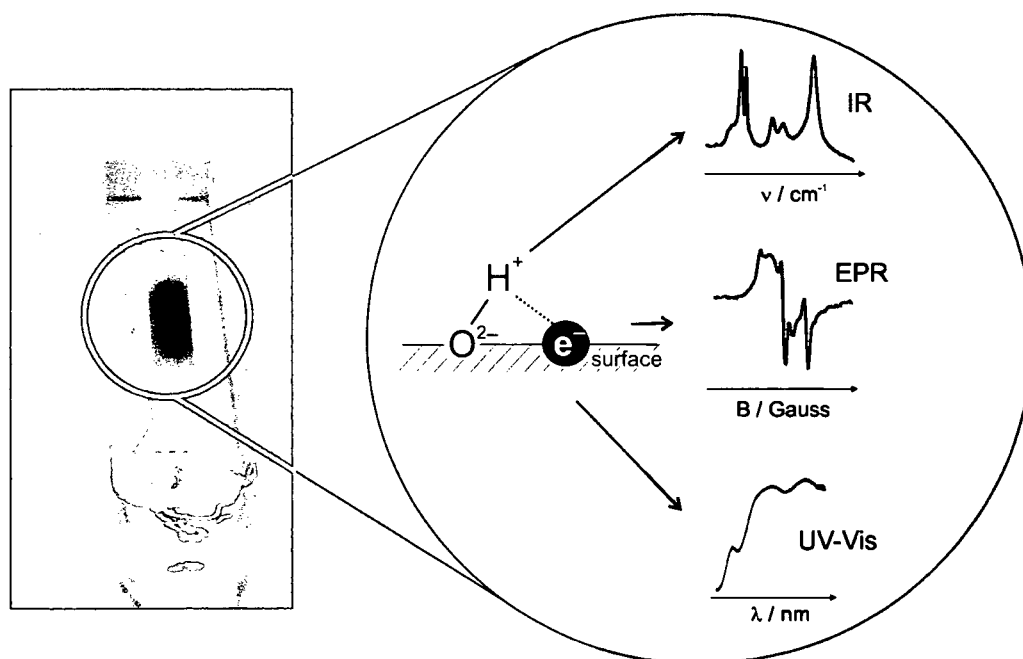
6.4. Conclusions

On dehydroxylated TiO₂ nanoparticles (average diameter of 13 nm), trapping processes of photogenerated charges and charge transfer reactions have been investigated in the temperature range between 90 K and 298 K. The studies were carried out at high vacuum conditions ($P < 10^{-6}$ mbar) or in the presence of O₂ as an electron acceptor. In the latter case, photogenerated electrons are scavenged by adsorbed molecular oxygen forming superoxy species O₂⁻. The holes are either trapped by surface O²⁻, forming O⁻ species (140 K) or react with molecular oxygen (90 K) to produce ozonide species O₃⁻. The ozonide centres exhibit a very low thermal stability and decompose at T = 120 K into O⁻ species and molecular O₂. The quantification of the paramagnetic centres reveals a 1:1 ratio in the concentration between

hole (O_3^- , O^-) and electron centres (O_2^-). It was found, that UV exposure at $P < 10^{-6}$ mbar gives rise to one electron/hole pair per nanoparticle. This number is enhanced by a factor of 10 in the presence of an electron scavenger (O_2), which is explained by the more efficient screening of photogenerated electrons.

SURFACE CHEMISTRY ON MgO NANOCUBES

Utilizing the rather complex chemistry of hydrogen on the surface of MgO, various types of colour centres were selectively generated on MgO nanocubes. Different experimental procedures were applied that include the reduction of hydrogen either in conjunction with UV light or in the dark. The trapped electron centres were investigated by different spectroscopic techniques in order to probe the surface of the MgO nanocubes and to elucidate the chemical and physical properties of various surface arrays. The optical properties of colour centres were studied by UV/Vis diffuse reflectance spectroscopy (Sec. 7). In order to investigate the magnetic properties of the respective centres electron paramagnetic resonance (EPR) spectroscopy was used and the interaction of the electron with a nearby hydroxyl group was traced both by EPR spectroscopy and by infrared (IR) spectroscopy (Sec. 8). O^- hole centres at 3-coordinated corner oxygen sites were generated site-specifically and transformed into hydroxyl groups by homolytical H_2 splitting. In conjunction with *ab initio* embedded cluster calculations an assignment of these well-defined centres to specific surface arrays was proposed (Sec. 9).



7. Optical properties of surface trapped electrons

7.1. Introduction

The physical and chemical properties of insulator interfaces are crucial for a variety of fields spanning the range from microelectronics¹⁵⁴⁻¹⁵⁶ to heterogeneous catalysis^{1,157,158}. Since equilibrium surfaces are considered as chemically inert, the abundance of defects, either point defects, such as ion vacancies and coordinatively unsaturated ions, or extended defects, such as terrace steps, determine the chemical properties of the surface. For this reason a tremendous amount of research has focused on their characterization¹⁵⁹⁻¹⁶¹.

Magnesium oxide belongs to the most intensively studied materials because of its purely ionic nature and its simple cubic rock salt structure. Prominent defective surface sites that may act as electron traps are surface arrays of Mg^{2+} cations with a local deficiency in O^{2-} ions³⁹. These entities can be formally subsumed as $(\text{Mg}^{2+})_n$ units ($n = 1 - 5$) and incorporate single Mg^{2+} cations, classical anion vacancies, as well as less regular surface defects. In literature these centres are often referred to as surface colour centres or F_S centres^{162,163}.

In chemistry F_S centres on MgO have attracted attention, because they exhibit reactivity¹⁶⁴ and are involved in the electronic activation of metal clusters¹⁶⁵, when MgO is used as a substrate material. In addition, highly inert molecules, such as molecular nitrogen turned out to be activated by these sites at liquid nitrogen temperature¹⁶⁶. Furthermore the role of electron traps is of considerable importance in photochemistry, because they are intimately related to the fate of photogenerated excitons and their decomposition products, i.e. electrons and electron holes⁶³.

The abundance of F_S centres on single crystalline epitaxially grown MgO films, considered as model surfaces, is very limited. It has to be artificially increased by high temperature treatment above 1100 K¹⁶⁷ or electron stimulated desorption¹⁶⁸, in order to be successfully studied by electron energy loss spectroscopy. Another approach for their investigation, though related to a much higher complexity, is the use of high surface area powder material, which contains a large number of different defect types. As shown recently, MgO nanoparticles, which were produced by chemical vapour deposition, exhibit surfaces with a surprisingly uniform distribution of spectroscopically very well defined defects having specific chemical reactivities¹⁴⁵.

As for epitaxially grown MgO films, electron trapping sites on polycrystalline MgO have to be transformed into paramagnetic (i.e. F_S^+ , $1e^-$) and diamagnetic (i.e. F_S^0 , $2e^-$) centres to study them by electron paramagnetic resonance spectroscopy (EPR)¹⁶² and/or by optical spectroscopy in the UV/Vis range³⁶ respectively. This transformation corresponds to an electronic reduction of the surface and can be achieved by chemical means, such as the ionisation of deposited alkali metal atoms¹⁶⁹ or the simultaneous exposure towards molecular hydrogen and UV light¹⁶². The latter technique involves the dissociation and UV assisted oxidation of hydrogen at essentially three different sets of reactive surface sites¹⁷⁰.

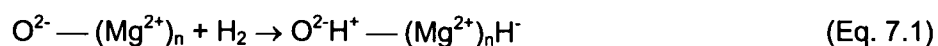
The purpose of the present UV/Vis reflectance study is to investigate the influence of H_2 pressure during surface colour centre formation in order to elucidate the effect of the underlying chemistry and photochemistry on the optical properties of the polycrystalline MgO surface. It will be shown that due to their electronic transitions in the energy range between 1.5 and 4 eV essentially three types of F_S centres can be observed. Their relative abundance clearly depends on the chemical nature of hydrogen species (i.e., chemisorbed hydride groups and atomic hydrogen) that serve as electron donors in the process of surface colour centre formation.

7.2. Experimental procedure

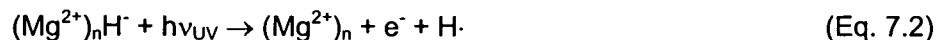
F_S centres were formed on MgO nanoparticles by sample exposure to molecular hydrogen and UV light. Three fundamentally different experimental procedures were chosen in order to initiate specific reaction channels for the electronic reduction of the surface. Before presenting the UV/Vis diffuse reflectance spectra, they will be briefly outlined below.

Procedure a: The MgO sample is contacted with hydrogen and subsequently evacuated. After removal of any reversible H_2 chemisorption product UV activation is applied. Based on previous IR and EPR spectroscopic studies performed in our laboratory¹⁷⁰ this treatment implies the occurrence of the surface reaction step represented by Eqs. 7.1 - 7.4.

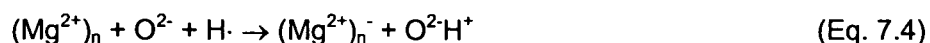
In the first step (Eq. 7.1) H_2 is split heterolytically and – at room temperature – irreversibly. It is transformed into mainly one type of neighbouring hydroxyl and hydride groups:



These hydride groups then become effective as electron donors when UV light is applied:



The photolysis of chemisorbed hydride (Eq. 7.2) provides directly (e^-) and indirectly ($\text{H}\cdot \rightarrow \text{H}^+ + e^-$) electrons for colour centre formation:



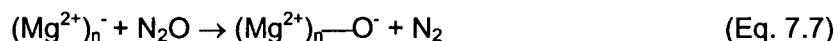
Paramagnetic $(\text{Mg}^{2+})_n^-$ is characterized by EPR and O^{2-}H^+ by FTIR spectroscopy⁴⁰. The presence of diamagnetic species may not be excluded.

Procedure b: In the second procedure MgO samples are exposed to UV light and molecular hydrogen at the same time. Parallel to the reaction channel related to *procedure a* (Eqs. 7.1 - 7.4) a second one has now to be considered which is based on an – at room temperature – reversible heterolytic H_2 splitting process. The resulting hydride groups are non-bridged, i.e., $n=1$. With this modification Eqs. 7.1 - 7.4 also hold for this reaction channel. Furthermore, UV-induced ionisation of low-coordinated surface oxygen anions⁵³ opens up the route to homolytic H_2 splitting⁵⁴ according to

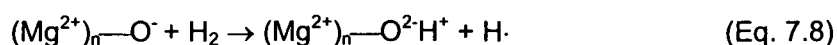


and thus provides additional electrons (e^- , $\text{H}\cdot \rightarrow \text{H}^+ + e^-$) for colour centre formation (Eqs. 7.3 and 7.4).

Procedure c: The third procedure is based on existing F_s centres, which were produced by *procedure b*. These will be – for the sake of brevity – designated colour centres of the 0th generation and are subsequently used as educts for two further consecutive reaction steps. First the F_s centres are bleached by N_2O gas admission according to



At room temperature N_2 does not interact with surface defects to any significant extent¹⁶⁶. The resulting paramagnetic O^- sites are used for homolytic H_2 splitting:



It should be mentioned that, besides serving as an electron source, a considerable fraction of atomic hydrogen out of Eqs. 7.2, 7.4 and 7.6 can also desorb into the gas-phase without participating in any further surface reaction or by becoming active at sites remote from its formation.

7.3. Results

The presented spectra show changes in optical absorption between before and after colour centre formation. After Kubelka-Munk transformation of each experimental reflectance curve, the reference spectrum, acquired right after previous outgassing at 1170 K was subtracted. Since only changes in the optical range $4.1 \geq E \geq 1.6$ eV ($300 \leq \lambda \leq 800$ nm) will be discussed, spectral contributions from optical transitions due to the excitation of low coordinated anions and luminescence effects at energies above 4.1 eV ($\lambda < 300$ nm) are excluded^{50,63}. The same is true for colour centres in the bulk and subsurface region, since their optical absorptions are located around 5 eV¹⁷¹. Under high vacuum conditions, the optical absorption patterns measured after the different preparative steps did not change on a time scale of days.

7.3.1. Colour centre formation by UV-induced oxidation of irreversibly formed hydrides

For *procedure a*, the MgO sample was subjected iteratively to the following three-phase treatment:

- H₂ chemisorption in the dark by sample exposure to 20 mbar H₂ for 60 seconds,
- removal of excess H₂ gas and any reversible H₂ chemisorption product by evacuation,
- UV irradiation ($1 \text{ mW}\cdot\text{cm}^{-1}$ with $1.2 \text{ eV} < h\nu < 6.2 \text{ eV}$) under dynamic vacuum conditions for 5 minutes.

In the UV/Vis spectrum, the reduced MgO surface gives rise to one dominating broad band centred around 700 nm (1.8 eV, Fig. 7.1a), attributed to an electronic F_S centre excitation. A second excitation occurs around 520 nm (2.4 eV) where a weak shoulder appears. On increasing the number of treatment cycles the relative ordinate values increase uniformly in the spectral interval between 320 and 800 nm and exhibit moderate saturation behaviour (Fig. 7.1b and 7.1c). The bandwidths of these absorptions are estimated via band fitting to lie between 0.2 and 0.5 eV. The whole spectral pattern is perfectly bleached after addition of oxidizing agents like N₂O (see Figure 7.3b), proofing that only surface defects are involved.

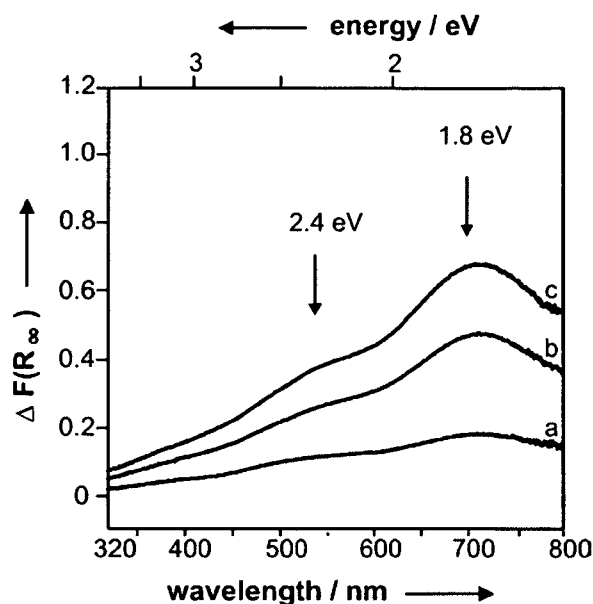


Fig. 7.1: Difference curves between the Kubelka-Munk functions $\Delta F(R_\infty)$ before and after F_S -centre formation according to *procedure a*. The surface colour centres were generated by (a) 1-fold, (b) 5-fold and (c) 15-fold iteration of the following sample treatment: exposure to H_2 (20 mbar, 1 minute), evacuation and subsequent UV activation under dynamic vacuum conditions for 5 minutes and at 298K.

7.3.2. Colour centre formation by simultaneous exposure of MgO to H_2 and UV light

According to *procedure b*, dehydroxylated MgO nanoparticles are exposed to polychromatic UV light and molecular hydrogen (0.1, 1.0, 10, 100 mbar) at the same time*. The contour of the absorption spectra for the lowest H_2 pressure (0.1 mbar, Fig. 7.2a) strongly resembles that observed after multiple treatment cycles of *procedure a* (Fig. 7.1c): again two broad and overlapping bands centred around 520 (2.4 eV) and 700 nm (1.8 eV) appear. The intensity ratio is, however, shifted in favour of that at 520 nm (2.4 eV). This trend holds on when the H_2 pressure in *procedure b* is raised. At the same time both bands exhibit – as in Fig. 7.1 – moderate saturation behaviour. Colour centres resulting from experimental *procedure b* are in the following text denoted as *colour centres of the 0th generation*.

* The UV activation of already irradiated samples can excite or ionise the previously produced colour centres. As a result the respective spectra refer to stationary states, which develop on a time scale of minutes.

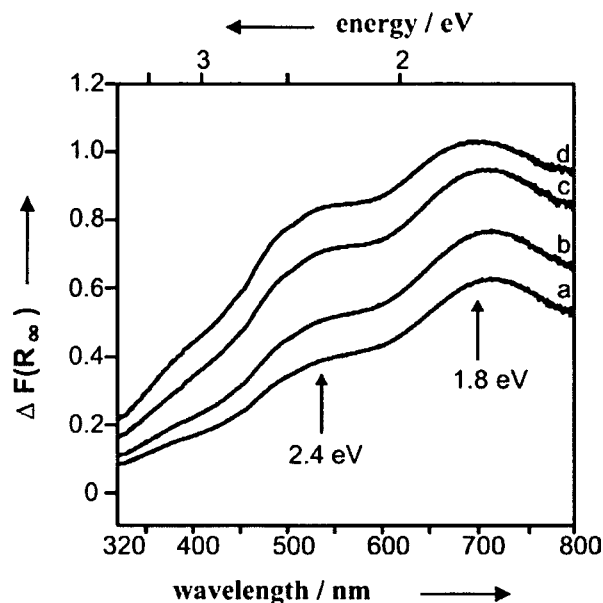


Fig. 7.2: Difference curves between the Kubelka-Munk functions $\Delta F(R_\infty)$ before and after sample activation at (a) 0.1 mbar, (b) 1 mbar, (c) 10 mbar and (d) 100 mbar H_2 with polychromatic UV light for 10 minutes and at 298K. Longer UV exposure times in the presence of hydrogen do not alter structure and intensity of the absorption pattern.

7.3.3. Colour centre formation by homolytic H_2 splitting at O^- sites

Procedure c: The spectrum in Fig. 7.3a is related to F_S centres of the 0^{th} generation and was taken after UV activation of MgO nanoparticles in the presence of 100 mbar H_2 for 600 seconds and subsequent evacuation (see also Fig. 7.2d). As shown in Fig. 7.3b, they are instantaneously bleached upon contacting the sample with N_2O . After another evacuation step and addition of 1 mbar H_2 the sample regains its blue colour. The absorption spectrum of the newly formed F_S centres of the so-called 1^{st} generation (Fig. 7.3c) exhibits distinct differences compared to that of the 0^{th} generation (Fig. 7.3a). The absorption feature centred at 520 nm (2.4 eV) gains relative intensity as compared to that at 700 nm (1.8 eV) and, in addition, a third band at 380 nm (3.2 eV) appears.

Additionally to experiments concerning different mechanisms of generation, preliminary experiments addressing both thermal and photostability of surface colour centres were carried out. For this purpose, a MgO sample containing colour centres of the 1^{st} generation (*procedure c*, Fig. 7.4a) was subjected subsequently either to low energy radiation or thermal treatment under dynamic vacuum conditions. Fig. 7.4b shows the resulting diffuse reflectance UV/Vis spectrum after heating the 1^{st} generation colour centres to 400 K for 5 minutes. Similar results are obtained after exposing the same sample to low energy quanta

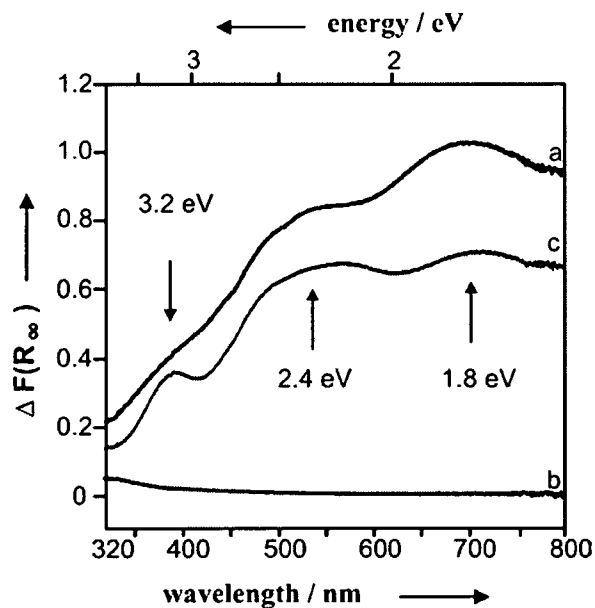


Fig. 7.3: Comparison between F_S centres of the 0th (a) and the 1st generation (c): the curve in (a) was obtained after sample activation with polychromatic UV light at 100 mbar H_2 for 10 minutes. Afterwards, the sample was contacted with N_2O and evacuated. The originally blue sample bleaches out (b). Subsequent addition of 1 mbar H_2 leads to new colouration as shown by Fig. 7.3c.

of $E < 1.5$ eV ($\lambda > 830$ nm). Beside the photoassisted reduction of the whole absorption pattern between 320 and 800 nm, the spectrum in Fig. 7.4b also reveals that the absorption feature centred at 540 nm (2.4 eV) in Fig. 7.4a is actually overlapped by two bands at 480 nm (2.6 eV) and 580 nm (2.1 eV). Furthermore, the depletion process is more effective for colour centres exhibiting transition energies in the low energy region (2.6 – 1.8 eV) than for those absorbing at 3.2 eV.

7.4. Discussion

The energies of the bands observed here are listed in Tab. 7.1 in comparison with other experimental data, obtained either on powder samples (pos.1 and 2) or on epitaxially grown MgO surfaces after defect generation (pos. 3 and 4). There is perfect agreement with the study of Paganini et al.³⁶ performed on high surface area MgO, which was produced by the controlled thermal decomposition of magnesium hydroxide. Apparently, after sample annealing above 1100 K, samples of different preparative origin and morphology^{145,172} contain sites with identical chemical and spectroscopic properties and, consequently, similar electronic structure on an atomic level.

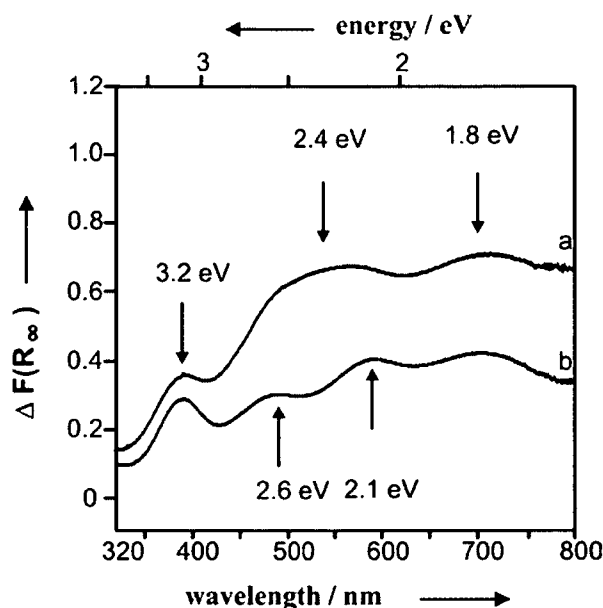


Fig. 7.4: Thermal stability of colour centres of the 1st generation. The difference curves of the Kubelka-Munk functions $\Delta F(R_\infty)$ in (a) and (b) were obtained before and after 5 minutes of thermal treatment of 1st generation colour centres at 400K under dynamic vacuum conditions, respectively.

For MgO as a perfect insulator it was reported that bulk like electronic properties of MgO thin films develop within the first 2-3 monolayers¹⁷³. Hence thin MgO films are appropriate models for polycrystalline MgO surfaces. An early experimental study on the properties of thermally generated defects on MgO (100) thin films by Wu et al.¹⁶⁷ gave electron energy loss features at 5.3, 3.6 and 1.1 eV (Tab. 7.1, pos. 3), which were attributed to electronic excitations of bulk F centres, surface F centre aggregates and surface F centres, respectively. More recently, Kramer et al.¹⁶⁸ have observed a whole set of loss features between 3.4 to 2.0 eV on an epitaxially grown MgO (100) film, which has been subjected to electron bombardment. By comparing the ratio of the intensities of distinct loss features on MgO films grown on a flat Ag (100) and a vicinal Ag (1,1,19) substrate¹⁷⁴, these authors were able to further refine their results and to give an assignment of the loss peaks to electronic transitions of F centres located at differently coordinated sites on the surface. The loss energies 2.4 and 3.4 eV were attributed to multiplet transitions¹⁷⁵ of colour centres located at a terrace site and the measured loss energy of 2.8 eV was assigned to the electronic $1s \rightarrow 2_{x,y}$ transition of a low coordinated colour centre at a step site.

Experiment	Electronic Transitions of F centres [eV]			Sample type
This study	3.2	2.1/ 2.6	1.8	polycryst. CVD
1) Nelson et al. [35]		2-2.3		polycryst. ex hydroxide
2) Paganini et al. [36]	3.3	2.4	1.7	polycryst. ex hydroxide
3) Wu et al. [167]	5.33	3.58	1.15	MgO (100) films
4) Kramer et al. [168]	5.5	3.4/2.4	2.8	1.3/1.0 MgO (1,1,19) films

Tab. 7.1: Compilation of experimental data for optical absorption energies of F_s centres in the bulk and in the surface

The specific loss energies well compare to the UV/Vis bands* observed in the present study (Tab. 7.1) and, thus, nicely relate to the properties of more realistic catalyst materials. A major unknown in our investigation, however, is the charge state of the electron trap. Whether diamagnetic (two electrons) or paramagnetic states (one electron) are present on the surface of MgO nanoparticles and to what extent cannot be decided on the basis of absorption experiments alone: theoretical calculations reveal that paramagnetic and diamagnetic centres have similar transition energies¹⁷⁵, which is experimentally not resolvable due to actual band widths between 0.2 and 0.5 eV. However, the coincidence of certain transitions associated with both types of materials is promising and suggests that similar structural defects are involved. Further corroborating studies are needed to ascertain potential connections between defects on polycrystalline and monocrystalline surfaces.

The abundance of colour centres on MgO nanoparticles clearly depends on the experimental conditions. After application of *procedure a* (Fig. 7.1) one dominating colour centre species absorbing at 1.8 eV is observed. It emerges after the UV-induced oxidation of the hydride group (Eq. 7.2) when the released electron replaces H^- in the corner anion vacancy (Eq. 7.4)¹⁷⁰. The resulting neutral $H\cdot$ radical is – different from the electron (Eq. 7.2) – only weakly bound to the MgO surface³⁸ and, therefore, likely to be mobile on the ionic surface. Thus it may act as reducing agent for any other – possibly remote – type of $(Mg^{2+})_n$ array acting as electron trap. The weak shoulder around 2.4 eV (Fig. 7.1) indicates that one of them is particularly favoured – be it because of its abundance or of its electron affinity. Taking into account the stoichiometric ratio of 1:1 for the electrons and the surface mobile $H\cdot$ radicals (Eq. 7.2), it follows that the surface colour centres emerging at the sites of irreversible

* The multiplets, predicted in a theoretical study (Ref. 175) and observed on MgO films (Ref. 168,174) have not been seen in our experiments.

heterolytic H₂ splitting are the most abundant ones (1.8. eV). The obvious trend of colour centre formation towards saturation on raising the number of treatment cycles (Fig. 7.1) is intimately related to the saturation effect observed for the irreversible heterolytic H₂ splitting process¹⁷⁰.

When UV light and molecular hydrogen ($p(\text{H}_2) > 10$ mbar, *procedure b*) act simultaneously on the MgO surface, a larger reservoir of reducing agents is available since, in addition to the irreversible heterolytic (Eqs. 7.1 – 7.4), both the reversible heterolytic (Eqs. 7.1 – 7.4) and the UV-induced homolytic H₂ splitting⁵⁴ process (Eq. 7.6) become effective. The reversible process – as the irreversible counterpart – provides electrons and H· radicals in the stoichiometric ratio. They emerge, however, from the reversible hydride groups located at step edges (see *procedure b* in Sec. 7.2). Recalling the fact that the electron is likely to stick to the (Mg²⁺)_n array which previously hosted H⁻, we assign the resulting colour centre – according to Fig. 7.2 – to the absorption feature centred at 520 nm (2.4 eV). On the other hand, the UV-induced homolytic H₂ splitting process also provides H· radicals (Eq. 7.6), in addition to electrons (eq. 7.5) which become trapped in a so far unspecified form close to the site of O²⁻ excitation⁶³. The increased supply of mobile H· species should further favour the formation of the colour centre type to which the band at 520 nm (2.4 eV) was attributed. In fact, the relative intensity at 520 nm (2.4 eV) grows faster with the applied H₂ pressure than that at 700 nm (1.8 eV) (Fig. 7.2).

So far colour centres of the so-called *Oth generation* have been discussed exclusively. In the first step of *procedure c* they are bleached by N₂O addition (Eq. 7.7). The respective UV absorption bands (Fig. 7.2d and 7.3a) as well as the EPR signal components^{89,176} vanish completely. The latter ones are replaced by those of surface O⁻ species^{89,176} which are then available for homolytic H₂ splitting according to Eq. 7.8. After all, the colour centres of the *Oth generation* are replaced by isolated OH groups and surface mobile H· radicals. These are available for probing the MgO surface for anion vacancies as electron traps, which have not yet been consumed by previous reaction steps (Eqs. 7.3, 7.4, and 7.7). In fact, Fig. 7.3c shows that the absorption bands at 1.8 and 2.4 eV observed during the *procedures a* and *b* reappear even though with strongly changed relative intensities. The H· radicals formed in the course of homolytic H₂ splitting (Eq. 7.8) are likely to be supplied with so much excess energy that they reach (Mg²⁺)_n arrays on the surface of the MgO sample which were previously not accessible in both *procedures a* and *b* for H₂ molecules (Eq. 7.1) and/or UV quanta (Eq. 7.2). Among them are sites where – in principle – irreversible or reversible heterolytic H₂ splitting may occur. Of course, they are likely to preferentially act as local potential minima for the electrons of mobile H· radicals and thus to explain the appearance of

the same band positions in *procedure c* on one hand and *procedures a* and *b* on the other. The most striking observation is, however, the presence of a third comparatively sharp absorption band at 3.2 eV (380 nm) which is absent in the experiments based on *procedures a* and *b*. Quantum chemical calculations^{38,39,175} predict the excitation energy of electrons trapped in anion vacancies and O²⁻ anion deficient (Mg²⁺)_n arrays in general (Fig. 7.5). The value for an ideal surface colour centre in a perfect (100) plane is in good agreement with the absorption band around 3.2 eV. As there are neither experimental nor theoretical evidences for a heterolytic H₂ splitting at the respective type of (Mg²⁺)_n array, a direct electron transfer from a hydride to the vacancy in a perfect (100) plane appears, therefore, not to be possible. Consequently the abundance of the corresponding surface colour centres in *procedures a* and *b* does not reach the detection limit of UV/Vis absorption spectroscopy. On the other hand, under the experimental conditions during the formation of 1st generation colour centres, H· radicals may dispose of sufficiently high kinetic energy in order to reach single anion vacancies in (100) planes and to be trapped there.

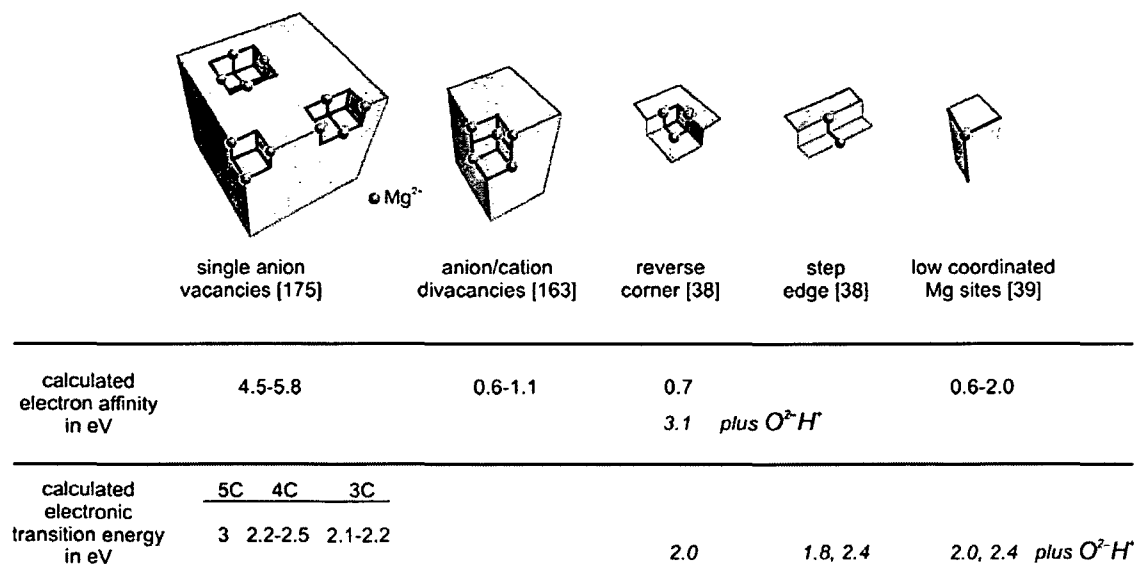


Fig. 7.5: Models, calculated electron affinities and electronic transition energies of electron traps on the surface of MgO.

The quantum chemical calculations also show that shallow (Mg²⁺)_n electron traps may be strongly stabilized by closely spaced surface OH groups (Fig. 7.5)³⁹. These emerge under the experimental conditions described in the present paper in both heterolytic cleavage of H₂ and electron transfer from mobile H· radicals to (Mg²⁺)_n traps. According to the calculations the excitation energies at 1.8 and 2.4 eV (Fig. 7.4) are likely to be related to such surface-OH-stabilized electron centres. On the other hand, it has to be emphasized that the colour

centre absorbing at 3.2 eV is attributed to a non-OH-stabilized colour centre – in agreement with the fact that heterolytic H₂ splitting and thus hydride formation does not occur at the respective anion vacancy (see above). Relevant support for the tentative assignments given here stems from IR and EPR spectroscopic studies revealing electronic and magnetic coupling, respectively, between closely spaced surface OH groups and surface trapped electrons on MgO surfaces⁴⁰.

A moderate temperature rise from 300 to 400 K already partially bleaches the absorption bands at 2.4 and 1.8 eV (Fig. 7.4), which are related to sites of heterolytic H₂ splitting. The band at 3.2 eV, on the other hand, survives essentially unaffected. This experiment reveals that the whole absorption pattern between 2.5 and 1.5 eV is made up from more than two types of differently stable electron centres. The influence of the surface OH groups on neighbouring trapped electrons may also help in the attempt of understanding the comparatively low thermal stability of most of the electron centres absorbing in the spectral interval between 3 and 1.5 eV. In fact, the quantum chemical calculations clearly show a wide variety of surface electron traps, the electron affinity (EA) and the transition energy of which depend on both the structure of the local (Mg²⁺)_n array and the presence of a closely-spaced OH group. Fig. 7.5 only contains a limited selection of such surface sites. The thermal energy supplied in the bleaching process is only a fraction of the ionisation energy required for the surface species in question. It may, however, suffice to excite a low-energy mode of the OH group involved and thus initiate a reaction channel:



This hypothesis, even though highly speculative, is, however, intimately related to reliable strategies of corroboration: In the course of the bleaching process specific surface OH groups must definitely disappear and hydrogen must emerge in the gas-phase. The respective experiments are in the process of being prepared in our laboratory.

7.5. Conclusions

In the present study we have shown, that on the surface of polycrystalline MgO colour centres are formed selectively by applying different kinds of formation procedures involving two types of electron donors: hydride ions and H· radicals. The former ones are related to hydrogen chemisorption sites on the surface, which are subsequently also the main electron

trapping centres. $H\cdot$ radicals, on the other hand, are mobile on the surface and, therefore, able to reach remote electron traps, which are not directly involved in the hydrogen photochemistry on MgO. The transition energies of the colour centres are in reasonable agreement with studies on MgO thin films, which is an evidence for the morphological uniformity of MgO samples of different origin. Although the assignment of the observed absorption features to optical transitions of specific structural surface entities capable of trapping electrons and their stability is not entirely unambiguous, the results presented here provide some further important insights into the defect chemistry on MgO.

8. Magnetic properties of surface trapped electrons

8.1. Introduction

The surface properties of metal oxide materials, in terms of chemical reactivity or as substrate for metal clusters, are determined by local geometrical irregularities, so-called surface defects¹⁷⁷. These include sites of low coordination (LC) and ion vacancies. For understanding the structure-reactivity relationship of metal oxide surfaces the detailed investigation of surface defects is indispensable. On single crystalline model systems, the concentration of surface point defects is small, and this makes it difficult to obtain relevant information by classical surface science analyses. On the other hand, polycrystalline materials prepared by non-equilibrium techniques exhibit an enhanced concentration of point defects, which are accessible to different kinds of molecular spectroscopy. The inherent disadvantage is, however, the plethora of ill-defined structures that are expected to be found on the surface of nanometer- to micrometer-sized crystallites.

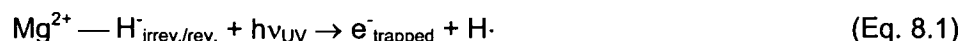
Electron paramagnetic resonance (EPR) spectroscopy has become a powerful method for the investigation of point defects, due to its high sensitivity, and to the copious body of geometric and electronic information extractable from the corresponding spectra¹⁷⁸. Prototype examples of EPR active point defects on magnesium oxide, MgO, are paramagnetic surface colour centres or F_S^+ centres. In principle, these species correspond to electrons trapped on the MgO surface at sites of sufficient electron affinity. An often reported paramagnetic defect is the so-called $F_S^+(H)$ centre. It is manifested by a characteristic EPR signal that arises from the electron spin interaction with the surrounding Mg cations plus a significant magnetic interaction with the proton of a nearby OH group. The latter effect is observed in EPR as super-hyperfine splitting of the resonance lines into a doublet^{35,162,179}. Spectrum simulation of this very specific signal structure provides accurate values for the g tensor and hyperfine splitting parameters, which can also be analysed by theoretical modelling.

Only one dominating type of $F_S^+(H)$ centre has been observed in EPR studies performed on diverse types of highly dispersed MgO particles, which had been previously activated at temperatures above 1170 K and pressures below 10^{-5} mbar³⁶. There are, however, further contributions of less abundant surface colour centre species, which superimpose on the dominating $F_S^+(H)$ pattern⁸⁹.

The first structural model for $F_S^+(H)$ centres was proposed by Tench and Nelson³⁵. This model described the centres as electrons trapped in anion vacancies located in the MgO(100) surface plane. Recently, theoretical and experimental results have given new insights into the electron trapping properties of irregular MgO surface arrays, such as low coordinated (LC) vacancies¹⁸⁰, step edges, reverse corners³⁸ and even single, LC Mg ions³⁹. Different from the classical oxygen anion vacancies at (100) planes (5C), on edges (4C) or on corners (3C), the new electron trap locations were classified as so-called shallow traps; these can – according to the calculations^{160,163} – transform into deep traps when a stabilizing surface hydroxyl proton is available in sufficiently close vicinity to the unpaired electron³⁹. Because the local structure of this electron trap has little in common with a classical colour centre F_S^+ , Pacchioni et al.³⁸ suggested to replace the respective symbol $F_S^+(H)$ by $(e^-)(H^+)$ as a more general and appropriate designation. This symbol will also be adopted in the present study, whereas the symbol F_S^+ will be applied to the total of surface colour centres that are related to EPR signals without measurable hyperfine couplings with neighbouring protons.

The significant magnetic interaction between the trapped electron and the nearby hydroxyl group leads to the conclusion that the underlying surface defect also has to be involved in the – at room temperature – irreversible or reversible heterolytic splitting process of H_2 ³⁶. In any case, combined infrared and EPR studies revealed that, when hydrogen and UV light are present at the same time, several processes can occur to produce trapped electrons^{36,162,170}. The complex chemistry of H_2 on MgO has been discussed in detail in Sec. 7.2. Here only a short summary shall be given:

To begin with, hydride groups that originate from heterolytic H_2 splitting may be subject to UV photolysis, producing electrons and $H\cdot$ radicals.



The photogenerated hydrogen radicals from Eq 8.1 can be oxidized upon further electron trapping.



In addition, low coordinated oxygen ions can be photoexcited and, subsequently, ionised to give surface O^- and electrons⁸⁹. The released electrons are then trapped at the surface. The resulting electron states exhibit ionisation energies of about 2 eV⁶³.



On the other hand, the O^{-} centres generated by UV excitation split H_2 homolytically to produce surface OH groups and $\text{H}\cdot$ radicals⁵⁴.



Similar to the $\text{H}\cdot$ radicals released in the course of UV-induced hydride oxidation (Eq. 8.1), the $\text{H}\cdot$ radicals produced in Eq 8.4 are mobile on the surface until they get trapped at appropriate surface structures with sufficient electron affinity (Eq. 8.2). The surface states that result from these simultaneously occurring processes are referred to in the following text as *colour centres of the zeroth generation*. One would assume a complex EPR pattern originating from the superimposition of the $(e^{-})(\text{H}^+)$ and other colour centre signals. However, the number of observable paramagnetic surface sites is, opposite to the diversity expected for the polycrystalline material, rather limited. This surprising observation was explained by the fact that different closely spaced signals cannot be resolved by X-band measurements¹⁷⁶.

In the realm of magnetic resonance spectroscopy on MgO surfaces, a way to overcome the problem of overlapping signals of electron traps is the detailed address of hyperfine coupling effects induced by the magnetic dipole interaction between the electron spin of colour centre electrons and the nuclear spin of neighbouring ^{25}Mg cations ($I=5/2$) and protons ($I=1/2$). The successful combination of EPR and electron nuclear double-resonance (ENDOR) spectroscopy¹⁸¹ revealed a well-defined heterogeneity of trapped electron species on activated alkaline earth metal oxides (MgO, CaO and SrO)¹⁸². Among these trapped species, the $(e^{-})(\text{H}^+)$ was common to all studied oxides.

Further attempts were made to unravel the composite signal by an indirect technique. N_2O bleaches the paramagnetic electron traps $(\text{Mg}^{2+})_n^{-}$ and produces O^{-} ions, which remain either adsorbed on the surface or even get incorporated into the local structure, which previously hosted the trapped electron.



The O^{-} ions have characteristic EPR signals that strongly differ from those related to trapped electrons. Since the respective g tensor depends sensitively on the magnitude and the symmetry of the electrostatic field felt by the anion, the O^{-} ions have turned out to be excellent candidates to probe the distribution of electron traps¹⁷⁶. The spectra obtained after

the reaction of colour centres of the zeroth generation with N_2O show well-resolved features, which permit an accurate determination of the g values of at least five different O^- radical species^{89,176}. As their UV induced counterparts (Eq. 8.3), these radicals produce $H\cdot$ radicals from molecular H_2 (Eq. 8.4), which again act as electron sources for different traps that had not been involved in previous electron trapping processes^{89,176}. We will refer to this newly formed category of species, produced in the absence of UV light, as *colour centres of the first generation*.

By this study, we want to disentangle the complex EPR pattern that originates from electrons trapped on the MgO surface. The strategy is based on a previous investigation (Sec. 7)¹⁸³: By applying different hydrogen-based reducing agents, it is possible to address specific reaction channels of the overall process described by Eqs. 8.1 to 8.5. The optical absorption properties of colour centres, which include both paramagnetic and diamagnetic states, exhibit significant differences depending on the formation procedure. These differences are shown in Fig. 8.1 and can be summarized as follows: essentially two absorption features at 1.8 and 2.4 eV were observed, with their relative intensities depending differently on the hydrogen pressure applied during UV irradiation (Fig. 8.1a and b). This fact has been explained in terms of changes in the relative abundance of hydride groups stemming from H_2 chemisorption at different surface defects¹⁸³. The bleaching of colour centres with N_2O , followed by evacuation and subsequent addition of molecular hydrogen, is related to the appearance of a new band at 3.2 eV (Fig. 8.1c), which leads to the conclusion that the underlying defect is not involved in heterolytic hydrogen chemisorption reactions or in the subsequent UV-induced hydride oxidation. These significant differences in the optical absorption spectra¹⁸³, together with the complex outcome of O^- ions derived from the electron traps^{89,176}, motivated us to reinvestigate the nature of the corresponding paramagnetic sites.

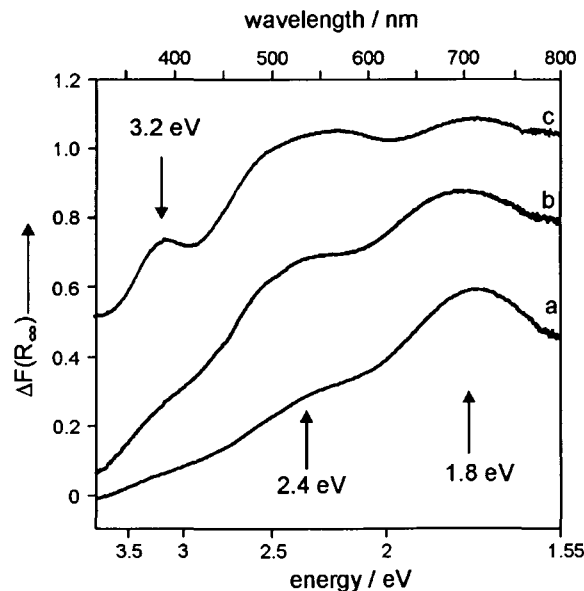


Fig. 8.1: Diffuse reflectance UV/Vis spectra of colour centres on the surface of MgO obtained after different preparation techniques: a) irradiation of preadsorbed H_2 , b) zeroth-generation colour centres, and c) first-generation colour centres (see Ref. 183)

Another objective of our study was to address the open question whether the sites that host $(e^-)(H^+)$ centres are effective in the heterolytic splitting of H_2 . For this purpose, a combination of infrared spectroscopy and EPR spectroscopy was employed. As shown previously, this approach links the H_2 chemisorption, which occurs in the dark and under the influence of UV light, with the activity of specific surface structures in electron trapping¹⁷⁹.

8.2. Results

8.2.1. Colour centre formation by UV-induced oxidation of irreversibly formed hydrides

The adsorption of molecular hydrogen on the surface of MgO powder at room temperature gives rise to two heterolytic chemisorption complexes, each of them consisting of one hydride ($Mg^{2+}H^-$) and one hydroxyl group ($O^{2-}H^+$)¹⁷⁰. Upon evacuation, only one of these complexes is stable at room temperature and offers a hydride as electron source, according to Eq. 8.1. Iterative experiments comprising consecutive steps of H_2 adsorption (20 mbar), evacuation, and subsequent UV irradiation for 10 min were carried out. In Fig. 8.2, the colour centre signals present after the first and the fifth cycle are shown. The spectra are composed of essentially two colour centre components, the most apparent of which is the well-known $(e^-)(H^+)$ centre with its characteristic super-hyperfine coupling constant of the perpendicular signal component of 2.06 Gauss. In addition, an uncoupled species with perpendicular and parallel signal components of $g_{\perp}=2.000$ and $g_{\parallel} = 2.0014$, respectively, designated in this study as F_{S^+A} (indicated in Fig. 8.2) is present.

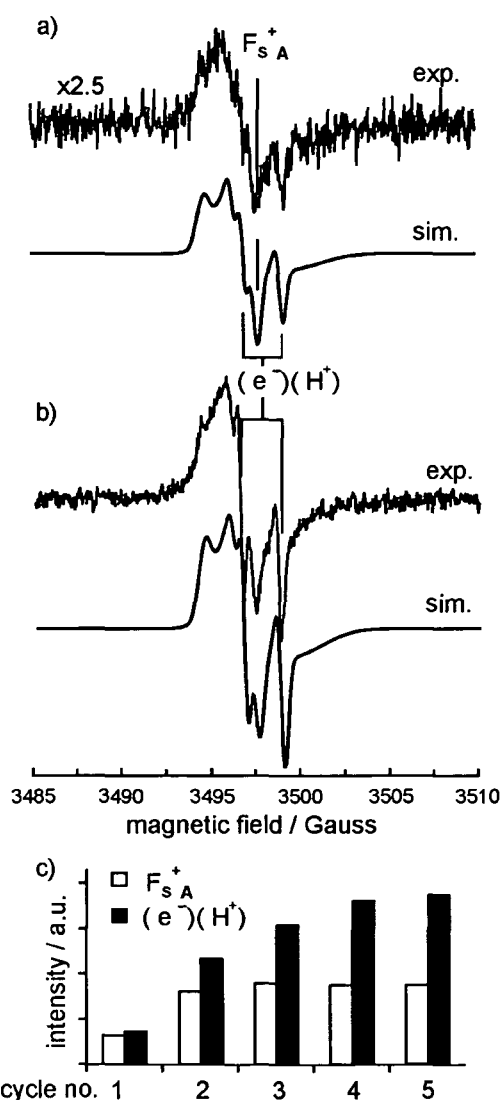


Fig. 8.2: EPR colour centre signals after preadsorption of hydrogen and subsequent UV activation. The spectrum in a) corresponds to the first run of cycles comprising the consecutive H_2 exposure-, evacuation- and UV exposure steps. Spectrum b) was acquired after five iterations. The diagram in c) contains the relative concentrations of F_{S^+A} and $(e^-)(H^+)$ centres with increasing number of cycles.

	g_{\parallel}	g_{\perp}	I_{\parallel}	I_{\perp}
(e ⁻)(H ⁺)	2.0016	1.9998	0.55	0.45
	$A_{\parallel} = 0.31$ G	$A_{\parallel} = 2.06$ G		
F _S ⁺ [A]	2.0014	2.0000	0.55	0.55
F _S ⁺ [B]	2.0019	2.0008	0.4	0.5
F _S ⁺ [C]	2.0017	2.0004	0.55	0.55
background	2.0006-2.0011	1.9984-1.9993	2.0-2.5	3.0

Tab. 8.1: EPR parameters (g value, linewidth I , hyperfine coupling constant A) of paramagnetic colour centres on the surface of MgO.

The shape of the EPR signal remains essentially unchanged with increasing number of cycles. The intensity of the total EPR signal increases up to the fifth cycle and remains constant thereafter.

To determine the spin Hamiltonian parameters, and to measure the relative abundance of different paramagnetic species, spectrum simulations were performed (Fig. 8.2)*. The respective EPR parameters are listed in Tab. 8.1. A broad background component was added to improve the quality of the fit and to mimic the heterogeneity of sites of minor abundance**. In Fig. 8.2c the relative concentrations of the (e⁻)(H⁺) and F_S⁺_A centres are plotted as a function of the number of repeated preadsorption cycles. Starting with a ratio of almost 1:1 between F_S⁺_A and the (e⁻)(H⁺) centre after the first cycle, the ratio shifts in favour of the (e⁻)(H⁺) centres with increasing number of applied cycles.

* In each case the overall signals could be satisfactorily simulated using aside from F_S⁺_A and (e⁻)(H⁺) two additional colour centre species labelled here as F_S⁺_B and F_S⁺_C with a relative abundance below 10%.

** Since the presented X-band spectra are composed by several signals, which overlap in the same restricted magnetic field range, the simulation approach used is not totally unambiguous with respect to the selected symmetry of the simulated spin centres and, consequently, with respect to their exact intensities. A more complete analysis is beyond the scope of this investigation and would also involve independent measurements at different frequencies (Q band, W band). However, the approach applied is sufficient for the purpose of this study, which is to show trends in the abundance of specific centres as a function of production and differences in the saturation behaviour. The origin of the background (see also Fig. 8.4) is ascribed to the heterogeneous distribution of undefined and less abundant paramagnetic electron centres on the surface of MgO, which emerge during colour centre formation.

8.2.2. Colour centre formation by simultaneous exposure of MgO to H₂ and UV light

The reversible chemisorption complex of H₂ becomes more abundant upon raising the H₂ pressure. Under simultaneous UV irradiation, its hydride groups are active as electron sources, according to Eq. 8.1. The colour of the sample turns blue and an EPR colour centre pattern, designated here zeroth generation, is observed (Fig. 8.3a). Its contour is similar to that related to stable hydride groups as electron sources (see Sec. 8.2.1, Fig. 8.2). It clearly depends on the microwave power P_{MW} (Fig. 8.3a and 3c) and consists of two dominating constituents. A detailed deconvolution is presented in Sec. 8.2.4. The evacuation and subsequent admission of N₂O bleaches the blue colour, as well as the colour centre signals and gives rise to the appearance of O⁻ signals in the EPR spectrum (Eq. 8.5).

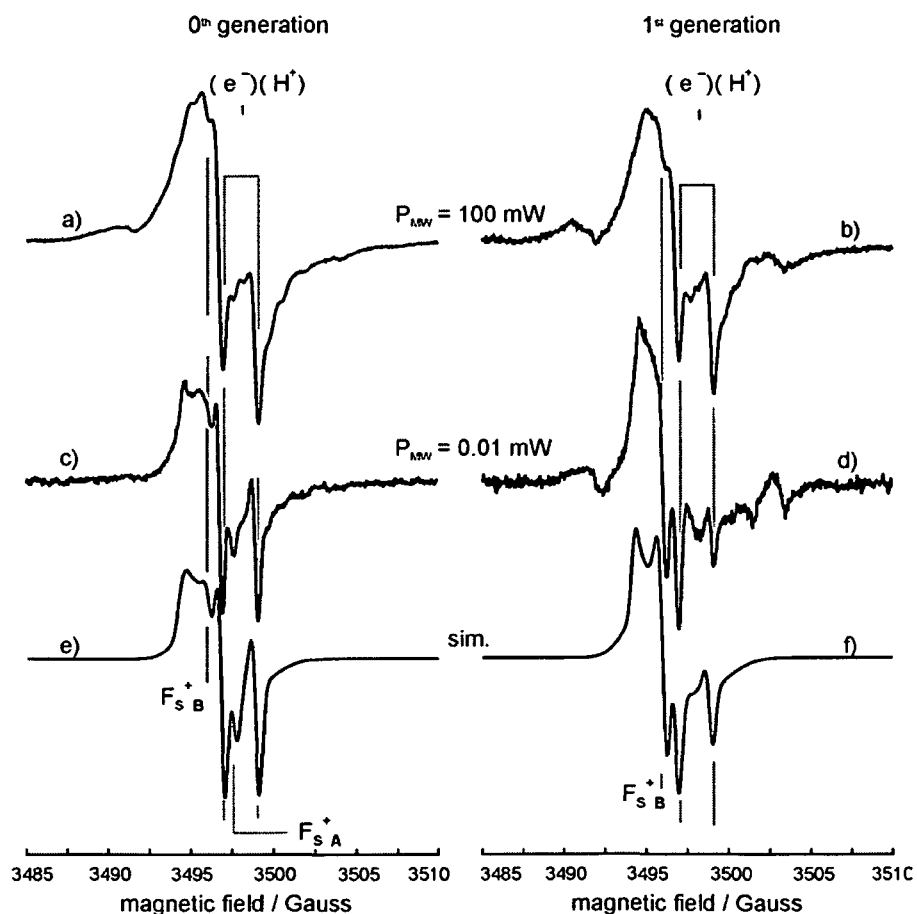


Fig. 8.3: EPR signals of colour centres on MgO nanoparticles: after UV treatment in hydrogen [zeroth generation, (a) and (c)] and after chemical production (see text) of H[•] radicals (b) and (d). The applied microwave power for the acquisition of the spectra was 100 mW in (a) and (b), and 10 μ W in (c) and (d).

8.2.3. Colour centre formation by homolytic H₂ splitting at O⁻ sites

Surface O⁻ centres out of Sec. 8.2.2 split H₂ homolytically (Eq. 8.4). The resulting H· radicals act as electron sources for colour centre formation. Therefore, H₂ admission restores the blue colour and an EPR colour centre pattern (Fig. 8.3b), which we designate first generation, is observed.

8.2.4. Comparison of the zeroth and the first generation colour centres

A comparison of the signals of the zeroth with the first generation colour centres acquired with a microwave power of P_{MW} = 100mW (Figs. 8.3a and 8.3b) reveals a strong similarity of

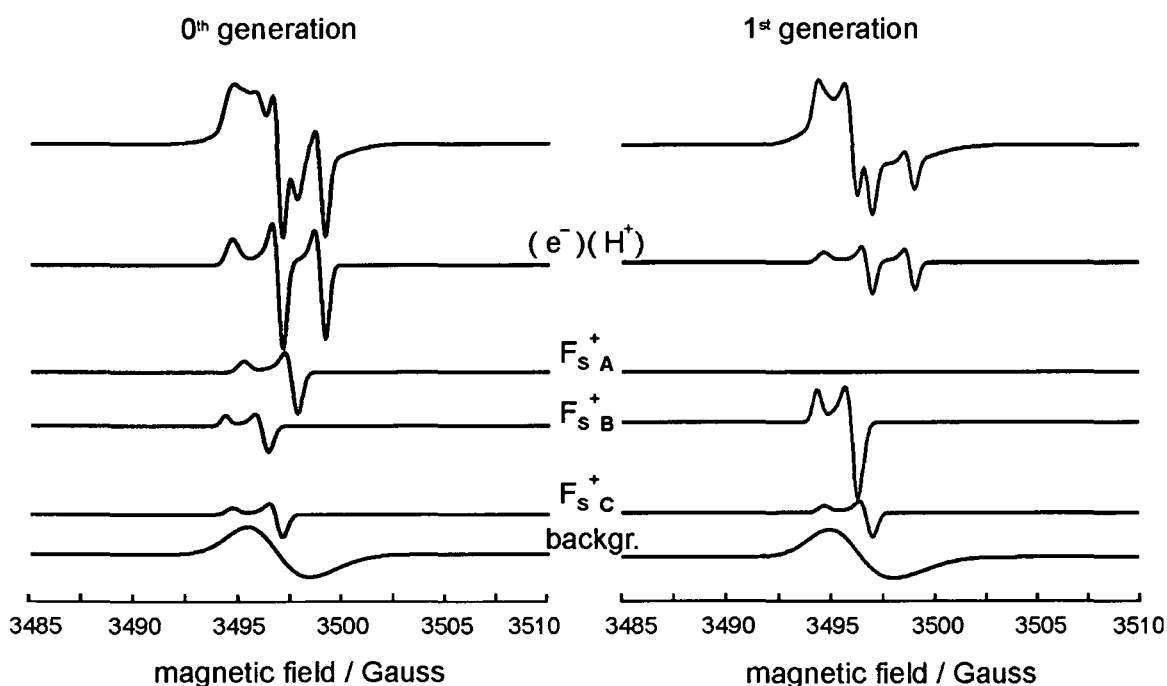


Fig. 8.4: Deconvolution of the simulated signals shown in Figs. 8.3e and 8.3f into the simulated profiles of four colour centre species and a background component.

the respective signal contours. Major differences are, however, observed after recording the EPR spectra at a microwave power of 0.01 mW (Figs 8.3c and 8.3d). This points to the following fact: There are different paramagnetic sites, which saturate at different microwave power levels.

The deconvolution of the signals in Figs. 8.3e and 8.3f into their constituents was performed using the same *g* parameter as that used in Sec. 8.2.1. The spectra recorded at 0.01 mW were analysed because the differences are most apparent at this power level. Fig. 8.4 shows

the results of the deconvolution, and in Fig. 8.5 the relative abundance as a function of the colour centre production is plotted. The following conclusions can be drawn:

- The $(e^-)(H^+)$ species is the most abundant species in the EPR signal of zeroth generation colour centres.
- The F_{S^+A} species, which was observed after colour centre formation by irradiation of preadsorbed hydrogen (Sec 8.2.1), contributes to the zeroth generation colour centres but is absent in the first generation.
- The abundance of F_{S^+B} species is substantially greater in the first colour centre generation than in the zeroth generation.
- At low P_{MW} the abundance of F_{S^+B} species in the first generation colour centres exceeds that of $(e^-)(H^+)$ centres.

The intensity data of surface colour centres over the microwave power range 0.01 mW – 50 mW* are plotted in Fig. 8.6. In the low power regime (0.01-0.1 mW) the spectra are dominated by the signals of $(e^-)(H^+)$ and F_{S^+B} (Fig. 8.6a), and contain minor contributions of a species designated as F_{S^+C} (Tab. 1, Fig. 8.4). When going to higher P_{MW} , the relative concentration of F_{S^+B} , and F_{S^+C} decreases, while the $(e^-)(H^+)$ concentration increases and, finally, dominates at high P_{MW} (> 1 mW). These results clearly show that the various colour centre species exhibit significantly different saturation

characteristics with respect to their EPR transitions. The corresponding saturation curves, that is, the dependence of the EPR signal intensities on the square-root of the microwave power, are shown in Fig. 8.6b. In the low P_{MW} regime (see inset in Fig. 8.6b), all F_{S^+} centres rise linearly with P_{MW} , which indicates that the respective EPR transitions are not saturated. However, at $P_{MW}=0.1$ mW the curves for F_{S^+B} and F_{S^+C} level off, while that for $(e^-)(H^+)$ continues increasing, though with decreasing slope. The saturation behaviour of the EPR signal of F_{S^+A} , which is identical to that of F_{S^+B} or F_{S^+C} , was determined from the respective

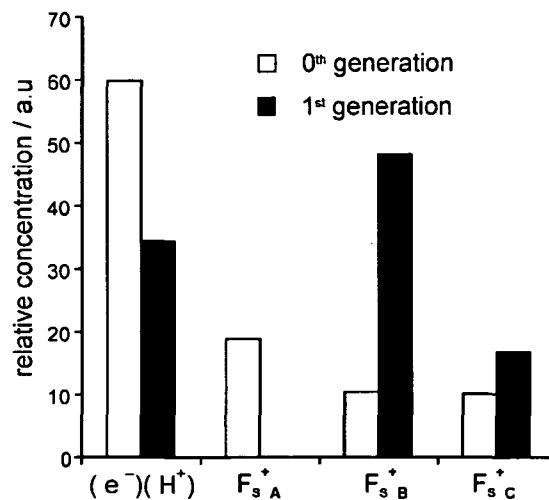


Fig. 8.5: Plot of the relative concentrations of colour centres as a function of the production process. The values were determined on the basis of the simulations shown in Fig. 8.4.

* We have not considered the spectra measured at 100 mW for this analysis because of difficulties in simulation due to strong contribution from the background.

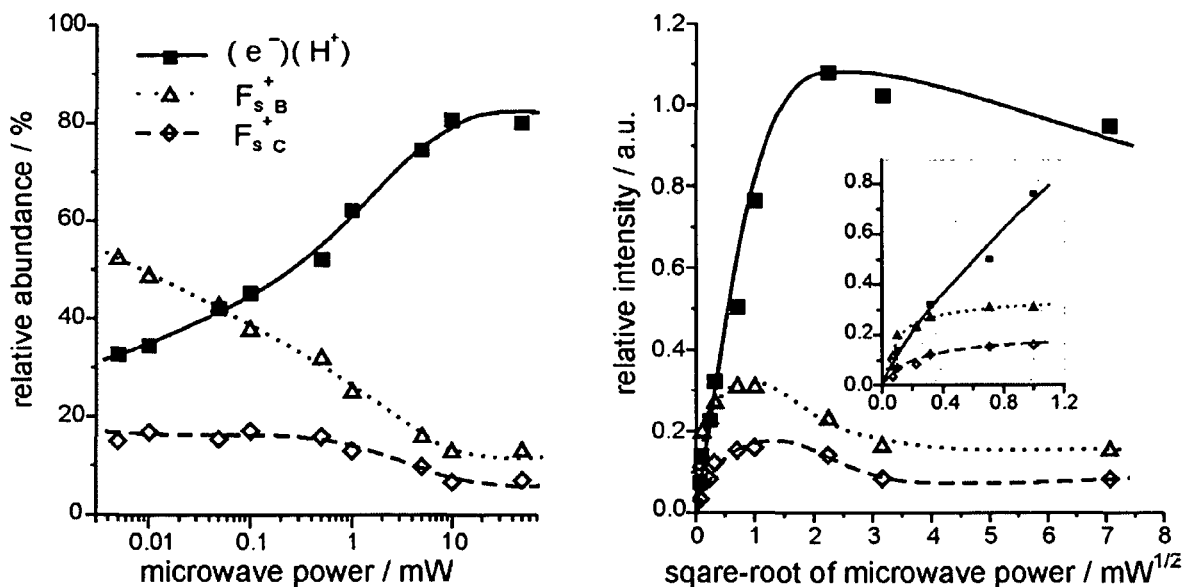


Fig. 8.6: a) Relative abundance of individual first-generation colour centre species as a function of the microwave power. b) EPR saturation curves for the individual colour centre species.

spectra of zeroth generation colour centres (not shown here). To sum up this analysis, the $(e^-)(H^+)$ centre exhibits outstanding saturation properties due to the enhanced relaxation probability of the spin state.

8.2.5. Electronic interaction between colour centre electrons and protons evidenced by IR spectroscopy

The electronic interactions between trapped electrons and the protons of nearby hydroxyl groups can be measured via the shift of the IR absorption of the respective hydroxyl stretching bands⁴⁰. Therefore, in analogy to the EPR investigation, we have performed IR experiments addressing the formation of zeroth and first generation colour centres. In Fig. 8.7, the OH stretching region of the resulting IR spectra is shown.

The heterolytic chemisorption of hydrogen at elevated pressures (> 10 mbar) leads to two adsorption complexes, associated with OH bands at 3712 cm^{-1} and 3465 cm^{-1} (Fig. 8.7a). As in the experiments described in Figs. 8.3a and 8.3c, the colour centres of the zeroth generation were formed by UV irradiation of the MgO sample in H_2 atmosphere for 10 min. The IR spectrum in Fig. 7b reveals new spectral features at 3632 , 3602 and 3528 cm^{-1} ¹⁸⁴. Due to the interaction of the proton with a neighbouring proton acceptor, these OH bands are shifted to lower wavenumbers as compared to free OH groups. In a previous study, we assigned these bands to OH groups interacting with colour centre electrons⁴⁰. The intensities of the bands at 3632 cm^{-1} and 3602 cm^{-1} do not change with the H_2 pressure applied (1-100 mbar) during UV irradiation. For this reason, these bands can be attributed to hydroxyl ions

that originate from irreversible, heterolytic hydrogen splitting on the MgO surface (Eq. 8.1, Ref. [179]).

After admission of N_2O (Fig. 8.7c), the features that are attributed to OH groups interacting with colour centre electrons (Fig. 8.7b) disappear; this observation is in line with the bleaching of colour centres observed in EPR. Subsequent hydrogen admission in the dark (formation of first generation colour centres, Fig. 8.7d) leads to an OH band at 3532 cm^{-1} , which is slightly shifted with respect to the band at 3528 cm^{-1} in Fig. 8.7b. However, the bands at 3632 cm^{-1} and 3602 cm^{-1} do not reappear. Based on previous studies^{40,179,184} the bands observed at 3532 cm^{-1} and 3528 cm^{-1} in the zeroth and the first generation, respectively, are attributed to the presence of $(e^-)(H^+)$ centres. The slight wavenumber shift can be explained by means of a chemical modification of the surface in the course of the previous reaction steps applied (e.g., different levels of hydroxylation).

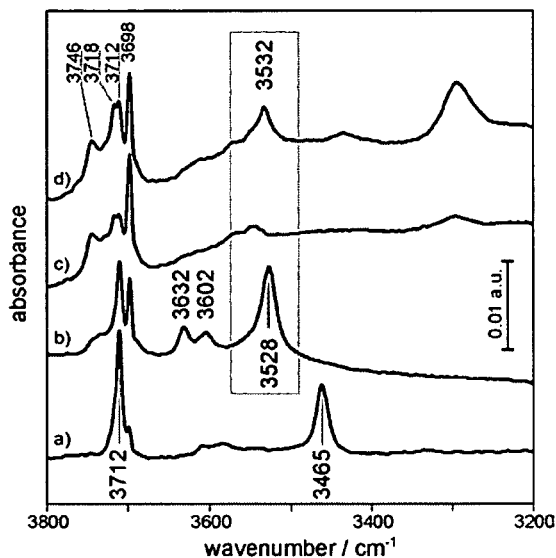


Fig. 8.7: OH stretching region of the IR spectra related to the formation of zeroth- and first-generation colour centres on the surface of MgO. a) Chemisorption of hydrogen (100 mbar); b) formation of zeroth-generation colour centres by UV irradiation under H_2 atmosphere; c) bleaching of colour centres by N_2O after removing the H_2 atmosphere [admitted in (b)]; d) formation of first-generation colour centres by subsequent admission of H_2 . The bands at 3700 cm^{-1} and above originate from dark reactions between residual adsorbed hydrogen species and N_2O . They do not relate to the process of electron trapping and are extensively discussed in Ref [184].

8.3. Discussion

Most of the studies on the properties of surface colour centres on MgO reported so far aimed at a structural classification of the experimentally observed features. Contrary to the case of colour centres in the bulk, where the model of electrons trapped in anion vacancies is well established¹⁷¹, a definitive assessment of electron trapping sites on the surface in terms of their local geometry is enormously complicated, if at all possible. This is related, on one hand, to the huge variety of structural surface defects that can act as electron trapping sites. Recent theoretical calculations have shown that almost every array of low coordinated Mg^{2+}

ions with a local O^{2-} deficiency has sufficient electron affinity to trap electrons at room temperature or below^{38,39,160,163,180}. A reasonable agreement between theory and experiment was achieved for the OH-stabilized electron trap on a single Mg^{2+} cation in the corner position as proposed in Ref. [39]. Despite the high number of possible structures proposed by theory^{38,39,160,163}, there is only one prevailing type of EPR signal, namely, that attributed to the $(e^-)(H^+)$ centre. The discrepancy between the number of paramagnetic colour centre species and a much higher number of derived O^- species (see Sec. 8.1 and Ref. [176]) may originate from the fact that EPR spectroscopy is only capable of detecting the paramagnetic states, but not diamagnetic ones. Another reason may be that the characteristic doublet splitting of the $(e^-)(H^+)$ centre measured by continuous wave (cw) EPR in X-band, is the only unambiguously resolvable feature of the complex colour centre signal envelope. To disentangle this feature, we have concentrated herein on two aspects: (1) the careful analysis of the colour centre EPR signal as a function of microwave power and (2) the preferential address of specific trapping sites by selected hydrogen-based reducing agents.

In a previous study, Pinarello et al. reported and discussed the nature of zeroth and first generation colour centres on MgO ¹⁷⁶. Although different sites are involved in the production process during these experiments, they found that the EPR spectra of colour centres of the zeroth and the first generation are qualitatively the same. This is in conflict with results of an earlier study performed by us⁸⁹, where we observed a clear difference between the EPR spectra, although essentially the same experimental conditions as those reported in Ref. [176] were applied.

Giamello et al. described the saturation behaviour of colour centres of the zeroth generation in a microwave power range between 0.1 and 10 mW¹⁶². In that study, three single species, namely the characteristic $(e^-)(H^+)$ species, a second centre with essentially the same g parameters as those reported for $F_S^+ B$ in this study and a subsurface species (not observed in the present study), were discriminated. The former two species, $(e^-)(H^+)$ and $F_S^+ B$, were found to exhibit the same P_{MW} saturation characteristics down to 0.1 mW.

According to Fig. 8.4, more than two paramagnetic species contribute to the complex signal envelope. To obtain a reasonable fit in the simulation, we used, in addition to the $(e^-)(H^+)$ centre, three uncoupled species with axial symmetry (Tab. 8.1). The expansion of the P_{MW} range down to 0.01 mW provides insights in the saturation behaviour of all colour centre EPR signals and reveals a significant difference between the signals acquired at low and high P_{MW} (see the first colour centre generation in Figs. 8.3b and 8.3d). The relative contribution of the $(e^-)(H^+)$ centre to the overall signal is significantly less at low P_{MW} (below 0.1 mW) where the

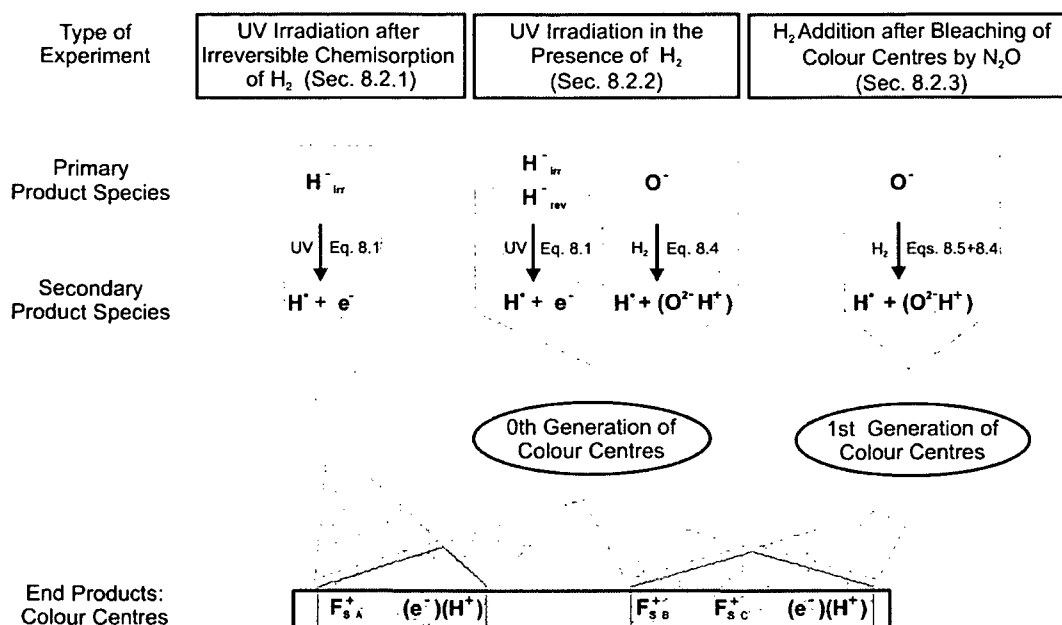


Fig. 8.8: Reaction channels contributing to electron trapping on MgO surfaces exposed simultaneously to H₂ gas and UV irradiation.

relative contributions of the individual species vary considerably (Fig. 8.5a). An analysis of the saturation characteristics of individual colour centre species allows a quantitative evaluation of this phenomenon. In the low P_{MW} regime, the intensity of the paramagnetic species rises linearly with increasing microwave power, which indicates the occurrence of non-saturated EPR transitions. In this regime, the population difference between the excited spin state and the ground state is sufficiently maintained by spin-lattice relaxation. However, as the microwave power is increased, the transitions of the uncoupled colour centres begin to saturate, which can be clearly observed by the levelling off of the respective saturation curves (Fig. 8.6). Above 1 mW, the signal form of the EPR spectra does not change significantly and the intensity of the (e⁻)(H⁺) centre continues increasing and saturates only at 5 mW. As a major consequence, a quantitatively meaningful assessment of the relative abundance of colour centres is only possible if the EPR measurements are carried out at microwave powers below 0.05 mW. In this regard, difference in acquisition conditions would plausibly explain the discrepancy in the observations between Pinarello et al.¹⁷⁶ and our earlier study⁸⁹.

The photochemistry of H₂-based generation of colour centres has been discussed in detail before (see Sec. 8.1 and Refs. [36,162,170]). When UV irradiation and H₂ are present at the same time, in principle, two types of electron sources become active for colour centre formation: chemisorbed hydrides H⁻ and H⁻ radicals (Fig. 8.8, Eqs. 8.1 and 8.2).

We want to focus now on the relationship between MgO surface sites, which dissociate H₂, and electron traps, among them the most prominent (e⁻)(H⁺) centre. In this context, Pinarello et al. introduced the very useful concepts of “hot sites” and “cold sites” for the characterization of electron traps¹⁷⁶. “Hot sites” are regarded to be active for hydrogen splitting in the dark, whereas “cold sites” are not. The following questions arise:

- Which of the paramagnetic trapped-electron states observed in this study are associated with “hot sites”?
- Is the surface element to be transformed into a (e⁻)(H⁺) centre a hot site?

Irreversibly formed hydride groups act as electron donors when UV light is applied (see Sec. 8.2.1, Fig. 8.2). In addition, H· radicals formed in this step (Eq.8.1) can also act as reducing agent for surface electron traps. The resulting EPR spectrum shows the appearance of essentially two paramagnetic colour centre species (Figs. 8.2 and 8.8). In the first of total five preadsorption cycles (Fig. 8.2), these colour centre species exhibit an almost 1:1 distribution (Fig. 8.2c), which is perfectly in line with the stoichiometric ratio of electrons and H· provided in these experiments (Eq. 8.1). From IR investigations it is known, that irreversible H₂ chemisorption on MgO is, at the temperature applied, saturation limited. Consequently, we expect, that the amount of colour centres directly formed according to the reaction in Eq. 8.1 has also to be limited. Since this is valid for the F_S⁺_A centre (Fig. 8.2, Tab. 8.1), we attribute this signal to electrons trapped at surface structures, which previously hosted the hydride. Accordingly, these electron trap centres belong to the family of “hot sites”. H· radicals that are released in this process then produce the (e⁻)(H⁺) centres. The fact that the latter exhibit a slightly rising abundance upon increasing the number of preadsorption cycles (Fig. 8.2c) suggests that residual H₂ from previous preadsorption cycles becomes active as an additional reducing agent during the UV irradiation of the next cycle. The problems caused by H₂ in high vacuum technique are commonly known – in particular when tiny reservoirs, such as EPR tubes with inner diameters of a few millimetres, have to be evacuated.

Both colour centre species, (e⁻)(H⁺) and F_S⁺_A, which are formed by UV irradiation of irreversibly formed hydrides, are also observed in the EPR spectra of zeroth generation colour centres (see Sec. 8.2.2 and Figs. 8.3 and 8.4), although the ratio is shifted in favour of (e⁻)(H⁺). All possible electron sources according to Eqs. 8.1 to 8.4 – both types of hydrides and H· radicals – become active simultaneously under the prevailing experimental conditions (UV irradiation in the presence of H₂). In the respective IR spectrum (Fig. 8.7b), three new bands are observed in the frequency range of bridged OH. Two of them (i.e., those at 3632 and 3602 cm⁻¹) show no dependence on the H₂ pressure applied during formation of zeroth

generation colour centres and are, therefore, attributed to OH groups that arise from irreversible hydrogen chemisorption and interact with colour centre electrons. On the other hand, the intensities of the IR band at $3528/3532\text{ cm}^{-1}$ and of the EPR signal of the $(e^-)(H^+)$ centre rise continuously with increasing H_2 pressure¹⁷⁹. Therefore, these signals are unambiguously related to the reversible H_2 chemisorption complex. Under UV irradiation the related reversible hydride groups and $H\cdot$ radicals act as electron donors according to Eqs. 8.1 and 8.2. Whether the sites of reversible hydrogen chemisorption are associated with MgO surface arrays with electron trapping capabilities remains an open question at this point. It is, however, important to note that none of the paramagnetic centres described in this study requires the presence of the reversibly formed chemisorption complex for its formation. Furthermore, within the series of alkaline earth metal oxides (MgO, CaO, SrO, BaO), MgO is the only oxide that allows for this type of H_2 activation, whereas the capability of forming $(e^-)(H^+)$ centres is common to all of them¹⁸².

The comparison of the EPR spectra of zeroth- and first-generation colour centres reveals, in contrast to the study of Pinarello et al.¹⁷⁶, a different distribution of electron traps (Fig. 8.4). This means that different electron traps may be selectively chemically addressed (choice of the reducing agent H^- or $H\cdot$). If only $H\cdot$ radicals are provided for colour centre formation on the MgO surface (first generation colour centres), both the characteristic EPR signal of $(e^-)(H^+)$ and the IR band at 3532 cm^{-1} are observed, which provides unambiguous evidence for the interconnection of these features. The appearance of $(e^-)(H^+)$ in the first generation colour centres corroborates the assumption that $H\cdot$ radicals suffice to generate these centres on the surface of MgO. Therefore, the surface arrays hosting the $(e^-)(H^+)$ centres are – according to Fig. 8.2c – unlikely candidates for “hot sites”. The absence of the IR bands at 3632 and 3602 cm^{-1} (Fig. 8.7d) and of the EPR signal for F_s^+ (Figs. 8.3 and 8.4) after the formation of first generation colour centres confirms, again, that these signals correspond to “hot sites” where irreversible heterolytic H_2 splitting occurs.

It is interesting to note that the genesis of all colour centre species discussed here dictates the presence of a hydroxyl proton in their close vicinity. The respective OH group originates either out of heterolytic H_2 splitting in the dark or from $H\cdot$ radical oxidation (Eq. 8.2). In fact, the only surface colour centre, which exhibits a measurable super-hyperfine interaction with a closely spaced hydroxyl proton, is the $(e^-)(H^+)$ centre. The quantitative value of super-hyperfine splitting is determined by the interaction of the magnetic dipoles of (e^-) and (H^+) , and depends on their distance and relative orientation. Obviously, the respective surface defect geometry of the $(e^-)(H^+)$ centre allows for a significant value of the super-hyperfine splitting, whereas that of the F_s^+ centres does not.

8.4. Conclusions

In the present study, we employed methods that involve UV light and different surface hydrogen species as reducing agents to produce colour centres on the surface of polycrystalline MgO. Significant differences in the EPR spectra of the respective colour centres formed point at a distribution of various colour centre species on the surface. Among them, the $(e^-)(H^+)$ centre exhibits outstanding properties. A careful analysis of the saturation behaviour of the EPR transitions shows an enhanced relaxation probability of the $(e^-)(H^+)$ centre as compared to the other F_S^+ species; this is due to the interaction with a closely spaced OH group.

The combination of infrared and EPR spectroscopic results suggests that the MgO sites involved in the irreversible heterolytic chemisorption of hydrogen are transformed into $F_{S^+}^+$ centres by a direct electron transfer from the hydride to the respective $(Mg^{2+})_n$ array, which acts as an electron trap. It also revealed that the surface arrays, where the heterolytic H_2 splitting occurs (the so-called "hot sites") definitely do not host $(e^-)(H^+)$ centres; these centres rather originate from the electron transfer from a mobile $H\cdot$ radical produced by UV-induced oxidation of hydride groups or from the homolytic hydrogen splitting of oxygen anions in corner positions⁵⁴.

9. Chemistry at corners and edges: generation and adsorption of H-atoms on the surface of MgO nanocubes

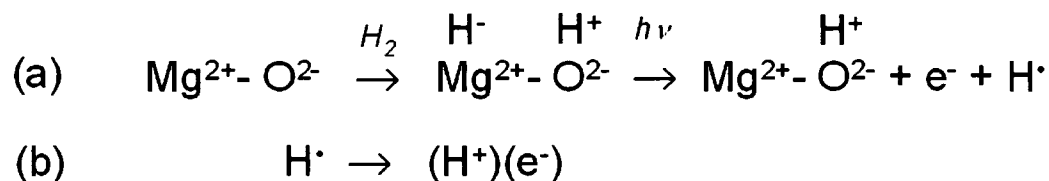
9.1. Introduction

Controlled manipulation of the physical and chemical properties of nanostructures requires correlating their spectroscopic properties and reactivity with specific surface sites. It has been demonstrated that chemical vapour deposition (CVD), in conjunction with subsequent thermal activation allows one to produce cubic MgO nanoparticles with average sizes in the range 3–10 nm⁵¹. Due to the dramatically enhanced concentration of corner and edge sites with distinct spectroscopic properties^{183,185} and reactivity¹⁴⁵, these nanoparticles represent a convenient model system for revealing physical and chemical properties of oxide nanostructures. In conjunction with theoretical modelling, they have been used for studying the surface topographic features, such as corners, kinks and edges^{21,186}. These surface sites and their chemical reactivity have been characterized using a wide arsenal of optical, vibrational and electron paramagnetic resonance (EPR) spectroscopies^{89,184,185}. In this paper we combined selective photo-excitation of the edge and corner sites at MgO nanoparticles surfaces with subsequent exposure to an H₂ atmosphere to achieve controlled modification of the electronic structure and chemical properties of the nanoparticles. On the basis of EPR data and theoretical modelling, we identified new types of surface defects created as a result of photoinduced surface reactions at oxygen corners and described their properties.

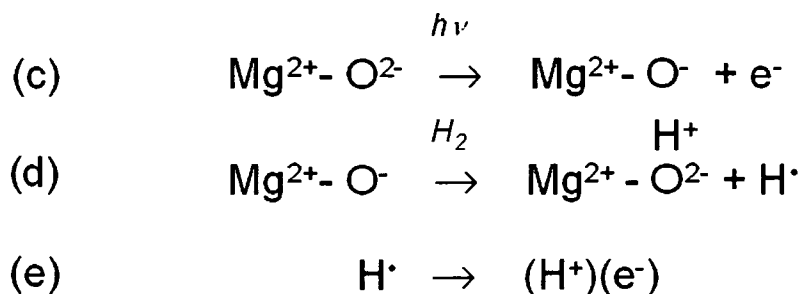
It is well established that the properties of surface excitons, as well as those of electrons and electron holes trapped at different sites at the MgO surface, depend significantly on their local atomic structure^{21,34,38,50,160}. One can exploit this dependence to achieve the site selective chemistry and defect formation at corner and edge sites of MgO nanocubes and to modify the electronic properties of these surface features. Recent experimental and theoretical studies significantly advanced our understanding of the structure and properties of electronic centres at the MgO surface^{21,38,39,160,162,182,187}. It has been demonstrated that anion vacancies on MgO surface terraces are not the only electron trapping sites, as has been assumed in previous studies³⁵. Other, perhaps even more abundant trapping sites, include corner vacancies^{36,176,186} low coordinated Mg cations^{39,160} and surface divacancies^{163,188} and a very general and perhaps conclusive assignment of trapping sites to morphological irregularities such as 4-coordinated cations at steps and edges has been put forward only recently¹⁸⁹.

Another type of deep electron trapping centres is characterized by significant electron spin interaction with the proton of an adjacent OH group^{162,182,185}. These, so-called $(H^+)(e^-)$ centres, have been investigated in several theoretical studies^{38,163,176,187,188} inspired by the recent advances in EPR studies of paramagnetic centres created during UV irradiation of MgO in a hydrogen atmosphere^{162,182,187}. The two reaction channels for the formation of $(H^+)(e^-)$ centres¹⁸⁵ are (see also Scheme 1).

Heterolytic H₂ activation pathway



Homolytic H₂ activation pathway



Scheme 1: Heterolytic and homolytic H₂ activation pathways for the photo-generation of H \cdot radicals and the formation of $(H^+)(e^-)$ centres.

(i) heterolytic H₂ splitting in the dark¹⁹⁰ followed by UV-induced hydride oxidation (Scheme 1a) and then trapping of the electrons and H \cdot radical adsorption (Scheme 1b) and (ii) UV induced O \cdot formation (Scheme 1c) followed by homolytic H₂ splitting in the dark (Scheme 1d) plus H \cdot radical adsorption (Scheme 1e). The precise assignment of the reaction pathways, including the initial sites of the H₂ splitting, and characterization of the reaction products is a very complex task.

We have recently demonstrated that irradiation of MgO powders with UV light in the energy range of 4.5–6.2 eV results exclusively in the formation of 3-coordinated O \cdot radicals that represent trapped hole centres⁵³. The almost ideal cubic structure of MgO nano-particles and high reactivity of corner O \cdot species make them well-defined surface reactants. In the present work, we use this to selectively induce and investigate one specific defect formation pathway

represented in Scheme 1c–e. The exposure of MgO nanocubes with pre-formed corner O^- radicals to H_2 gas causes homolytic splitting of H_2 at these O^- sites^{54,89} and the production of $H\cdot$ atoms. As a result of $H\cdot$ atom adsorption on the MgO surface new surface defects are formed. Since they optically absorb in visible light range they are considered as surface colour centres. Although the heterolytic dissociation of H_2 , shown in Scheme 1a, at other surface sites cannot be excluded, it does not contribute to the colour centre formation on its own. Thus, a complex chemistry associated with the colour centre formation process¹⁸⁵ can be greatly simplified. Since the local atomic structure and the nature of O^- radicals, as well as the nature of their chemical reaction with H_2 , are known (Scheme 1d), this limits the number of possible reaction products and permits a more reliable characterization of their atomic structure, electronic properties and location at the surface using theoretical modelling. Using *ab initio* embedded cluster calculations we found that the colour centres are most likely associated with *two* rather than one proton and can be represented as $(H^+)(e^-)(H^+)$ entities oriented along nanocube edges. We also demonstrate that combinations of such entities may form 1-dimensional structures with novel functionalities. The formation of these defects eliminates active O^- sites and is thus responsible for the modification of the surface electronic structure and chemical properties.

9.2. Theoretical method

The experimental results obtained in this work were corroborated by theoretical *ab initio* calculations carried out using an embedded cluster approach. This method is implemented in the computer code GUESS (Gaussians Used for Embedded Systems Studies) and combines a quantum-mechanical treatment of a “region of interest” with a classical shell model treatment of the rest of a system. The details of this approach have been described elsewhere^{160,186}. Briefly, an MgO powder particle is represented using a cubic nano-cluster of $20 \times 20 \times 20$ ions. The nano-cluster is divided into two regions. Region I, in the form of a segment of a sphere centred at an oxygen-terminated corner site, includes a quantum mechanical (QM) cluster, a classically treated part and an interface between them. The remaining part of the nano-cluster forms Region II, which is described classically. The total energy of the system is optimised with respect to the coordinates of all centres in Region I; all centres in Region II remain fixed at their ideal MgO bulk positions in the course of the calculations. The energy minimization is carried out automatically until the change in the total energy, displacements of atoms, and the forces acting on these atoms become less than 10^{-5} eV, 0.0003 Å, and $0.003 \text{ eV}\cdot\text{Å}^{-1}$, respectively. The “region of interest” in this work includes an oxygen-terminated corner, formed by three planes equivalent to an (001) surface terrace,

together with an edge of the nano-cluster. Hence, we chose a cuboidal QM cluster of $2 \times 2 \times 6$ ions $\text{Mg}_{12}\text{O}_{12}\text{Mg}^*_6$, where Mg^* denote interface ions. Pople's standard 6-31G basis set was used for Mg and O ions of the QM cluster and a cc-pVDZ basis set¹⁹¹ was used for hydrogen atoms. The interface Mg^* atoms were represented using an Effective Core Pseudo-potential (ECP)¹⁹². The quantum-mechanical contributions to the total energy were calculated using the Gaussian 03 package for *ab initio* calculations of molecules¹⁹¹ and hybrid density functional B3LYP. The latter combines Becke's exchange functional with 20% of exact exchange interaction¹⁹³ with a correlation functional by Lee, Yang and Parr¹⁹⁴. The excitation energies were calculated by Time Dependent Density Functional Theory (TD-DFT). For comparison, we also report the properties of $(\text{H}^+)(\text{e}^-)$ centres formed via adsorption of H atoms at MgO terraces. The adsorption energy was calculated earlier in Ref. 38; here we report the magnetic properties and optical absorption found for these centres. For consistency we use cc-pVDZ basis on H in all our calculations; all other details remain the same as in Ref. 38.

9.3. Results

9.3.1. Experimental data

Dehydroxylated MgO nanocubes were exposed to monochromatic UV light of 5.4 eV (237 nm, $0.35 \text{ mW}\cdot\text{cm}^{-2}$) and at $P < 10^{-6}$ mbar. As a result surface trapped hole and electron centres were generated as reported previously^{89,53} (Scheme 1c).

This corresponds to a photoinduced ionisation process of low coordinated (LC) oxygen ions. The released electrons give rise to an EPR signal (shown in Fig. 9.1a), which is consistent with creation of trapped-electron states¹⁹⁵ on the MgO surface. Analysis of the microwave power dependence of the EPR signal allowed us to identify two types of electron centres,

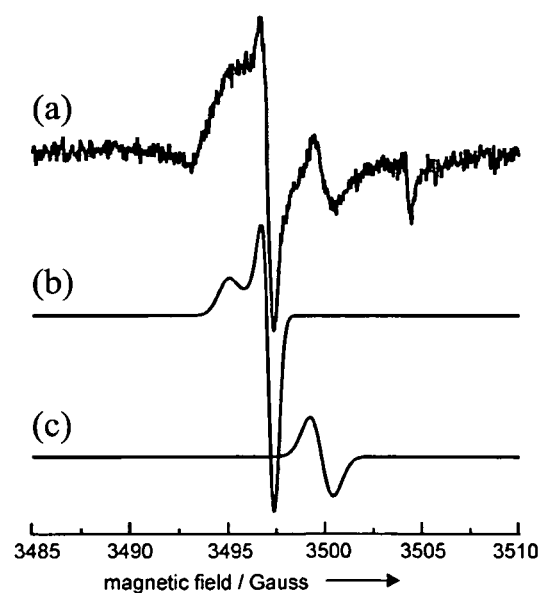


Fig. 9.1: (a) EPR spectrum of electron centres formed after UV irradiation of MgO nanocubes. Traces (b) and (c) are simulated spectra of the two colour centre species F(1) and F(2) respectively.

denoted here as F(1) and F(2). The simulated spectra of F(1) and F(2) are shown in Figs. 9.1b and 9.1c respectively, and the g-tensor components are given in Tab. 9.1.

Electron centre	$g_{11}=g_{22}$	g_{33}	^1H Hyperfine constants, Gauss
			A_{iso}
F(1)	2.0000	2.0013	—
F(2)	1.9985	1.9985	—
$(\text{H}^+)(\text{e}^-)$	1.9998	2.0016	1.5 ± 0.1

Tab. 9.1: Measured g-tensor components and ^1H hyperfine coupling constants of electron centres on the surface of MgO nanocubes.

The surface nature of the trapped electron centres has been verified by the complete disappearance of their EPR signal after reaction with O_2^{195} . However, the assignment of the electron centre species to specific surface structures has so far remained speculative. The electron centres F(1) and F(2) can be loosely divided into two groups. In an earlier study¹⁹⁵ we have shown that the ionisation energy of most of these centres is in the range from 2.0 eV to 2.5 eV. For this reason, they can be regarded as *shallow electron traps*. At the same time some of these electron centres are not ionised by photons with energies as large as 4 eV¹⁹⁵, and, therefore, can be regarded as *deep electron traps*. The situation is more straightforward with the trapped holes. Although 4-coordinated oxygen ions are excited with UV light of 5.4 eV energy, both experimental^{53,54} and theoretical studies^{34,160} indicate that trapped hole centres formed thereafter are located at 3-coordinated oxygen sites on the surface, e.g. kinks and corners. To summarize, prior to the admission of molecular hydrogen, the system was brought into a metastable state characterized by the well-defined 3-coordinated hole centres and electrons in deep and shallow surface traps.

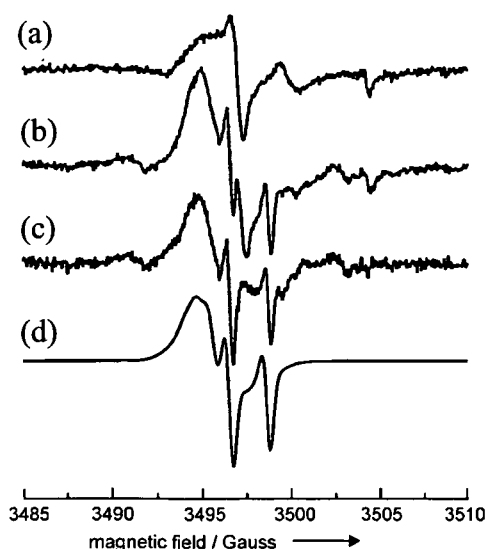


Fig. 9.2: EPR spectra of electron centres generated by UV-irradiation (a) and generated after the reaction of UV pre-irradiated samples with H_2 (b). (c) Difference between spectra (b) and (a). (d) Simulated trace of spectrum (c).

Admission of molecular hydrogen into the EPR cell causes the complete disappearance of the hole centre EPR signal. At the same time, new spectral features appear in the magnetic field range where colour centres usually resonate with $g \sim g_e$ ^{39,162,187} (Fig. 9.2b). The characteristic signature of the underlying signal is associated with $(H^+)(e^-)$ centres^{39,162,182,187}, which are different from the previously introduced F(1) and F(2) (Tab. 9.1). The spectrum is dominated by a super-hyperfine splitting with a coupling constant A_{iso} of 1.5 Gauss due to the interaction of the electron spin with the nuclear magnetic moment of a proton in its close vicinity. The difference between the spectra taken before (Fig. 9.2a) and after H_2 admission (Fig. 9.2b) is shown in Fig. 9.2c. Simulation of this spectrum reveals that >80% of the trapped electrons constitute $(H^+)(e^-)$ centres*. With EPR spectroscopy we did not detect any changes in shape and intensity of the F(1) and F(2) electron centre signals that might have resulted from the contact of the sample surface with H_2 (see Fig. 9.2b).

As shown by IR spectroscopy, hole centres react with H_2 and induce the homolytic H_2 splitting (Scheme 1d)^{54,89}. The hole centre becomes hydroxylated, i.e. one of the $H\cdot$ atoms (H_{II}) binds to the corner O^- and converts it effectively from a 3-coordinated to a 4-coordinated anion. The other $H\cdot$ atom (H_I) is released; it acts as a reducing agent on the surface and forms a colour centre as shown in Scheme 1e. Previous theoretical studies indicate that $H\cdot$ radicals remain intact on surface terraces and only weakly interact with terrace sites³⁸. However, they dissociate into a proton and an electron and form $(H^+)(e^-)$ centres at lattice sites with reduced coordination. Possible structures, such as reverse corners and mono-atomic steps³⁸ and sites in the vicinity of divacancies^{163,188}, have been put forward. In the case of MgO nanocubes produced by CVD, edges are the most abundant type of low-coordinated lattice sites^{21,51}. In line with a recent assignment of these centres to 4-coordinated cations at step edges¹⁸⁹ we, therefore, propose that the newly formed signal of $(H^+)(e^-)$ centres (Fig. 9.2c) is associated with $H\cdot$ atom adsorbed at the edge sites of MgO nanocubes in close vicinity to the 3-coordinated OH^- (OH^-_{3C}) groups, which were formed during the homolytic H_2 splitting.

9.3.2. Theoretical model

To test the proposed defect model, we have calculated the atomic and electronic structures of several paramagnetic centres that can be formed upon exposure of 3-coordinated O^- hole centres to H_2 gas and subsequent $H\cdot$ radical trapping. First, we established that the reaction of an O^-_{3C} ion with a hydrogen molecule indeed results in the homolytic dissociation of H_2

* Less than 20% abundance stems from colour centre species, which were reported in Ref. 185. These species do not contain any measurable hyperfine splitting due to electron proton interaction.

and formation of a 3-coordinated OH^- group and an $\text{H}\cdot$ atom. This reaction has no barrier and the total energy gain is close to 0.5 eV. The $\text{OH}^-_{3\text{C}}$ group formed in this reaction is oriented along [111] symmetry direction of the MgO lattice.

To investigate the fate of the $\text{H}\cdot$ radical released in H_2 splitting, we considered its reaction with several oxygen lattice sites. On edges, the nearest and the next-nearest 4-coordinated oxygen sites with respect to the $\text{OH}^-_{3\text{C}}$ group (Figs. 9.3a and 9.3b, respectively) will be denoted in this paper as $\text{O}_{4\text{C},\text{n}}$ and $\text{O}_{4\text{C},\text{nn}}$ sites and $\text{O}_{3\text{C},\text{inf}}$ stands for a distant 3-coordinated oxygen site (Fig. 9.3c). In addition, we also considered distant $\text{O}_{5\text{C},\text{inf}}$ site at the surface terrace (Fig. 9.3d). Calculated formation energies, ionisation potentials, and energies of the most intensive transitions are collected in Tab. 9.2. These data show that the electronic properties of the $(\text{H}^+)(\text{e}^-)$ centre strongly depend on the position and the distance from the original $\text{O}^-_{3\text{C}}$ site.

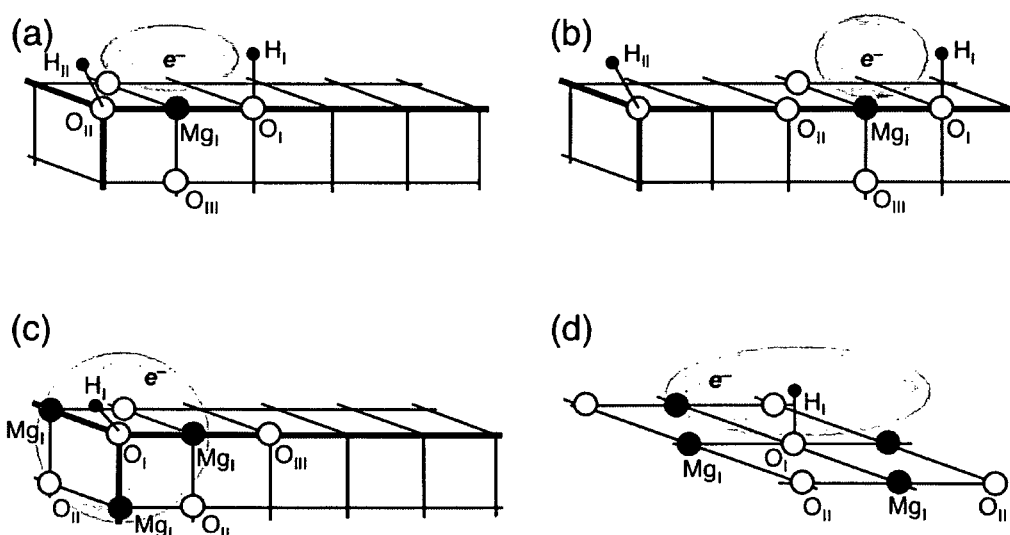


Fig. 9.3: In the course of the homolytic H_2 splitting process (Scheme 1c–e), one of the $\text{H}\cdot$ atoms (H_{II}) binds to the corner O^- and converts it effectively into a 4-coordinated anion. The other $\text{H}\cdot$ atom (H_{I}) is released and adsorbs at certain surface sites to form $(\text{H}^+)(\text{e}^-)$ centres. Discussed configurations of $(\text{H}^+)(\text{e}^-)$ centres are (a) the $(\text{H}_{\text{I}}^+)(\text{e}^-)(\text{H}_{\text{II}}^+)$ configuration with H_{I} adsorbed at a $\text{O}_{4\text{C},\text{n}}$ site, (b) $(\text{H}_{\text{I}}^+)(\text{e}^-)\dots(\text{H}_{\text{II}}^+)$ configuration with H_{I} adsorbed at a $\text{O}_{4\text{C},\text{nn}}$ site, (c) H_{I} adsorbed at a distant 3-coordinated oxygen site ($\text{O}_{3\text{C},\text{inf}}$), (d) H_{I} adsorbed at a distant 5-coordinated oxygen site ($\text{O}_{5\text{C},\text{inf}}$).

First, we compare the stability of different configurations of the $(\text{H}^+)(\text{e}^-)$ centres. It is seen from Tab. 9.2 that the highest adsorption energy of an $\text{H}\cdot$ radical, i.e. formation energy of an $(\text{H}^+)(\text{e}^-)$ centre, is obtained for the 3-coordinated oxygen site $\text{O}_{3\text{C},\text{inf}}$ shown in (Fig. 9.3c). Furthermore, the adsorption energies for $\text{H}\cdot$ at the 4-coordinated edge sites $\text{O}_{4\text{C},\text{n}}$ and $\text{O}_{4\text{C},\text{nn}}$ close to the H_2 splitting site are sufficiently high to expect stability for $(\text{H}^+)(\text{e}^-)$ centres at these

positions. However, H· radicals only physisorb at 5-coordinated sites $O_{5C,inf}$ (Fig. 9.3d) with an adsorption energy of 0.46 eV. Thus, it is expected that H· will travel across the terraces until they encounter lower coordinated oxygen sites, e.g. 4-coordinated sites (4C), to generate a $(H^+)(e^-)$ centre there*.

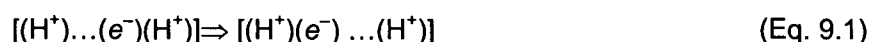
Site	Figure	Adsorption energy, eV	Ionisation potential, eV	Excitation energies (in eV) and oscillator strengths		
				$E_1 (f_1)$	$E_2 (f_2)$	$E_3 (f_3)$
$O_{4C,n}$	Fig. 3(a)	1.52	5.85	1.71 (0.23)	2.44 (0.16)	
$O_{4C,nn}$	Fig. 3(b)	1.32	4.84	0.53 (0.09)	1.92 (0.12)	2.32 (0.15)
$O_{3C,inf}$	Fig. 3(c)	2.10	2.63	1.21 (0.15)	1.45 (0.23)	1.53 (0.12)
$O_{5C,inf}$	Fig. 3(d)	0.46*	2.40	1.82 (0.24)×2		

* Value of 0.5 eV has been reported earlier in Ref.38.

Tab. 9.2: H· atom adsorption energies and ionisation potentials, excitation energies E and oscillator strengths f calculated for different types of $(H^+)(e^-)$ centres on MgO surface sites.

There is a strong dependence of the IP on the distance of the $(H^+)(e^-)$ centre from the H_2 splitting site where an OH^-_{3C} group has been formed. Clearly, the positive electrostatic potential of the OH^-_{3C} group contributes to the stabilization of the trapped electron; this effect is the strongest for $O_{4C,n}$ and $O_{4C,nn}$ sites and decreases rapidly with increasing distance between the H_2 splitting site and a 4C adsorption site of the H· radical.

The calculated excitation energies and the details of the electronic structure of the excited states of the trapped electrons also depend on the particular atomic structure of the defect. However, all of the centres absorb light in the visible range between approximately 1.3 eV and 2.4 eV in agreement with the experimental data^{36,183}. The energies of the main transitions for the $O_{4C,n}$ and $O_{4C,nn}$ are almost identical (two bands at 1.7–1.9 eV and 2.3–2.4 eV) which reflects the similarity of the electron density distribution for these centres. In addition, the $4C_{nn}$ centre also exhibits a low-energy transition at 0.5 eV. This transition corresponds to the electron transfer from a vicinity of the 4-coordinated OH^- group at the next nearest site to the vicinity of the OH^-_{3C} group (Eq. 9.1).



We note that the $O_{5C,inf}$ centre has two degenerate excited states with excitation energies at 1.8 eV and, therefore, can also be considered as a colour centre.

* However, one might expect that $O_{5C,inf}$ configuration of $(H^+)(e^-)$ centre can be stable at low temperatures. In that case it should contribute to the colouring of the MgO sample (see Tab. 9.2).

Site	Figure	Isotropic hyperfine constants A_{iso} , Gauss						g-tensor components		
		$^1\text{H}_I$	$^1\text{H}_{II}$	$^{25}\text{Mg}_I$	$^{17}\text{O}_I$	$^{17}\text{O}_{II}$	$^{17}\text{O}_{III}$	g_{11}	g_{22}	g_{33}
$\text{O}_{4\text{C},n}$	Fig. 3a	-2.7	-0.7	-34.7	-34.9	-23.3	-9.4	1.9999	2.0006	2.0020
$\text{O}_{4\text{C},nn}$	Fig. 3b	-2.7	0.0	-25.5	-48.8	-16.6	-9.4	1.9995	2.0006	2.0020
$\text{O}_{3\text{C},inf}$	Fig. 3c	-0.8		-8.1		-9.9		2.0004	2.0008	2.0030
				-11.9	-61.8	-9.2	-7.0			
				-11.7		-9.2				
$\text{O}_{5\text{C},inf}$	Fig. 3d	2.4		-4.6	-77.3	-12.6		1.9993	1.9994	2.0013

Tab. 9.3: Calculated isotropic parts of the hyperfine interaction of unpaired electrons with ^1H , ^{25}Mg , and ^{17}O calculated for different types of $(\text{H}^+)(e^-)$ centres on MgO surface sites.

Isotropic parts of the hyperfine interactions with ^1H , ^{25}Mg , and ^{17}O as well as components of g-tensors for these $(\text{H}^+)(e^-)$ centres are summarized in Tab. 9.3. Taking into account the basis set and method limitations, the principal values of the g-tensor are in reasonable agreement with the experimental data (Tab. 9.1). In particular, the hyperfine constants calculated for the centres $\text{O}_{4\text{C},nn}$ and $\text{O}_{3\text{C},inf}$ are consistent with experimentally observed values of 1.5 Gauss for ^1H , as well as 11 Gauss for ^{25}Mg and 51 G for ^{17}O which were reported for the $(\text{H}^+)(e^-)$ by E. Giamello and coworkers^{39,162,187,189}. The $(\text{H}^+)(e^-)$ centres at the $\text{O}_{4\text{C},n}$ and $\text{O}_{4\text{C},nn}$ sites can be characterized as $(\text{H}_{II}^+)(e^-)(\text{H}_I^+)$ and $(\text{H}_{II}^+) \dots (e^-)(\text{H}_I^+)$ configurations respectively. The spin density is mostly associated with H_I but it is polarized toward the 3-coordinated OH^- group, which contains H_{II} (Fig. 9.3). As a result the A_{iso} for H_I is smaller than for other $(\text{H}^+)(e^-)$ centres and A_{iso} for H_{II} is too small to be detected confidently. The g-tensor observed for $(\text{H}^+)(e^-)$ centres is apparently axial but is expected to have lower unresolved rhombic symmetry. The g values (see Tab. 9.1) are well reproduced in all theoretically considered models (Tab. 9.3).

9.4. Discussion

In this study we used UV light to generate site-specifically O^- hole centres at 3-coordinated corner oxygen sites on MgO nanocubes. These sites hydroxylate when molecular hydrogen is added. Adsorption of the resulting $\text{H}\cdot$ atom is associated with the formation of a $(\text{H}^+)(e^-)$ type colour centre. We propose a reaction pathway, involving hydroxylation of corner anions and adsorption of $\text{H}\cdot$ atoms at adjacent edge anions, which is supported by *ab initio* calculations. The $\text{O}_{4\text{C},nn}$ site is more favourable than a remote $\text{O}_{3\text{C},inf}$ site because of the following two arguments: first it is adjacent to the H_2 splitting site and second, the optical

absorption data are in much better agreement with the experimentally observed values¹⁸³. Furthermore, we show that the positive electrostatic potential of the corner hydroxyl significantly contributes to stabilization of these centres. The transformation of corner O^- centres into the $(H^+)(e^-)(H^+)$ type centres prevents their recombination with F(1) and F(2) centres and hence significantly alters the electronic structure of nano-clusters by introducing shallow electron traps.

The mechanisms of colour centre formation by the UV irradiation of MgO surfaces with pre-adsorbed hydrogen, or during UV irradiation in the presence of H_2 involve heterolytic H_2 activation pathways^{21,185,190}. In fact, the corresponding surface dissociation sites are still subject to speculation¹⁹⁶. Therefore, the approach, where the sites of H_2 homolytic dissociation are well-defined, represents a step forward in the structural determination of electron trapping sites on the MgO surface.

The detailed analysis of $(H^+)(e^-)$ centres at high surface-area MgO with isotopically labelled ^{17}O , has recently been reported by M. Chiesa et al.¹⁸⁷. By determination of the ^{17}O hyperfine coupling constants from the spectra, and with the support of quantum chemical calculations, the authors concluded that the adsorption of an $H\cdot$ atom and the formation of the most abundant $(H^+)(e^-)$ centres take place at the edges of the MgO plate-like structures²¹. The results of our calculations suggest that alternative configurations of $(H^+)(e^-)$ centres at $O_{3C,inf}$ and $O_{4C,m}$ sites are also consistent with the experimental data (see, for example, Ref. 187).

We should note that the shape of electron centre signals F(1) and F(2) generated during UV excitation (see also Tab. 9.1) is not affected by exposure to H_2^* . The absence of a hyperfine splitting (hfs) effect does not necessarily mean that these centres must be completely isolated from surface hydroxyl groups, since small values for the hfs constant as computed for trapped electron interacting with the proton of a 3-coordinated OH^- group (Figs 9.3a, 9.3b and Tab. 9.3) and for the interaction of $H\cdot$ radicals with the (100) surface of MgO^{197} are not resolvable in the cw-EPR powder spectrum^{**}. In agreement with earlier studies^{35,189}, both experimental and theoretical results provided in this study clearly demonstrate that $H\cdot$ radicals are sufficient for the generation of $(H^+)(e^-)$ centres on the surface of MgO^{185} . The balance of energies required for the formation of $(H^+)(e^-)$ centres was described in Ref. 38. Since the H_2 dissociation sites are positively charged with respect to the lattice, the resulting

* A smaller fraction of colour centres with no measurable hyperfine splitting was also observed after reaction of H_2 with O_{3C}^- (Tab. 9.1).

** Only hyperfine splitting effects with constants larger than 0.7 Gauss can be effectively resolved in cw-EPR signals with a linewidth of 0.5 Gauss, which is typically measured for colour centre signals on CVD MgO powders.

colour centres can be viewed as $(H^+)(e^-)\dots(H^+)$ entities that retain the positive charge and maintain a balance of energies favourable for formation of other $(H^+)(e^-)$ centres. The distance between $(H^+)(e^-)$ and (H^+) components and their properties should depend on the concentration of hydrogen species (both H_2 molecules and $H\cdot$ radicals) and the size and morphology of MgO particles. For a sufficiently high concentration of $H\cdot$ radicals, one can envisage, that structures similar to $(H^+)(e^-)(H^+)$ configuration, such as that found for $4C_n$ site shown in Fig. 9.3a, can be generated along mono-atomic steps or edges in the form of $(H^+)(e^-)(H^+)(e^-)(H^+)\dots(H^+)(e^-)(H^+)$ chains. In other words, edges effectively direct adsorption of $H\cdot$ radicals and accommodate $(H^+)(e^-)(H^+)$ -like entities. The latter represent 1D electrone-like structures where electrons play a role of anions^{198,199}. Alternatively, if the distance between $(H^+)(e^-)$ and (H^+) components is a few lattice constants, a low-energy optical absorption band is expected due to the charge-transfer transitions (Eq. 9.1) similar to the situation of the colour centre at $4C_{nn}$ site shown in Fig. 9.3b. Optical transitions of this character include inter- and intra-chain transitions in polymers²⁰⁰ and inter-cage transitions in an electron-rich nano-porous oxide^{201,202}. The broad absorption band reported recently for hydroxylated MgO surfaces²⁰³ could also be explained by such a phenomenon.

One can look at these results also from a different perspective: exposure of the UV-irradiated surface to molecular hydrogen eliminates active O^- sites and stabilizes the F(1) and F(2) centre because their recombination with holes is now prevented. The chemical modification of MgO nanocubes described above represents an example of electronic structure engineering where occupied as well as unoccupied electronic states appear in the band gap of MgO due to F(1), F(2) and $(H^+)(e^-)(H^+)$ centres. The concentration of these states can be regulated by the size and morphology of the MgO structures, the UV energy and fluence and by the concentration of $H\cdot$ radicals available. This approach is expected to be generic for materials with strong OH^- bonds and can be used to modify their properties.

CHARGE TRAPPING IN SEMICONDUCTORS AND INSULATORS – A COMPARATIVE STUDY

Light induced charge separation was studied in-situ by electron paramagnetic resonance spectroscopy on MgO and TiO₂ nanocrystals. For both materials, polychromatic excitation ($1.2 < E < 6.2$ eV) produces well-separated electron and hole centres. On MgO, where only surface features such as 3- and 4-coordinated anions are excited with energies < 6.2 eV, very different time evolutions were observed for the EPR signals of trapped electron and hole centres which is explained by secondary reactions stimulated by the low energy part of the radiation spectrum. As in the case of MgO, in TiO₂ supra band gap excitation ($E > 3.2$ eV) generates hole centres, which form O⁻ radicals when the holes get trapped at oxygen anions. Only a limited fraction of trapped electrons, however, is localized as Ti³⁺ states, the majority remains in the conduction band. Different to MgO, this state of charge separation can be kept constant only at temperatures below 200 K, because of thermally driven charge carrier annihilation. The performance of dynamic excitation experiments under high-vacuum conditions and low temperatures allows one to track the process of light induced charge separation on a time scale of seconds and minutes.

10. Trapping of photogenerated charges in oxide nanoparticles

10.1. Introduction

Understanding of charge trapping effects on oxide surfaces is fundamentally important for a variety of technological applications ranging from photocatalysis^{9,10,80} to solid state electronics^{155,156,204}. In photocatalysis, charge trapping extends the lifetime of photogenerated electrons and holes and decreases their recombination rate. This is a desired effect because it enhances the efficiency of the photocatalyst. High-k dielectrics such as ZrO₂ and HfO₂ represent another case where charge trapping determines the performance of oxide materials¹⁵⁴. Conventionally, current-voltage and capacitance-voltage measurements are employed to characterize the reliability of the high-k gates. However, these techniques fall short in assessing the nature and exact function of charge traps at the atomic level where basic knowledge and control is needed. As a third example, surface sites, which stabilize electrons and holes are generally associated with defects and play a major role in surface chemistry. Thus, research in the field of heterogeneous catalysis concentrates on the catalytic activity of reactive surface sites^{7,19,158} and methods for their visualization by molecular spectroscopy techniques are needed.

Surfaces and defects associated with the surface have a major impact on the physical properties of polycrystals, when they get a few nanometers in size since the surface-to-volume ratio is large. Besides their potential for technological applications, this makes nanometer-sized particles an attractive choice for surface science investigations on particulate matter. Recently, we have shown that nanoparticles obtained by chemical vapour deposition represent well-suited model systems for the characterization of surface defects^{51,145}. This technique for the production of non-equilibrium solids provides crystals with a narrow size distribution and, in some cases, even leads to particles of well-defined morphology.

Light absorption by solids produces excited states, e.g., excitons, free charge carriers and phonons. Incomplete recombination of the excited state is associated with the radiation-stimulated formation of defects in semiconductors and insulators. If light of moderate photon energies below the impact displacement energy threshold is used, these defects correspond to separated charges, such as localized electron and holes.

The objective of this investigation is to demonstrate that light induced charge separation and trapping effects, which occur on oxide nanoparticles, can be elucidated by electron paramagnetic resonance (EPR) spectroscopy. In oxide materials, holes are generally trapped by lattice anions to form paramagnetic O^{\cdot} radicals with a well-characterized EPR signature⁹⁸. As far as the local structure of the paramagnetic state is concerned, EPR spectroscopy is exceptionally valuable. Information about crystal structure and local symmetry around the spin centre can be extracted from the g-components of the respective EPR signals¹⁷⁸. Furthermore, it will be shown that when high vacuum conditions and low temperatures ($T < 100$ K) are applied, the dynamics of charge separation and charge trapping processes become experimentally accessible. The evolution of EPR signals of trapped holes and electrons can be tracked on a time scale of seconds to minutes during excitation using light sources with power densities in the $mW \cdot cm^{-2}$ range^{63,112}.

Two types of oxide materials with fundamentally different properties²⁰⁵ will be compared: i) MgO which is an insulator with a band gap of 7.8 eV and a fully ionic compound composed of Mg^{2+} and O^{2-} ions and ii) TiO_2 anatase as a semiconductor with a band gap of 3.2 eV representing an intermediate between fully ionic (Ti^{4+} and O^{2-}) and fully covalent. For both cases, it will be demonstrated that hole centres preferentially localize at oxygen anions, whereas the nature of the electron trapping site results from the electronic structure of the oxide material.

10.2. Results and Discussion

Chemical vapour deposition allows the production of nanometer-sized particles with narrow size distribution⁵¹. The transmission electron micrographs in Fig. 10.1 characterize the product powders after thermal activation under high-vacuum conditions. After annealing at 1170 K, the MgO particles exhibit cubic shape with edge lengths between 5-10 nm. The TiO_2 particles with an essentially undefined morphology, are slightly higher in particle size in the range between 10-20 nm. For TiO_2 activation, temperatures not higher than 870 K were selected. Under these conditions, only reflexes consistent with the anatase structure were measured by X-ray diffraction.

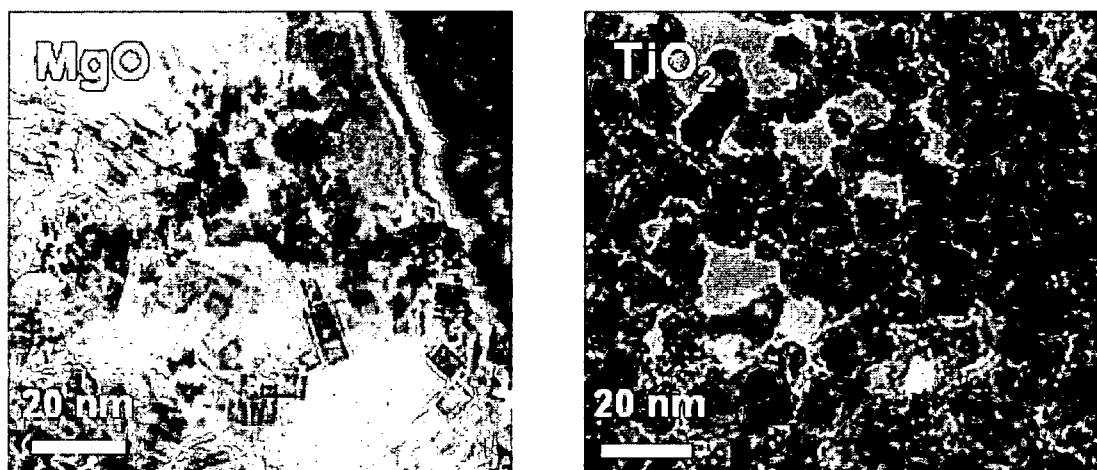


Fig. 10.1: Transmission electron micrographs of MgO nanoparticles after thermal treatment at 1170 K (left image) and anatase TiO₂ particles after treatment at 870 K (right image).

10.2.1. Optical excitation and charge separation

The UV diffuse reflectance spectra in Fig. 10.2 represent the optical absorption properties of MgO (Fig. 10.2a) and TiO₂ (Fig. 10.2b)* and illustrate the profound differences between the electronic structures of these two oxide materials²⁰⁵. MgO, an insulator with an intrinsic band gap of 7.8 eV, shows essentially two absorption bands below 6.2 eV*. These absorption features are only observable on highly dispersed MgO materials, provided the surface is sufficiently dehydroxylated¹⁸⁴. A correlation between the excitation energies and the coordination number of the oxygen anions in the MgO surface has been put forth on the basis of experimental studies^{50,51} and theoretical computations¹⁶⁰: the excitation energies range from 7.8 eV in the bulk (6-coordinated O²⁻), 6.3 eV for 5-coordinated anion sites in (100) planes, 5.4 eV for 4-coordinated anion sites and 4.6 eV for 3-coordinated anion sites. In line with this correlation, the optical absorption features at around 5.4 eV and 4.6 eV (Fig. 10.2a) are attributed to the electronic excitation of 4-coordinated anions located in edges and 3-coordinated anions in corner and kink positions of MgO nanocubes (Fig. 10.1), respectively. Whereas on MgO only surface states are addressed with light energies below the vacuum UV ($E < 6.2$ eV), the absorption spectrum of semiconducting TiO₂ particles reveals total optical absorption above the band gap onset at 3.2 eV corresponding to electron transitions from the valence to the conduction band.

* The spectra were acquired in the presence of 5 mbar O₂ in order to exclude luminescence effects.

* This energy corresponds to a wavelength of 200 nm, the minimum wavelength for studies in non-evacuated systems, where atmospheric oxygen is present between light source, sample cell and detector.

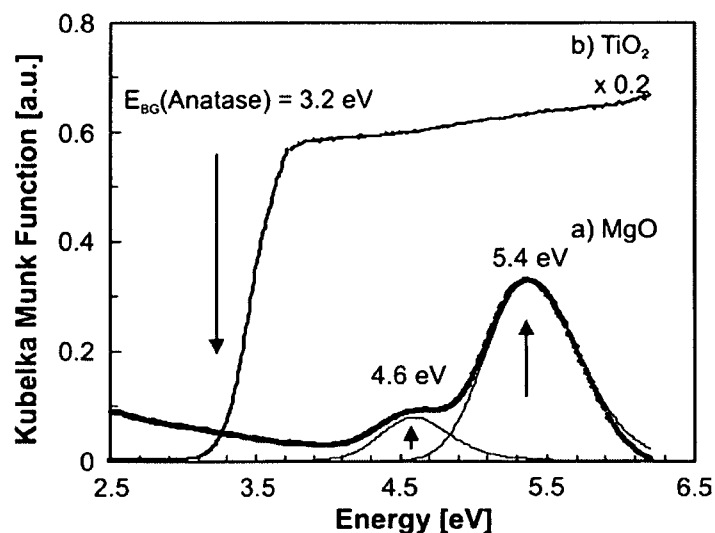


Fig. 10.2: UV/Vis diffuse reflectance curves for (a) MgO and (b) TiO₂ nanoparticles as characterized by Fig. 10.1. The spectra were acquired in the presence of 5 mbar O₂ in order to omit luminescence effects.

When UV light in the mW·cm⁻² range is used, the respective light-induced transitions can be followed by the decomposition of the excited states into separated charges. These processes were studied with EPR spectroscopy at 90 K. Before UV exposure no paramagnetic signals were observed on both types of samples. However, after UV exposure EPR signals with g values above (lower magnetic field) and below the free spin value $g_e = 2.0023$ (higher magnetic field) were measured.

In MgO an axially symmetric signal with $g_{\perp} = 2.036$ and $g_{\parallel} = 2.002$ originates from hole states localized at oxygen anions, i.e., O⁻ radicals (Fig. 10.3a)^{89,98}. On the basis of wavelength selected excitation experiments, we have shown that exclusively 3-coordinated surface ions in corner and kink positions are involved in this type of hole trapping⁵³. The electrons released during O⁻ generation



are trapped somewhere on the MgO surface giving a characteristic EPR signal around the free spin value ($g_e = 2.0023$). On MgO, these centres are generally regarded as surface colour centres, F_s^+ , since they give rise to typical excitations in the visible region of the spectrum¹⁸⁵. Their surface nature is evidenced by their complete conversion to superoxide anion species after reaction with molecular oxygen at 90 K⁵⁴.

Oxygen vacancies have long been considered as the most abundant surface electron trapping sites²⁰⁵. However, the discussion on the nature of surface electron traps has

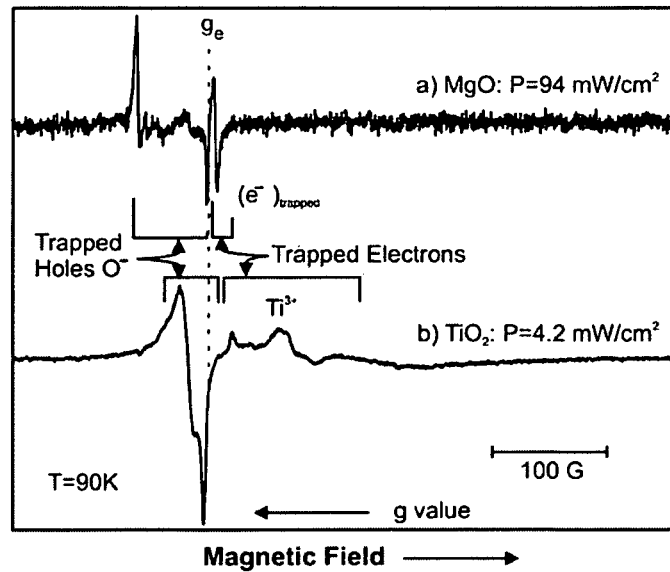


Fig. 10.3: EPR spectra of MgO (a) and TiO₂ (b) nanoparticles after 20 minutes of UV exposure at 90 K.

recently been extended to other structural defects¹⁶³. The ionisation energies for these electrons trapped after light-induced charge separation were determined to be about 2 eV, which is significantly below the value expected for electrons trapped in anion vacancies at surface terrace sites¹⁸⁶. This suggests that other structural defects, such as Mg²⁺/O²⁻ divacancies, Mg corner and kink sites, etc, adopt the electron out of Eq. 10.1 and then exhibit ionisation energies of about 1-2 eV^{34,37,38,186}.

A comparable excitation experiment performed on TiO₂ leads to O⁻ radicals with $g_{\perp} = 2.012$ and $g_{\parallel} = 2.0046$ (Fig. 10.3b). In addition, at higher magnetic fields axially symmetric signals with $g_{\perp} = 1.964/ g_{\parallel} = 1.950$ and $g_{\perp} = 1.990/ g_{\parallel} = 1.960$ are measured. These signatures are reported for paramagnetic Ti³⁺ cations in anatase crystals containing one unpaired electron in their d shell¹⁰⁷,



The integral intensity of Ti³⁺ centres, i.e., the number of trapped and localized electrons, never exceeds 10% of the hole centre concentration. This implies that the majority of the photoexcited electrons enter and remain in the conduction band as EPR silent species, as proven by complementary IR experiments^{112,113}. In MgO, the spin concentration of hole centres essentially equals the concentration of trapped electrons.

10.2.2. Dynamics of charge trapping

For time-resolved measurements, the corresponding signal intensities were measured in-situ at a fixed resonance magnetic field value. Irradiation of the MgO powder sample with polychromatic light ($P = 94 \text{ mW}\cdot\text{cm}^{-2}$, $T = 90 \text{ K}$) is associated with different dynamics for hole and electron centre evolution (Fig. 10.4). The concentration of O^\cdot signals and trapped electrons not only grow at different rates, but also exhibit different saturation behaviour. In

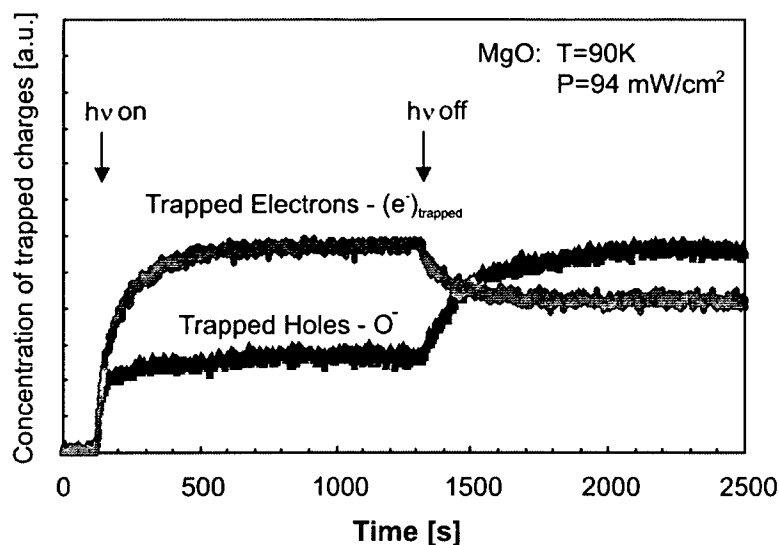


Fig. 10. 4: Light-induced charge separation in MgO: Concentration of paramagnetic hole centres O^\cdot and trapped electrons as a function of UV exposure time at $T = 90 \text{ K}$ ($P = 94 \text{ mW}\cdot\text{cm}^{-2}$ for $1.2 \text{ eV} < h\nu < 6.2 \text{ eV}$).

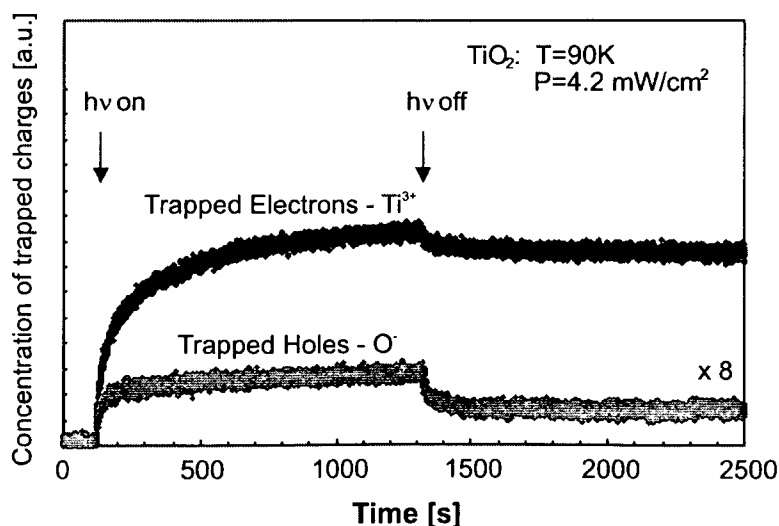


Fig. 10. 5: Light-induced charge separation in TiO_2 : Concentration of paramagnetic hole centres O^\cdot and trapped electrons (Ti^{3+}) as a function of UV exposure time at $T = 90 \text{ K}$ ($P = 4.2 \text{ mW}\cdot\text{cm}^{-2}$ for $1.2 \text{ eV} < h\nu < 6.2 \text{ eV}$).

particular, during the irradiation period of the first 500 s the amount of paramagnetic hole states reaches saturation, whereas the electron centre signal continues to grow with decreasing slope. After discontinuation of light exposure, the $O^{\cdot -}$ signal gains intensity. Conversely, the electron centre concentration decreases. The underlying processes of charge separation were proposed to occur via sequential absorption of two photons⁶³. When polychromatic light ($6.2 \text{ eV} < E < 1.2 \text{ eV}$) is used, this hole trapping process leading to $O^{\cdot -}$ formation (Eq.10.1) is accompanied by the excitation of localized holes to the valence band and their transfer to so far unspecified and EPR inactive sites. After discontinuation of light exposure a fraction of these holes are released from their unspecified sites and localize again at 3-coordinated surface ions⁶³. Another fraction recombines with electrons, previously detected as paramagnetic electron centres during UV exposure. This explains the reduction of the overall concentration in the subsequent dark period⁶³.

The situation is different for TiO_2 and the time evolution of trapped holes and trapped electrons during irradiation with polychromatic light ($P = 4.2 \text{ mW}\cdot\text{cm}^{-2}$, $T = 90 \text{ K}$) is shown in Fig. 10.5. Both curves clearly reveal a monotonous growth within the first $\sim 100 \text{ s}$; the Ti^{3+} signal levels thereafter at a constant value while the $O^{\cdot -}$ signal approaches steady state after $\sim 500 \text{ s}$. In line with the outcome in Fig. 10.3, the relative ratio of Ti^{3+} and $O^{\cdot -}$ signal intensities, which varies from sample to sample, never exceeds a value of 0.1. Stopping UV light exposure (after 1200 s) leads to an $O^{\cdot -}$ depletion to about 90% of the maximum intensity achieved during UV exposure and 50% for the Ti^{3+} signals. After the first 100 s in the dark, the corresponding signals remain constant on a time scale of hours, indicating that the state of charge separation is maintained¹¹². In this respect, temperature is a determining parameter. In TiO_2 , sample excitation at 298 K does not produce any paramagnetic states at all. Also raising the temperature to 298 K after UV excitation was performed at 90 K results in the complete annihilation of photogenerated charges. Because the relative Ti^{3+} concentration has a significant dependence on temperature between 90 K and 298 K, activation energies around 0.01 eV are estimated for the process of electron diffusion from their trapping sites, followed by recombination with holes. In MgO , temperature raise to 298 K only leads to the total depletion of trapped electrons, however, the concentration of trapped holes $[O^{\cdot -}]$ stays essentially constant on a time scale of hours.

For both oxides, the stability of trapped charges under the specified experimental conditions are a promising prerequisite for their further characterization. This can be done chemically, e.g. by studying the reactivity of trapped electrons towards different molecules from the gas-phase during as well as after UV exposure^{54,112,166}. But also physical experiments aiming at the interaction of trapped charges with low energy photons can be employed, for instance, to

determine the optical ionisation energies of the paramagnetic surface states⁶³. In conjunction with theory, providing a map of electronic states associated with different surface defects^{34,37,38,53,160,163,186} the investigation of light induced charge separation phenomena will allow a direct correlation between surface features on different oxides and their spectroscopic, electronic and chemical properties.

10.3. Conclusions

Ultraviolet light induced electron-hole pair excitations were studied on two fundamentally different nano-particulate oxides, MgO and TiO₂, for comparison. On both materials, holes become detectable as O⁻ species, generated from lattice O²⁻ in the valence band under continuous UV irradiation in the mW·cm⁻² range. The nature of the trapped electron species, however, strongly depends on the physical properties of the oxide. At lower temperatures (T < 200 K) electrons either are trapped at localized sites, such as paramagnetic F_S⁺ centres (MgO) and paramagnetic Ti³⁺ states (TiO₂) or predominantly remain in the conduction band as EPR silent and mobile species (TiO₂). On MgO, differences in the time-resolved build-up of trapped electrons and holes are explained by secondary reactions induced by the low energy part of the excitation spectrum. The study demonstrates that under high-vacuum conditions various types of EPR active electron and hole traps existing on the surface of oxide nanocrystals can be visualized by means of EPR spectroscopy in conjunction with UV excitation. In a next step, the energy distribution of these states that act as charge trapping sites will be analysed experimentally using light of known energy and photon flux.

11. Concluding remarks

In the first part of the present study the surface properties of TiO₂ nanoparticles (13 nm) were investigated with respect to the consumption and deactivation of charge carriers, which were generated by bulk excitation, using photons of supra band gap energy. For this purpose UV induced charge separation processes were investigated by a combined spectroscopic approach: delocalised electrons in the conduction band give rise to a free carrier absorption in the IR, whereas trapped and localized holes (O[•]) and electrons (Ti³⁺) are measured by EPR spectroscopy.

In the absence of electron and hole scavengers, at $p < 10^{-6}$ mbar, the majority of these charge carriers recombine within a few nanoseconds. Nevertheless, at $T \leq 140$ K charge carrier trapping processes can be observed on a time scale of minutes when irradiances in the $\text{mW}\cdot\text{cm}^{-2}$ range are used. It was found that most of the photoexcited electrons remain in the conduction band, whereas the holes get trapped and localized at the surface of the particles. The presence of oxygen as an electron scavenger enhances the efficiency of charge separation during UV exposure by a factor of 10 and leads to the photoadsorption of O₂. On this basis the number of charge carriers per nanoparticle was determined. The UV light irradiance during these experiments is crucial, since the efficiency of charge carrier separation sensitively depends on temperature. Local heating of the crystallites at irradiances $> 3 \text{ mW}\cdot\text{cm}^{-2}$ was observed and attributed to enhanced recombination of photogenerated charge carriers.

Elementary surface reactions involving H₂ and/or UV light on MgO nanocubes (5 nm) were investigated in the second part of the work. The characterizing procedure relies upon the interplay of diverse molecular spectroscopic techniques and quantum chemical calculations. There are sites where heterolytic H₂ splitting occurs giving rise to sharp IR active OH and MgH groups. UV-induced oxidation of the hydride groups initiates a reduction of anion deficient Mg²⁺ arrays to paramagnetic surface electron centres. Their characterization by EPR spectroscopy is corroborated by quantum chemical calculations, UV/Vis diffuse reflectance spectroscopy, and IR probe spectroscopy. Bleaching of the electron centres by N₂O gives rise to the appearance of EPR active O[•] radical species. In a third reaction step, homolytic H₂ splitting occurs at the O[•] radical sites giving rise to an IR active isolated free surface OH group. At the same time H[•] radicals are produced which migrate on the surface and finally are localized by the electron transfer to the remaining anion deficient Mg²⁺ arrays.

Electrons required in order to reduce anion deficient Mg^{2+} surface arrays to paramagnetic electron centres may also be provided by site-selective excitation of corner (282 nm, 4.5 eV) or edge oxygen anions (237 nm, 5.4 eV) in vacuo. Both processes end up with the formation of well-separated electron centres and hole centres O^- in corner positions. Obviously excitons generated on edge positions are mobile and are finally trapped in corner positions. This fact was used in order to site-specifically hydroxylate MgO nanocubes: hole centres at 3-coordinated corner oxygen sites were generated by UV irradiation ($E = 5.4$ eV). These highly reactive O^- radicals split H_2 homolytically and, in the course of this reaction, become hydroxylated and produce hydrogen atoms. The hydrogen atoms adsorb at cube edges and dissociate into surface trapped electrons and protons. It is proposed that the experimentally observed $(\text{H}^+)(e^-)$ centres are formed adjacent to the hydroxyl groups generated in the homolytic splitting process. *Ab initio* embedded cluster calculations reveal that the electronic properties of $(\text{H}^+)(e^-)(\text{H}^+)$ along MgO nanocube edges are consistent with both the electron paramagnetic resonance signal parameters and the reported optical absorption properties. The transformation of corner O^- centres into the $(\text{H}^+)(e^-)(\text{H}^+)$ type centres prevents their recombination with electronic surface centres and, hence, significantly alters the electronic structure of MgO nanocubes by introducing shallow electron traps.

In the third part of the present study light induced charge separation was studied at $P < 10^{-6}$ mbar in-situ by electron paramagnetic resonance spectroscopy on MgO and TiO_2 nanocrystals, which are used as prototypes for insulating and semiconducting metal oxides, respectively. For both materials, polychromatic excitation ($1.2 \text{ eV} < E < 6.2 \text{ eV}$) produces well-separated electron and hole centres. In the case of MgO only surface features such as low coordinated ions are excited with energies < 6.2 eV. On TiO_2 with a band gap of 3.2 eV, however, the generation of electron/ hole pairs is induced also in the bulk of the particles.

Photo-generated electrons and holes get strongly localized on MgO nanocubes and may be detected by EPR spectroscopy as paramagnetic F_S^+ and O^- centres, respectively. The situation is quite different in the case of TiO_2 : while holes are trapped as O^- , the respective electrons remain in a free state and give rise to an absorption in the IR. Electron and hole trapping in TiO_2 particles is observed only at temperatures $T < 140$ K. On the other hand, the charge separation state can be maintained even at 298 K in the case of MgO nanocubes.

In conclusion, the results presented in this work provide new insights into both photochemistry and photophysics on well-defined semiconducting and insulating model systems and may contribute to the elucidation of photoinduced processes on more realistic systems as used in photocatalysis.

Appendix

Publications:

M. Sterrer, T. Berger, O. Diwald, E. Knözinger, P. V. Sushko, A. L. Shluger:
"Chemistry at corners and edges: generation and adsorption of H-atoms on the surface of MgO nanocubes"
J. Chem. Phys. **2005** submitted.

T. Berger, M. Sterrer, O. Diwald, E. Knözinger:
"Charge trapping and the photoadsorption of O₂ on dehydroxylated TiO₂ nanocrystals – an electron paramagnetic resonance study"
Chem. Phys. Chem. **2005** accepted.

T. Berger, M. Sterrer, S. Stankic, J. Bernardi, O. Diwald, E. Knözinger:
"Trapping of photogenerated charges in oxide nanoparticles"
Mat. Sci. Eng. C, **2005** accepted.

T. Berger, M. Sterrer, O. Diwald, E. Knözinger, D. Panayotov, T. L. Thompson, J. T. Yates Jr.:
"Light-induced charge separation in anatase TiO₂ particles"
J. Phys. Chem. B. **2005**, 109, 6061.

T. Berger, M. Sterrer, O. Diwald, E. Knözinger:
"The colour of the MgO surface- a UV/Vis diffuse reflectance investigation of electron traps"
J. Phys. Chem. B **2004**, 108, 7280.

M. P. Green, S. Pichlmair, M. M. B. Marques, H. J. Martin, O. Diwald, T. Berger, J. Mulzer:
"Synthesis of analogue structures of the p-quinone methide moiety of kendomycin"
Org. Lett. **2004**, 6, 3131.

M. Sterrer, T. Berger, S. Stankic, O. Diwald, E. Knözinger:
"Spectroscopic properties of trapped electrons on the surface of MgO nanoparticles"
Chem. Phys. Chem. **2004**, 5, 1695.

M. Sterrer, T. Berger, O. Diwald, E. Knözinger:
"Energy transfer on the MgO surface - monitored by UV-induced H₂ chemisorption"
J. Am. Chem. Soc. **2003**, 125, 195.

O. Diwald, T. Berger, M. Sterrer, E. Knözinger:
"Chemistry and photochemistry of H₂ on MgO surfaces"
Stud. Surf. Sci. Catal. **2001**, 140, 237.

Lectures:

"Light-induced charge separation and charge recombination effects in nanometer-sized TiO₂ particles"
COST D 19 meeting 2005, Torino/Italy; 14.05.2005.

"Light-induced charge separation in TiO₂ nanocrystals – a spectroscopic investigation of model catalysts"

104th Meeting of the Bunsen Society of Physical Chemistry, Frankfurt/Germany; 07.05.2005.

"Spektroskopische Untersuchung von Ladungseinfang-Prozessen an nanostrukturierten TiO₂ Photokatalysatoren"

38. Jahrestreffen Deutscher Katalytiker, Weimar/Germany, 16.03.2005.

"Charge trapping processes in insulating and semiconducting metal oxide nanoparticles"

Center for Computational Materials Science, Vienna/Austria; 27.01.2005.

Conference contributions:

O. Diwald, M. Sterrer, T. Berger, S. Stankic, M. Müller, E. Knözinger:

"Site-specific processes on MgO nanocubes"

COST D 19 meeting 2005, Torino/Italy; 13. - 14.05.2005.

A. Riss, T. Berger, J. Bernardi, O. Diwald, E. Knözinger:

"Spectroscopic properties of H₂Ti₃O₇ nanotubes"

104th Meeting of the Bunsen Society of Physical Chemistry, Frankfurt/Germany; 05. – 07.05.2005.

S. Stankic, T. Berger, A. Riss, M. Sterrer, O. Diwald, E. Knözinger:

"Oberflächen-Funktionalisierung von MgO Nanoteilchen durch Ca Dotierung"

38. Jahrestreffen Deutscher Katalytiker, Weimar/Germany, 16. - 18.03.2005.

M. Sterrer, T. Berger, O. Diwald, E. Knözinger, P. V. Sushko, A. L. Shluger:

"Influence of hydrogen on the properties of trapped charges on the MgO surface"

The fourth International Workshop on Oxide Surfaces, Centre Langevin, Aussois/France; 04. - 08.01.2005.

O. Diwald, S. Stankic, T. Berger, A. Riss, M. Sterrer, J. Bernardi, E. Knözinger:

"Light induced surface processes on MgO and MgO-based nanocrystals"

The fourth International Workshop on Oxide Surfaces, Centre Paul Langevin, Aussois/France; 04. - 08.01.2005.

T. Berger, M. Sterrer, O. Diwald, T. L. Thompson, D. Panayotov, E. Knözinger, J. T. Yates Jr.:

"Charge trapping in nano-sized TiO₂ photocatalysts"

Photocatalytically Active Nanoscale Scavengers and Sensors /MURI Review meeting, Jackson Hole, Wyoming/USA; 18. - 19.10.2004.

O. Diwald, M. Sterrer, T. Berger, S. Stankic, A. Riss, E. Knözinger:

"Light induced surface processes on oxide nanocrystals"

Environmental Molecular Sciences Laboratory, Richland/USA; 21.10.2004.

T. Berger, A. Riss, S. Stankic, M. Sterrer, O. Diwald, E. Knözinger:

"Charge trapping processes in nano-sized TiO₂ photocatalysts"

7th Pannonian International Symposium on Catalysis, Srni/Czech Republic; 12. - 16.09.2004.

S. Stankic, T. Berger, A. Riss, O. Diwald, E. Knözinger:

"Novel surface properties of Ca doped MgO nanoparticles"

7th Pannonian International Symposium on Catalysis, Srni/Czech Republic; 12. - 16.09.2004.

J. Sa, T. Berger, H. Vinek:

"A new approach to remove nitrates from drinking water"

3rd International Taylor Conference, Belfast/UK; 05. - 08.09.2004.

T. Berger, O. Diwald, E. Knözinger, S. Stankic, M. Sterrer:

"Surface properties of vapour deposited metal oxides"

Catalysis and 21th century challenges: basic research and the needs of society, Paris/France; 11. - 16.07.2004.

O. Diwald, M. Sterrer, T. Berger, E. Knözinger:

"Light induced charge separation on MgO and TiO₂ nanoparticles"

EMRS spring meeting 2004, Strasbourg/France; 25.05.2004.

O. Diwald, S. Stankic, T. Berger, M. Sterrer, E. Knözinger:

"Chemical and light induced address of specific surface sites on metal oxides"

COST D 19 meeting 2004, Torino/Italy; 02.04.2004.

M. Sterrer, O. Diwald, T. Berger, E. Knözinger:

"Potential and limitations of EPR probe spectroscopy in the characterization of metal oxide surface ensembles"

5th Meeting of the European Federation of EPR Groups, Lisboa/Portugal; 07. - 11.09.2003.

E. Knözinger, M. Sterrer, T. Berger, O. Diwald:

"Chemistry and photochemistry on the surface of MgO nanocubes"

EuropaCat VI, Innsbruck/Austria; 31.08. - 04.09.2003.

T. Berger, O. Diwald, M. Sterrer, E. Knözinger:

"Colour centres on the surface of MgO nanoparticles"

225th National Meeting of the American Chemical Society, New Orleans/USA; 23. - 27.03.2003.

M. Sterrer, T. Berger, O. Diwald, E. Knözinger:

"Chemistry and photochemistry on the surface of MgO nanoparticles"

3rd International Workshop on Oxide Surfaces, Sapporo/Japan; 27. - 31.01.2003.

T. Berger, O. Diwald, M. Sterrer, E. Knözinger:

"Optical, paramagnetic and vibrational properties of various colour centres on the surface of nanosized MgO"

International Workshop on Nanochemistry, Vienna/Austria, 26. - 28.09.2002.

References

- [1] V. E. Henrich, P.A. Cox, *The Surface Science of Metal Oxides*, Cambridge University Press, Cambridge, 1994.
- [2] P. A. Cox, *Transition Metal Oxides: An Introduction to Their Electronic Structure and Properties*, Clarendon Press, Oxford, 1992.
- [3] M. S. Reisch, *C&EN* 2003, 81, 13.
- [4] J. R. Owen, *Chem. Soc. Rev.* 1997, 26, 259.
- [5] A. Fujishima, K. Honda, *Nature* 1972, 238, 37.
- [6] M. Grätzel, *Nature* 2001, 414, 338.
- [7] G. Ertl, H. Knözinger, J. Weitkamp, eds., *Handbook of Heterogeneous Catalysis*, Wiley-VCH, Weinheim, 1997.
- [8] J. Peral, X. Domenech, D. F. Ollis, *J. Chem. Technol. Biotechnol.* 1997, 70, 117.
- [9] A.L. Linsebigler, G. Lu, J.T. Yates, Jr., *Chem. Rev.* 1995, 95, 735.
- [10] M.R. Hoffmann, S.T. Martin, W.Y. Choi, D.W. Bahnemann, *Chem. Rev.* 1995, 95, 69.
- [11] C. J. Först, C. R. Ashman, K. Schwarz, P. E. Blöchl, *Nature* 2004, 427, 53.
- [12] Y. Matsumoto, T. Shono, T. Hasegawa, T. Fukumura, K. Kawasaki, P. Ahmet, T. Chikyow, S. Koshihara, and H. Koinuma, *Science* 2001, 291, 854.
- [13] M. Fernandez-Garcia, A. Martinez-Arias, J. C. Hanson, J. A. Rodriguez, *Chem. Rev.* 2004, 104, 4063.
- [14] A. T. Bell, *Science* 2003, 299, 1688.
- [15] D. Beydoun, R. Amal, G. Low, S. McEvoy, *J. Nanoparticle Res.* 1999, 1, 439.
- [16] A. Gribb, J. F. Banfield, *Am. Mineralogist* 1997, 82, 717.
- [17] M. Lazzeri, A. Vittadini, A. Selloni, *Phys. Rev. B* 2001, 63, 155409.
- [18] C. B. Duke, ed., *Surface Science: The First Thirty Years*, Elsevier, Amsterdam, 1994.
- [19] U. Diebold, *Surf. Sci. Rep.* 2003, 48, 53.
- [20] H.-J. Freund, H. Kühlenbeck, J. Libuda, G. Rupprechter, M. Bäumer, H. Hamann, *Topics Catal.* 2001, 15, 201.
- [21] G. Spoto, E. N. Gribov, G. Ricchiardi, A. Damin, D. Scarano, S. Bordiga, C. Lamberti, A. Zecchina, *Progr. Surf. Sci.*, 2004, 76, 71.
- [22] T. Ohno, K. Sarukawa, M. Matsumura, *New J. Chem.* 2002, 26, 1167.
- [23] J. B. Lowekamp, G. S. Rohrer, P. A. M. Hotsenpiller, J. D. Bolt, W. E. Farneth, *J. Phys. Chem. B* 1998, 102, 7323.
- [24] P. A. M. Hotsenpiller, J. D. Bolt, W. E. Farneth, J. B. Lowekamp, G. S. Rohrer, *J. Phys. Chem. B* 1998, 102, 3216.
- [25] T. Ohno, K. Tokieda, S. Higashida, M. Matsumura, *Appl. Catal. A* 2003, 244, 383.
- [26] A. Gribb, J. F. Banfield, *Am. Mineralogist* 1997, 82, 717.
- [27] M. Lazzeri, A. Vittadini, A. Selloni, *Phys. Rev. B* 2001, 63, 155409.
- [28] K. I. Fukui, H. Onishi, Y. Iwasawa, *Phys. Rev. Lett.* 1997, 79, 4202.
- [29] U. Diebold, J. Lehman, T. Mahmoud, M. Kuhn, G. Leonardelli, W. Hebenstreit, M. Schmid, P. Varga, *Surf. Sci.* 1998, 411, 137.
- [30] R. Schaub, E. Wahlström, A. Ronnau, E. Laesgaard, I. Stensgaard, F. Besenbacher, *Science* 2003, 299, 377.
- [31] W. Hebenstreit, N. Ruzycki, G. S. Herman, Y. Gao, U. Diebold, *Phys. Rev. B* 2000, 64, R16344.
- [32] G. S. Herman, M. R. Sievers, Y. Gao, *Phys. Rev. Lett.* 2000, 84, 3354.
- [33] M. Sterrer, E. Fischbach, T. Risse, H. J. Freund, *Phys. Rev. Lett.* 2005, accepted.
- [34] A. L. Shluger, P. V. Sushko, L. N. Kantorovic, *Phys. Rev. B* 1999, 59, 2417.
- [35] A. J. Tench, R. L. Nelson, *J. Colloid Interface Sci.* 1968, 26, 364.
- [36] M. C. Paganini, M. Chiesa, E. Giamello, S. Coluccia, G. Martra, D. M. Murphy, G. Pacchioni, *Surf. Sci.* 1999, 421, 246.
- [37] L. Ojamäe, C. Pisani, *J. Chem. Phys.* 1998, 109, 10984.
- [38] D. Ricci, C. Di Valentin, G. Pacchioni, P. V. Sushko, A. L. Shluger, E. Giamello, *J. Am. Chem. Soc.* 2003, 125, 738.
- [39] M. Chiesa, M. C. Paganini, E. Giamello, C. Di Valentin, G. Pacchioni, *Angew. Chem., Int. Ed.* 2003, 42, 1759.
- [40] O. Diwald, E. Knözinger, G. Martra, *J. Chem. Phys.* 1999, 111, 6668.
- [41] R. Wang, K. Hashimoto, A. Fujishima, M. Chikuni, E. Kojima, A. Kitamura, M. Shimohigoshi, T. Watanabe, *Nature*, 1997, 388, 431.
- [42] A. V. Emeline, G. N. Kuzmin, D. Purevdorj, V. K. Ryabchuk, N. Serpone, *J. Phys. Chem. B* 2000, 104, 2989.

- [43] G. Rothenberger, J. Moser, M. Grätzel, N. Serpone, D. K. Sharma, *J. Am. Chem. Soc.* **1985**, *107*, 8054.
- [44] O. Carp, C. L. Huisman, A. Reller, *Progr. Solid State Chem.* **2004**, *32*, 33.
- [45] J. I. Pankove, *Optical Processes in Semiconductors*, Dover, New York, **1975**.
- [46] P. K. Basu, *Theory of Optical Processes in Semiconductors*, Oxford University Press, New York, **1997**.
- [47] C. Di Valentin, G. Pacchioni, A. Selloni, *Phys. Rev. B* **2004**, *70*, 085116.
- [48] S. Livraghi, A. Votta, M. C. Paganini, E. Giamello, *Chem. Comm.* **2005**, *4*, 498.
- [49] O. Diwald, T. L. Thompson, E. G. Goralski, S. D. Walck, J. T. Yates, Jr., *J. Phys. Chem. B* **2004**, *108*, 52.
- [50] E. Garrone, A. Zecchina, F. S. Stone, *Phil. Mag. B* **1980**, *42*, 683.
- [51] S. Stankic, M. Müller, O. Diwald, E. Knözinger, M. Sterrer, J. Bernardi, *Angew. Chem.* **2005**, in press.
- [52] S. Coluccia, A. M. Deane, A. J. Tench, *J. Chem. Soc., Faraday Trans.1* **1978**, *74*, 2913.
- [53] O. Diwald, M. Sterrer, E. Knözinger, P. V. Sushko, A. L. Shluger, *J. Chem. Phys.* **2002**, *116*, 1707.
- [54] M. Sterrer, T. Berger, O. Diwald, E. Knözinger, *J. Am. Chem. Soc.* **2003**, *125*, 195.
- [55] K. Beck, A. L. Shluger, COST D19 meeting Torino/Italy, 13.-14.5.2005.
- [56] J. A. Weil, J. R. Bolton, J. E. Wertz, *Electron Paramagnetic Resonance - Elementary Theory and Practical Applications* J. Wiley&Sons, Inc., New York, **1994**
- [57] N. M. Atherton, *Principles of Electron Spin Resonance* Ellis Horwood PTR Prentice Hall, Physical Chemistry Series, London, **1983**.
- [58] H. P. Boehm, H. Knözinger, *Catalysis-science and technology* **1983**, *4*, 39.
- [59] P. Kubelka, F. Munk, *Z. Tech. Physik* **1931**, *12*, 593.
- [60] S. Benfer, E. Knözinger, *J. Mater. Chem.* **1999**, *9*, 1203.
- [61] P. Hofmann, K. H. Jacob, E. Knözinger, *Ber. Bunsenges. Phys. Chem.* **1993**, *97*, 316.
- [62] G. P. Lozos, B. M. Hoffman, C. G. Franz, modified by J. M. Lagan (SLAFiBS), SIM14S-ESR spectrum simulation, DOS version of 24/06/1996.
- [63] M. Sterrer, O. Diwald, E. Knözinger, P. V. Sushko, A. L. Shluger, *J. Phys. Chem. B.* **2002**, *106*, 12478.
- [64] P. Hoffmann, *Dissertation*, Universität-GH-Siegen **1986**.
- [65] P. Hofmann, *Dissertation*, TU Wien **1997**.
- [66] T. H. Ballinger, J. C. S. Wong, J. T. Yates, Jr., *Langmuir* **1992**, *8*, 1676.
- [67] J. C. S. Wong, A. Linsebigler, G. Q. Lu, J. F. Fan, J. T. Yates, Jr., *J. Phys. Chem.* **1995**, *99*, 335.
- [68] *The Book of Photon Tools*; Oriol Corporation.
- [69] N. Serpone, E. Pilezzetti, *Photocatalysis: Fundamentals and Applications*; Wiley Interscience: New York, **1989**.
- [70] K. Kalayanasundaram, M. Gratzel, *Coord. Chem. Rev.* **1998**, *77*, 347.
- [71] M. A. Henderson, W. S. Epling, C. H. F. Peden, C. L. Perkins, *J. Phys. Chem. B.* **2003**, *107*, 534.
- [72] D. Panayotov, J. T. Yates, Jr., *Chem. Phys. Lett.* **2003**, *381*, 154.
- [73] I. Bedja, P. V. Kamat, *J. Phys. Chem.* **1995**, *99*, 9182.
- [74] R. F. Howe, *Dev. Chem. Eng. Mineral Process.* **1998**, *6*, 55.
- [75] D. W. Bahnemann, D. Bockelmann, R. Goslich, M. Hilgendorff, D. Weichgrebe, *Photocatalytic Purification and Treatment of Water and Air*, Elsevier Science Publishers, **1993**.
- [76] U. Diebold, N. Ruzycski, G. S. Herman, A. Selloni, *Catal. Today* **2003**, *85*, 93.
- [77] L. X. Chen, T. Rajh, Z. Y. Wang, M. C. Thurnauer, *J. Phys. Chem. B.* **1997**, *101*, 10688.
- [78] D. C. Hurum, A. G. Agrios, K. A. Gray, T. Rajh, M. C. Thurnauer, *J. Phys. Chem. B.* **2003**, *107*, 4545.
- [79] P. Meriaudeau, M. Che, P. C. Gravelle, S. Teichner, *Bull. Soc. Chim. France* **1971**, *1*, 13.
- [80] T. Rajh, O. V. Makarova, M. C. Thurnauer, D. Cropek, in *Synthesis, Functionalization and Surface Treatment of Nanoparticles*; Baraton, M. I., Ed.; American Science Publishers, **2003**.
- [81] N. Serpone, D. Lawless, R. Khairutdinov, E. Pelizzetti, *J. Phys. Chem.* **1995**, *99*, 16655.
- [82] D. P. Colombo, R. M. Bowman, *J. Phys. Chem.* **1995**, *99*, 11752.
- [83] D. P. Colombo, R. M. Bowman, *J. Phys. Chem.* **1996**, *100*, 18445.
- [84] D. W. Bahnemann, M. Hilgendorff, R. Memming, *J. Phys. Chem. B.* **1997**, *101*, 4265.
- [85] A. Yamakata, T. Ishibashi, H. Onishi, *Chem. Phys. Lett.* **2001**, *333*, 271.
- [86] S. H. Szczepankiewicz, J. A. Moss, M. R. Hoffmann, *J. Phys. Chem. B.* **2002**, *106*, 2922.
- [87] S. H. Szczepankiewicz, J. A. Moss, M. R. Hoffmann, *J. Phys. Chem. B.* **2002**, *106*, 7654.
- [88] M. A. Henderson, J. M. White, H. Uetsuka, H. Onishi, *J. Am. Chem. Soc.* **2003**, *125*, 14974.

- [89] M. Sterrer, O. Diwald, E. Knözinger, *J. Phys. Chem. B* **2000**, *104*, 3601.
- [90] A. V. Emeline, L. G. Smirnova, G. N. Kuzmin, L. L. Basov, N. Serpone, *Photochem. Photobiol. A: Chemistry* **2002**, *148*, 97.
- [91] A. L. Attwood, D. M. Murphy, J. L. Edwards, T. A. Egerton, R. W. Harrison, *Res. Chem. Intermediat.* **2003**, *29*, 449.
- [92] G. Riegel, J. R. Bolton, *J. Phys. Chem.* **1995**, *99*, 4215.
- [93] E. Servicka, M. W. Schlierkamp, R. N. Schindler, *Z. Nanoforsch.* **1981**, *36a*, 226.
- [94] M. Anpo, M. Che, B. Fubini, E. Garrone, E. Giamello, M. C. Paganini, *Top. Catal.* **1999**, *8*, 189.
- [95] R. F. Howe, M. Gratzel, *J. Phys. Chem.* **1987**, *91*, 3906.
- [96] C. A. Jenkins, D. M. Murphy, *J. Phys. Chem. B* **1999**, *103*, 1019.
- [97] O. I. Micic, Y. N. Zhang, K. R. Cromack, A. D. Trifunac, M. C. Thurnauer, *J. Phys. Chem.* **1993**, *97*, 7277.
- [98] M. Che, A. J. Tench, *Adv. Catal.* **1982**, *31*, 78.
- [99] A. M. Volodin, A. E. Chercashin, V. S. Zakharenko, *React. Kin. Catal. Lett.* **1979**, *11*, 103.
- [100] J. M. Herrmann, J. Disdier, P. Pichat, *J. Chem. Soc. Faraday Trans I*, **1981**, *77*, 2815.
- [101] J. Nelson, A. Eppler, I. M. Ballard, *Photochem. Photobiol. A: Chemistry* **2002**, *148*, 25.
- [102] A. Yamakata, T. Ishibashi, H. Onishi, *J. Mol. Catal. a-Chem.* **2003**, *199*, 85.
- [103] A. Emeline, A. Salinaro, N. Serpone, *J. Phys. Chem. B*, **2000**, *104*, 11202.
- [104] M. Che, A. J. Tench, *Adv. Catal.* **1983**, *32*, 2.
- [105] C. Y. Liu, A. J. Bard, *J. Phys. Chem.* **1989**, *93*, 3232.
- [106] A. K. Ghosh, F. G. Wakim, P. R. Adiss, *Phys. Rev.* **1969**, *184*, 979.
- [107] P. C. Gravelle, F. Juillet, P. Meriaudeau, S. Teichner, *Faraday Discuss. Chem. Soc.* **1971**, *52*, 140.
- [108] I. Justicia, P. Ordejon, G. Canto, J. L. Mozos, J. Fraxedas, G. A. Battiston, R. Gerbasi, A. Figueras, *Adv. Mater.* **2002**, *14*, 1399.
- [109] I. Nakamura, N. Negishi, S. Kutsuna, T. Ihara, S. Sugihara, E. Takeuchi, *J. Mol. Catal. a-Chem.* **2000**, *161*, 205.
- [110] T. Yoshihara, R. Katoh, A. Furube, Y. Tamaki, M. Murai, K. Hara, H. Arakawa, M. Tachiya, *J. Phys. Chem. B* **2004**, *108*, 3817 and references therein.
- [111] T. Bredow, G. Pacchioni, *Chem. Phys. Lett.* **2002**, *355*, 417.
- [112] T. Berger, M. Sterrer, O. Diwald, E. Knözinger, M. Panayotov, T. L. Thompson, J. T. Yates Jr., *J. Phys. Chem. B* **2005**, *109*, 6061.
- [113] T. Berger, M. Sterrer, O. Diwald, E. Knözinger, *Chem. Phys. Chem.* **2005**, accepted.
- [114] C. Naccache, P. Meriaudeau, M. Che, A. J. Tench, *Trans. Faraday Soc.* **1971**, *67*, 506.
- [115] A. Hagfeldt, M. Grätzel, *Acc. Chem. Res.* **2000**, *33*, 269.
- [116] D. L. Bahnemann, *Solar Energy* **2004**, *77*, 445.
- [117] Y. Nosaka, M. Kishimoto, J. Nishino, *J. Phys. Chem. B* **1998**, *102*, 10279.
- [118] J. Fan, J. T. Yates Jr., *J. Am. Chem. Soc.* **1996**, *118*, 4686.
- [119] N. Djeghri, S. J. Teichner, *J. Catal.* **1980**, *62*, 99.
- [120] R. I. Bickley, G. Munuera, F. S. Stone, *J. Catal.* **1973**, *31*, 398.
- [121] G. K. Mor, K. Shankar, M. Paulose, O. K. Varghese, C. A. Grimes, *Nano Letters* **2005**, *5*, 191.
- [122] A. J. Maira, K. L. Yeung, C. Y. Lee, P. L. Yue, C. K. Chan, *J. Catal.* **2000**, *192*, 185.
- [123] L. Cao, A. Huang, F. J. Spiess, S. L. Suib, *J. Catal.* **1999**, *188*, 48.
- [124] A. J. Maira, K. L. Yeung, J. Soria, J. M. Coronado, C. Belver, C. Y. Lee, V. Augugliaro, *Appl. Catal. B* **2001**, *29*, 327.
- [125] Z. Zhang, C. C. Wang, R. Zakaria, J. Y. Ying, *J. Phys. Chem. B* **1998**, *102*, 10871.
- [126] H. Zhang, R. L. Penn, R. J. Hamers, J. F. Banfield, *J. Phys. Chem. B* **1999**, *103*, 4656.
- [127] M. A. Grela, A. J. Colussi, *J. Phys. Chem.* **1996**, *100*, 18214.
- [128] C. Wang, Z. Zhang, J. Y. Ying, *Nanostr. Mater.* **1997**, *9*, 583.
- [129] J. M. Coronado, A. J. Maira, J. C. Conesa, K. L. Yeung, V. Augugliaro, J. Soria, *Langmuir* **2001**, *17*, 5368.
- [130] C. Almquist, P. Biswas, *J. Catal.* **2002**, *212*, 145.
- [131] K. L. Yeung, S. T. Yau, A. J. Maira, J. M. Coronado, J. Soria, P. L. Yue, *J. Catal.* **2003**, *219*, 107.
- [132] Z. Ding, G. Q. Lu, P. F. Greenfield, *J. Phys. Chem. B* **2002**, *104*, 4815.
- [133] A. Sclafani, L. Palmisano, M. Schiavello, *J. Phys. Chem. B* **1990**, *94*, 829.
- [134] H. Uetsuka, H. Onishi, M. A. Henderson, J. M. White, *J. Phys. Chem. B* **2004**, *108*, 10621.
- [135] D. C. Hurum, K. A. Gray, T. Rajh, M. C. Thurnauer, *J. Phys. Chem. B*, **2005**, *109*, 977.
- [136] M. A. Fox, M. T. Dulay, *Chem. Rev.* **1993**, *93*, 341.
- [137] C. S. Turchi, D. F. Ollis, *J. Catal.* **1990**, *122*, 178.

- [138] C. Wang, A. Heller, H. Gerischer, *J. Am. Chem. Soc.* **1992**, *114*, 5230.
- [139] A. L. Attwood, J. L. Edwards, C. C. Rowlands, D. M. Murphy, *J. Phys. Chem. A* **2003**, *107*, 1779.
- [140] P. Meriaudeau, M. Che, C. K. Jørgensen, *Chem. Phys. Lett.* **1970**, *5*, 131.
- [141] a) P. C. Gravelle, F. Juillet, P. Meriaudeau, S. Teichner, *Faraday Discuss. Chem. Soc.* **1971**, *52*, 140; b) R. I. Bickley, F. S. Stone, *J. Catal.* **1973**, *31*, 389; c) A. H. Boonstra, C. A. H. A. Mutsaers, *J. Phys. Chem.* **1975**, *79*, 1694; d) G. Munuera, V. Rives-Amau, A. Saucedo, *J. Chem. Soc., Farad. Trans. I* **1979**, *75*, 736.
- [142] P. Pichat, in: *Homogeneous and Heterogeneous Photocatalysis*, E. Pelizzetti, N. Serpone (eds.), D. Reidel Publishing Company, **1986**, p.533.
- [143] K. Ishibashi, A. Fujishima, T. Watanabe, K. Hashimoto, *J. Phys. Chem. B* **2000**, *104*, 4934.
- [144] S. Ahmed, S. M. Fonseca, T. J. Kemp, P. R. Unwin, *J. Phys. Chem. B* **2003**, *107*, 5892.
- [145] E. Knözinger, M. Sterrer, O. Diwald, *J. Mol. Catal. A: Chem.* **2000**, *162*, 83.
- [146] E. Yagi, R. R. Hasiguti, M. Aono, *Phys. Rev. B* **1996**, *54*, 7945.
- [147] A. Goossens, B. van der Zanden, J. Schoonman, *Chem. Phys. Lett.* **2000**, *331*, 1.
- [148] B. van der Zanden, A. Goossens, *J. Phys. Chem. B* **2000**, *104*, 7171.
- [149] H. van't Spijker, B. O'Regan, A. Goossens, *J. Phys. Chem. B* **2001**, *105*, 7220.
- [150] M. D. Ward, A. J. Bard, *J. Phys. Chem.* **1982**, *86*, 3599.
- [151] D. Bahnemann, A. Henglein, J. Lilie, L. Spanhel, *J. Phys. Chem.* **1984**, *88*, 709.
- [152] P. V. Kamat, *Langmuir* **1985**, *1*, 608.
- [153] Y. Sun, A. Li, M. Qi, L. Zhang, X. Yao, *J. Mater. Sci.* **2002**, *37*, 1343.
- [154] L. C. Feldman, E. P. Gusev, E. Garfunkel, *Fundamental Aspects of Ultrathin Dielectrics on Si-based Devices*, Kluwer, Dordrecht, **1998**.
- [155] R. A. McKee, F. L. Walker, M. F. Chisholm, *Phys. Rev. Lett.* **1998**, *81*, 3014.
- [156] M. Suzuki, T. Ami, *Mater. Sci. Eng. B* **1996**, *41*, 166.
- [157] G. Pacchioni, *The Chemical Physics of Solid Surfaces Vol. 9, Oxide Surfaces*; Woodruff P., Ed.; Elsevier, Amsterdam, **2000**, 94.
- [158] H. Idriss, M. Barteau, *Adv. Catal.* **2000**, *45*, 261.
- [159] J. H. Lunsford, in: G. Ertl, H. Knözinger, J. Weitkamp (Eds.), *Handbook of Heterogeneous Catalysis Vol. 4*, VCH, Weinheim, **1997**, 1843.
- [160] P. V. Sushko, J. L. Gavartin, A. L. Shluger, *J. Phys. Chem. B* **2002**, *106*, 2269.
- [161] A. Zecchina, D. Scarano, S. Bordiga, G. Spoto, C. Lamberti, *Adv. Catal.* **2001**, *46*, 265.
- [162] E. Giamello, M. C. Paganini, D. Murphy, A. M. Ferrari, G. Pacchioni, *J. Phys. Chem. B* **1997**, *101*, 971.
- [163] D. Ricci, G. Pacchioni, P. V. Sushko, A. L. Shluger, *J. Chem. Phys. B* **2002**, *117*, 2844.
- [164] M. C. Wu, C. M. Truong, K. Coulter, D. W. Goodman, *J. Am. Chem. Soc.* **1992**, *114*, 7565.
- [165] S. Abbet, A. Sanchez, U. Heiz, W. D. Schneider, A. M. Ferrari, G. Pacchioni, N. Rösch, *J. Am. Chem. Soc.* **2000**, *122*, 3453.
- [166] M. Chiesa, E. Giamello, D. M. Murphy, G. Pacchioni, M. C. Paganini, R. Soave, Z. Sojka, *J. Phys. Chem. B* **2001**, *105*, 497.
- [167] M. C. Wu, C. M. Truong, D. W. Goodman, *Phys. Rev. B* **1992**, *46*, 12688.
- [168] J. Kramer, W. Ernst, C. Tegenkamp, H. Pfnür, *Surf. Sci.* **2002**, *517*, 87.
- [169] D. M. Murphy, E. Giamello, *J. Phys. Chem.* **1995**, *99*, 15172.
- [170] O. Diwald, T. Berger, M. Sterrer, E. Knözinger, *Stud. Surf. Sci. Catal.* **2001**, *140*, 237.
- [171] B. Henderson, J. E. Wertz, *Adv. Phys.* **1968**, *17*, 749.
- [172] S. Coluccia, M. Baricco, L. Marchese, G. Martra, A. Zecchina, *Spectrochim. Acta A* **1993**, *49*, 1289.
- [173] S. Schintke, S. Messerli, M. Pivetta, F. Patthey, L. Libioulle, M. Stengel, A. De Vita, W. D. Schneider, *Phys. Rev. Lett.*, **2001**, 8727, 276801.
- [174] J. Kramer, C. Tegenkamp, H. Pfnür, *Phys. Rev. B* **2003**, *67*, 235401.
- [175] C. Sousa, G. Pacchioni, F. Illas, *Surf. Sci.* **1999**, *429*, 217.
- [176] G. Pinarello, C. Pisani, A. D'Ercole, M. Chiesa, M. C. Paganini, E. Giamello, O. Diwald, *Surf. Sci.* **2001**, *494*, 95.
- [177] a) G. Pacchioni, *Chem. Phys. Chem* **2003**, *4*, 1041; b) C. Di Valentin, C. Locati, G. Pacchioni, *Chem. Phys. Chem* **2004**, *5*, 642; c) H. Häkkinen, S. Abbet, A. Sanchez, U. Heiz, U. Landman, *Angew. Chem.* **2003**, *115*, 1335; *Angew. Chem. Int. Ed.* **2003**, *42*, 1297; d) G. Spoto, E. N. Gribov, G. Ricchiardi, A. Damin, D. Scarano, S. Bordiga, C. Lamberti, A. Zecchina, *Prog. Surf. Sci.* **2004**, *76*, 71.
- [178] J. M. Spaeth, J. R. Niklas, R. H. Bartram, *Structural Analysis of Point Defects in Solids*, Springer-Verlag, Berlin, **1992**.

- [179] O. Diwald, P. Hofmann, E. Knözinger, *Phys. Chem. Chem. Phys.* **1999**, *1*, 713.
- [180] G. Pacchioni, P. Pescarmona, *Surf. Sci.* **1998**, *412/413*, 657.
- [181] D. M. Murphy, R. D. Farley, I. J. Purnell, C. C. Rowlands, A. R. Jacob, M. C. Paganini, E. Giamello, *J. Phys. Chem. B* **1999**, *103*, 1944.
- [182] I. J. Purnell, M. Chiesa, R. D. Farley, D. M. Murphy, C. C. Rowlands, M. C. Paganini, E. Giamello, *Magn. Res. Chem.* **2002**, *40*, 381.
- [183] T. Berger, M. Sterrer, O. Diwald, E. Knözinger, *J. Phys. Chem B* **2004**, *108*, 7280.
- [184] O. Diwald, M. Sterrer, E. Knözinger, *Phys. Chem. Chem. Phys.* **2002**, *4*, 2811.
- [185] M. Sterrer, T. Berger, S. Stankic, O. Diwald, E. Knözinger, *Chem. Phys. Chem.* **2004**, *5*, 1695.
- [186] P. V. Sushko, A. L. Shluger, C. R. A. Catlow, *Surf. Sci.* **2000**, *450*, 153.
- [187] M. Chiesa, P. Martino, E. Giamello, C. Di Valentin, A. del Vitto, G. Pacchioni, *J. Phys. Chem. B* **2004**, *108*, 11529.
- [188] A. D' Ercole, C. Pisani, *J. Chem. Phys.* **1999**, *111*, 9743.
- [189] M. Chiesa, M.C. Paganini, G. Spoto, E. Giamello, C. Di Valentin, A. D. Vitto, G. Pacchioni, *J. Phys. Chem. B* **2005**, *109*, 7314.
- [190] E. N. Gribov, S. Bertarione, D. Scarano, C. Lamberti, G. Spoto, and A. Zecchina, *J. Phys. Chem. B* **2004**, *108*, 16174.
- [191] Gaussian 03, Revision B.04, M. J. Frisch, G. W. Trucks, H. B. Schlegel, G. E. Scuseria, M. A. Robb, J. R. Cheeseman, J. A. Montgomery Jr., T. Vreven, K. N. Kudin, J. C. Burant, J. M. Millam, S. S. Iyengar, J. Tomasi, V. Barone, B. Mennucci, M. Cossi, G. Scalmani, N. Rega, G. A. Petersson, H. Nakatsuji, M. Hada, M. Ehara, K. Toyota, R. Fukuda, J. Hasegawa, M. Ishida, T. Nakajima, Y. Honda, O. Kitao, H. Nakai, M. Klene, X. Li, J. E. Knox, H.P. Hratchian, J. B. Cross, C. Adamo, J. Jaramillo, R. Gomperts, R. E. Stratmann, O. Yazyev, A. J. Austin, R. Cammi, C. Pomelli, J. W. Ochterski, P. Y. Ayala, K. Morokuma, G. A. Voth, P. Salvador, J. J. Dannenberg, V. G. Zakrzewski, S. Dapprich, A. D. Daniels, M. C. Strain, O. Farkas, D. K. Malick, A. D. Rabuck, K. Raghavachari, J. B. Foresman, J. V. Ortiz, Q. Cui, A. G. Baboul, S. Clifford, J. Cioslowski, B. B. Stefanov, G. Liu, A. Liashenko, P. Piskorz, I. Komaromi, R. L. Martin, D. J. Fox, T. Keith, M. A. Al-Laham, C. Y. Peng, A. Nanayakkara, M. Challacombe, P. M. W. Gill, B. Johnson, W. Chen, M. W. Wong, C. Gonzalez, and J. A. Pople, Gaussian Inc., Pittsburgh PA, USA 2003.
- [192] W. R. Wadt, P. J. Hay, *J. Chem. Phys.* **1985**, *82*, 284.
- [193] A. D. Becke, *J. Chem. Phys.* **1993**, *98*, 5648.
- [194] C. Lee, W. Yang, R. G. Parr, *Phys. Rev. B* **1988**, *37*, 785.
- [195] M. Sterrer, O. Diwald, E. Knözinger, P. V. Sushko, A. L. Shluger, *J. Phys. Chem. B* **2002**, *106*, 12478.
- [196] O. Diwald, E. Knözinger, *J. Phys. Chem. B* **2002**, *106*, 3495.
- [197] M. Ménétrey, A. Markovits, C. Minot, A. Del Vitto, G. Pacchioni, *Surf. Sci.* **2004**, *549*, 294.
- [198] J. L. Dye, *Science* **2003**, *301*, 607.
- [199] S. Matsuishi, Y. Toda, M. Miyakawa, K. Hayashi, T. Kamiya, M. Hirano, I. Tanaka, H. Hosono, *Science* **2003**, *301*, 626.
- [200] K. Yonemitsu, *Mol. Cryst. Liq. Cryst.* **2002**, *376*, 53.
- [201] K. Hayashi, S. Matsuishi, T. Kamiya, M. Hirano, H. Hosono, *Nature* **2002**, *419*, 462.
- [202] P. V. Sushko, A. L. Shluger, K. Hayashi, M. Hirano, H. Hosono, *Phys. Rev. Lett.* **2003**, *91*, 126401.
- [203] M. Chiesa, M. C. Paganini, E. Giamello, *Chem. Phys. Chem.* **2004**, *5*, 1897.
- [204] A. Stesmans, V.V. Afanas'ev, *J. Vac. Sci. Technol. B* **2002**, *1720*, 20.
- [205] G. Pacchioni, *Chem.Phys.Chem.* **2003**, *104*, 14.

Curriculum Vitae von Thomas Berger

Zur Person:

Geburtsdatum: 7.3.1978
Geburtsort: Eisenstadt
Staatsbürgerschaft: Österreich
Familienstand: ledig

Ausbildung:

September 1984 - Juni 1988 Besuch der Volksschule Draßburg-Baumgarten

September 1988 - Juni 1996 Besuch des Gymnasiums Mattersburg
Abschluß mit ausgezeichnetem Erfolg

Oktober 1996 - März 2001 Studium der Physikalischen Chemie an der
Technischen Universität Wien
Abschluß mit Auszeichnung

Juli 2000 - Februar 2001 Arbeit an der Diplomarbeit zum Thema
„Elektronische Eigenschaften reiner und Li-
dotierter MgO-Nanopartikel“ (ausgezeichnet mit
dem Förderpreis der Gesellschaft
Österreichischer Chemiker 2001) unter der
Betreuung von Prof. Dr. Erich Knözinger, Institut
für Physikalische und Theoretische Chemie, TU
Wien

Tätigkeit als Studienassistent

Juni 2001 - Mai 2002 Zivildienst beim Österreichischen Roten Kreuz

Juni 2002 - Mai 2005 Arbeit an der Dissertation zum Thema:
„Photoelectronic properties of semiconducting
and insulating nanocrystals“ unter der Betreuung
von Prof. Dr. Erich Knözinger am Institut für
Materialchemie, TU Wien

seit Juni 2002 Wissenschaftlicher Mitarbeiter am Institut für
Materialchemie, TU Wien